Lattice Energy as Emerging General Parameter Describing Ionic Organic Semiconducting Materials Properties

THÈSE N^{O} 9110 (2018)

PRÉSENTÉE LE 30 NOVEMBRE 2018

À LA FACULTÉ DES SCIENCES ET TECHNIQUES DE L'INGÉNIEUR

SMX - ENSEIGNEMENT

PROGRAMME DOCTORAL EN CHIMIE ET GÉNIE CHIMIQUE

ÉCOLE POLYTECHNIQUE FÉDÉRALE DE LAUSANNE

POUR L'OBTENTION DU GRADE DE DOCTEUR ÈS SCIENCES

PAR

Donatas GESEVIČIUS

acceptée sur proposition du jury:

Prof. U. A. Hagfeldt, président du jury
Prof. F. Nüesch, Dr J. Heier, directeurs de thèse
Prof. I. Krossing, rapporteur
Dr P.-A. Bouit, rapporteur
Prof. M. K. Nazeeruddin, rapporteur

ÉCOLE POLYTECHNIQUE
FÉDÉRALE DE LAUSANNE

Suisse
2018

“Wenn du nur machst was man dir sagt, wirst du’s nicht weit bringen.”

– Sido

“Die Zeit kommt und du musst einsehen, nur Glück, Family und die Gesundheit zählen.”

– Kc Rebell

“Erfolg ist kein Glück, sondern nur das Ergebnis aus Blut, Schweiß und Tränen das Leben zahlt alles mal zurück.”

– Kontra K

Acknowledgements

In the first instance, my thanks go to Prof. Frank Nüesch and Dr. Jakob Heier for the opportunity to perform a PhD in the Functional Polymer group at EMPA. Further, I would like to acknowledge the jury members and the jury president which are taking their valuable time for examination and reading of this thesis. Prof. Ingo Krossing for its inspiring work on weakly coordinating anions which helped me to develop and adopt own ideas. Dr. Antonia Neels, Dr. Erwin Hack and Dr. Sergii Yakunin for their helpful and fast collaborations, which is not self-evident at EMPA. Special thanks are going also to Guido Toivanen from ETH personal coaching and Jolanda Müller from the HR department for solving internal problems.

The former and current members of the Functional Polymers group have helped me during my PhD in many ways. I would like to thank therefore Anna for showing me CV measurements, Mohammed and Sandra for the introduction towards evaporation techniques and device fabrication, Surendra for all kind of scientific discussions and knowledge transfer, Beatrice for thermal measurements and Christian for the introduction to the optical microscope, Dani being always nice and doing NMR measurements without complaints, Dorina and Philip for putting thiols into my lab fridge, Dr. Matthias Nagel for providing me a clean lab space which was up to date regarding the security standards, Roland for the nice and very helpful weekly Wednesday group meetings and Philip for his laughing and some funny videos that came up during his teeth brushing activities. Special thanks go to Nicolas being my office mate and sharing the burdens which came up during the long three years and four months. Together we achieved the state of becoming a “Jean”. And EMPA in general for being “the place where innovation starts”.

I would also like to thank all my remaining colleagues from the Functional Polymers group for all the scientific and non-scientific discussions and funny activities during and after working hours. Simon, Song, Elena, Matteo, Lei, Tym, Mikel, Adrian, Yauhen and Jose… Jose Ciotas…Aleeeee suczka!

Very important for me was the support of my family, which helped me withstand very stressful and frustrating times. Thank you for that!

Zurich, 14th of September, 2018

Abstract

Cyanine dyes represent a class of ionic functional materials used by a broad heterogeneous science community containing biologists, chemists, physicists and materials scientists. Their diverse application opportunities are ranging from fluorescence markers, nonlinear optics, CD-R data storage, photography and organic electronics. Therefore the development of cyanine dyes and their applications in chemistry, engineering, medicine and pharmacology is growing continuously. A typical leitmotif of a cyanine dye contains two nitrogen heterocyclic rings joined by a conjugated chain of carbon atoms. Due to the synthetic approach, quaternary salt precursors are required resulting in ionic compounds. Such chromophores are positively charged and require a counter anion to maintain the overall charge neutrality. Several reports were presenting certain anions as efficiency enhancers in cyanine dye based organic electronic devices. Despite their long presence in science, there is a lack of knowledge behind the mechanisms causing these efficiency enhancements. Furthermore, in the field of organic electronics the processability of cyanine dyes towards electronic devices was restricted to solution based methods.

In the present thesis work the three main challenges in cyanine dye research, namely: efficient ion exchange procedures, mechanisms behind organic electronics figures of merit enhancement as well as the introduction of physical vapour deposition method have been addressed. An efficient halide-for-anion exchange method with the potential for industry scale up was introduced. This allowed modifying a cationic cyanine chromophore with organic or inorganic anions yielding six salts. The following investigations of these six anions by either varying organic moieties or negative charge delocalisation paved the way towards a generalized concept describing the semiconducting properties of this cationic cyanine chromophore. The lattice energy was established as a universal parameter describing cyanine salt semiconducting properties on a universal energy scale. Such decoupling of an ionic structure from its Lewis formula allows future predictions of semiconducting properties which can be widened to all organic ionic functional materials. Furthermore weakly coordinating anion influence on the volatility of a cyanine chromophore established physical vapour deposition as thin film fabrication method. Using co-evaporation of the cyanine dye and the fullerene C_{60} a suitable bulk heterojunction morphology was obtained. This resulted in the fabrication of the first fully vacuum deposited cyanine dye bulk heterojunction device.

Keywords

Cyanine dyes, weakly coordinating anions, lattice energy, Coulomb interactions, volatility, enthalpy of vaporisation, physical vapour deposition, fluorescence intensity, morphology, organic photovoltaics.

Résumé

Cyanin-Farbstoffe repräsentieren eine Klasse von ionischen funktionellen Materialien die von einer breiten heterogenen Wissenschaftsgemeinde bestehend aus Biologen, Chemikern, Physikern und Materialwissenschaftlern verwendet werden. Deren breit gefächerte Anwendungsmöglichkeiten reichen von Fluoreszensmarkern, nicht linearen Optiken, CD-R Datenspeicherung, Photographie und organischen Elektronik. Cyanin-Farbstoffe unterliegen einer stetigen Weiterentwicklung in den Gebieten der Chemie, Ingenieurswissenschaften, Medizin und Pharmakologie. Ein für Cyanin-Farbstoffe charakteristisches Merkmal ist die Verknüpfung von zwei Heteroatomhaltigen Heterozyklen mittels einer Polymethin-Kette. Bedingt durch den Einsatz von quaternären Salzen während der Syntheseführung entstehen ionische Verbindungen. Das Cyanin-Chromophor ist dabei positiv geladen und benötigt ein Gegenion für den Ladungsausgleich. Mehrere Wissenschaftliche Arbeiten auf dem Gebiet der organischen Elektronik präsentieren selektierte Anionen in den Cyanin-Farbstoffen als Effizienzfördernd. Trotz der Langzeitpräsens dieser Substanzklasse sind die zugrunde liegenden Mechanismen der Effizienzsteigerung unerforscht. Die Prozessierbarkeit solcher Farbstoffe in der organischen Elektronik ist bis heute auf Lösungsmittel basierte Abscheidungsmethoden limitiert.

Drei ungelöste Herausforderungen in der Cyanin-Halbleiterforschung wurden während dieser Doktorarbeit bearbeitet. Dazu gehören die Entwicklung von einem effizienten Anionenaustauschprozess, Aufstellung eines generellen Mechanismus der die Cyanin-Farbstoff Halbeitereigenschaften beschreibt und die Einführung von physikalischen Gasphasenabscheidung als Methode zur Dünschichtenformulierung. Eine effiziente Halogen-zu-Anion Austauschmethode die Industriepotential aufweist wurde eingeführt. Mit Hilfe dieser Methode war es möglich ein kationisches Cyanin-Chromophor mit organischen und anorganischen Anionen zu modifizieren. Die darauf folgenden Untersuchungen dieser Anionen bezüglich Variation des organischen Rests gegenüber der negativen Ladungsdelokalisation über mehrere Atome ermöglichten ein generelles Konzept einzuführen, welches die Halbleitereigenschaften von einem kationischen Cyanin-Chromophor beschreibt. Die Gitterenergie wurde als ein universeller Parameter etabliert der die Halbleitereigenschaften auf einer Energieskala beschreibt. Eine Loslösung von einer bestimmten Lewis Formel erlaubt es Vorhersagen zu treffen bezüglich Halbleitereigenschaften von einer breiten Klasse an ionischen Materialien. Desweiteren hat der Einsatz eines schwach koordinierenden Anions die physikalische Gasphasenabscheidungsmethode in Cyaninen zur Dünschichtformulierung ermöglicht. Unter Einsatz von Koverdampfung war es möglich eine Bulk-Heterostruktur zwischen einem Cyanin-Farbstoff und einem Fulleren zu erzeugen. Dies ermöglichte die Herstellung der ersten Vakuumprozessierten Cyanin-Farbstoff Bulk-Heterostruktur Solarzelle.

Schlüsselwörter

Cyanin-Farbstoffe, schwach koordinierende Anionen, Gitterenergie, Coulombwechselwirkungen, Flüchtigkeit, Verdampfungsenthalpie, Physikalische Gasphasenabscheidung, Fluoreszenzintensität, Morphologie, organische Photovoltaik.

Contents

Acknowledgements ..... **v**

Abstract ..... **vii**

Keywords ..... **vii**

Résumé ..... **viii**

Schlüsselwörter ..... **viii**

List of Figures ..... **xiii**

List of Tables ..... **xv**

List of Equations ..... **xv**

Chapter 1 General Introduction **17**

1.1 General Prequel to the Topic 17

1.2 Salts 17

1.2.1 The Basic Structure of Salts 17

1.2.2 Molecular Salts 17

1.2.3 Lattice Energy and Coulomb Interactions of Salts 18

1.3 General Organic Semiconductor Properties 20

1.3.1 UV-Vis and Photoluminescence Properties of Organic Semiconductors 21

1.4 Organic Photovoltaic Properties 22

1.4.1 Organic Photovoltaic (OPV) Device Architectures 22

1.4.2 Organic Photovoltaic Device Working Principles 23

1.4.3 External Quantum Efficiency (EQE) 24

1.5 References 24

Chapter 2 Increasing Photovoltaic Performance of an Organic Cationic Chromophore by Anion Exchange 29

2.1 Declaration of Contribution 29

2.2 Keywords 30

2.3 Abstract 30

2.4 Introduction 30

2.5 Results and Discussion 31

2.5.1 General Ion Exchange Pathway 31

2.5.2 Anion Influence on Thermal, Optical and Electrochemical Properties 32

2.5.3 Anion Influence on Crystal Packing, and Electronic Structure 33

2.5.4 Anion Influence on Thin Film Morphology 35

2.5.5 Anion Influence on OPV Device Performance 36

2.5.6 Conclusion 37

2.6 Experimental Section 38

2.6.1 Materials and Methods 38

2.6.2 Device Fabrication and Characterisation ... 38
2.6.3 Further Characterisation ... 38
2.7 Supporting Information ... 39
2.7.1 General Information ... 39
2.7.2 General Notation for this Work ... 39
2.7.3 Anion Exchange Procedure ... 39
2.7.4 General Loading of the Resin ... 39
2.7.5 Determination of Resin Capacity ... 39
2.7.6 Synthesis of $Cy5O_3SMe \times H_2O$ ... 40
2.7.7 Synthesis of $Cy5O_3SPh$ ... 40
2.7.8 Synthesis of $Cy5O_3SPhMe$ ... 41
2.7.9 Synthesis of $Cy5O_3SNaphth \times H_2O$ ... 42
2.7.10 Synthesis of Cy5TFSI ... 42
2.7.11 Thin Film Morphology and Thickness Evaluation ... 43
2.7.12 Screening of Suitable Solvents on Glass/MoO_3 Substrate ... 43
2.7.13 Determination of Resulting Film Thicknesses After Solution Spincoating ... 43
2.7.14 Thermal Behaviour of the Dyes ... 44
2.7.15 UV-Vis absorbance ... 46
2.7.16 Cyclic Voltammetry for Determination of HOMO/LUMO Energy Levels ... 49
2.7.17 Carrier Mobility using the CELIV Method ... 52
2.7.18 Relative Permittivity ... 53
2.7.19 Crystal Structures ... 55
2.7.20 Organic Photovoltaic Device Fabrication ... 59
2.7.21 Statistics of the Cy5TFSI Cell ... 60
2.7.22 Optimization Trials of the Cy5TFSI Cell ... 60
2.7.23 Vacuum Treatment of the Active Layer ... 60
2.7.24 Thermal Annealing Followed After Vacuum Treatment ... 60
2.7.25 Additive Effect ... 61
2.7.26 Active Layer Thickness Variation ... 62
2.7.27 Aging behavior ... 64
2.7.28 DFT Calculations of Cyanine Dyes Based on Single Crystal Data ... 65
2.7.29 Literature Supporting Information ... 66
2.8 Acknowledgements ... 66
2.9 References ... 66
Chapter 3 Superweak Coordinating Anion as Superstrong Enhancer of Cyanine Organic Semiconductor Properties . 69
3.1 Declaration of Contribution ... 69
3.2 Keywords ... 70

3.3 Abstract 70
3.4 Introduction 70
3.5 Results and Discussion 71
3.5.1 Anion Exchange and Solid State Features 71
3.5.2 Optical and Thermal Properties 72
3.5.3 Anion Influence on Thin Film Morphology 74
3.5.4 Anion Influence on OPV Device Performance 75
3.6 Conclusion 77
3.7 Experimental Section 77
3.7.1 Materials and Methods 77
3.7.2 Device Fabrication and Characterisation 77
3.7.3 Further Characterisation 78
3.8 Supporting Information 78
3.8.1 General Information 78
3.8.2 General Notation for this Work 78
3.8.3 Anion Exchange Procedure 79
3.8.4 Crystal Structure 79
3.8.5 Overview about possible ways to access parameters describing anion-cation 79
interactions in a single crystal 79
3.8.6 UV-Vis absorbance 82
3.8.7 Fluorescence 84
3.8.8 Active Light Absorbing Layer Morphology 85
3.8.9 Organic Photovoltaic Device Fabrication 86
3.8.10 Used Architecture of the Organic Photovoltaic (OPV) Device 86
3.8.11 Active Layer Thickness Adjustment 86
3.8.12 Determination of Optimum Hole Transport Layer (HTL) Thickness 87
3.8.13 Determination of Optimum Active Light Absorbing Layer Thickness 88
3.8.14 Optimized Device Descriptive Statistics 89
3.8.15 Short Circuit Current Density Calculation 90
3.8.16 Relative Permittivity 90
3.8.17 Literature Supporting Information 92
3.9 Acknowledgements 92
3.10 References 92
Chapter 4 Physical Vapor Deposition of Cyanine Salt and First Application in Organic Electronic Devices 95
4.1 Declaration of Contribution 95
4.2 Keywords 96
4.3 Abstract 96

4.4 Introduction 96
4.5 Results and Discussion 97
4.5.1 From Material Synthesis to Optical and Electrochemical Properties 97
4.5.2 Factors Enabling Physical Vapour Deposition 98
4.5.3 Substrate Dependent Thin Film Morphology 101
4.5.4 Proof of Concept in Organic Electronic Devices 103
4.6 Conclusion 104
4.7 Experimental Section 104
4.7.1 Materials and Methods 104
4.7.2 Device Fabrication and Characterisation 105
4.7.3 Further Characterisation 105
4.8 Supporting Information 105
4.8.1 General Information 106
4.8.2 General Notation for this Work 106
4.8.3 Anion Exchange Procedure 106
4.8.4 Synthesis of Cy3TFSI 106
4.8.5 Thin Film Evaporation 107
4.8.6 Qualitative trials of Cy3TFSI evaporation 107
4.8.7 UV-Vis absorbance 107
4.8.8 Cyclic Voltammetry for Estimation of HOMO/LUMO Energy Levels 109
4.8.9 Thermal Behaviour of Cy3I and Cy3TFSI 111
4.8.10 Crystal Structures 115
4.8.11 Relative Permittivity 118
4.8.12 Thin Film Morphology 120
4.8.13 Organic Photovoltaic Device Fabrication 120
4.8.14 Sort Circuit Current Density Calculation 125
4.8.15 Literature Supporting Information 126
4.9 Acknowledgements 126
4.10 References 126
Chapter 5 Conclusion 129
5.1 General Conclusion 129
5.1.1 Outlook of Future Development 130
Curriculum Vitae 133

List of Figures

Figure 2:1 Schematic representation of the ion exchange procedure. A): The anion exchange resin is loaded with the corresponding anions. Acids are acting as anion source. B): A solution of the starting material is passed through the resin equilibrated with MeCN. 31

Figure 2:2 A) Normalized UV-Vis spectra of the cyanine dye salts from Ethanol solution, B) UV-Vis spectrum of 10 nm thick films in solid state. The chromophores with sulfonate anions were spincasted from ethanol solution, while TFP was used as a solvent for the Cy5TFSI compound. 32

Figure 2:3 Anion coordination environment observed from single crystal data. The shortest anion-chromophore distances observed with Mercury are given in Å. A): $Cy5O_3SMe$, B): $Cy5O_3SPh$, C): $Cy5O_3SPhMe$, D): Cy5TFSI. The thermal ellipsoids represent 50% probability levels. All solvent and disordered molecules as well as hydrogen atoms are omitted for clarity. Additionally anionic contacts to the nitrogen atoms of surrounding chromophores are shown in the case of $Cy5O_3SMe$ and $Cy5O_3SPh$. In the case of $Cy5O_3Ph$ only the SO_3^- charge carrying group is shown for clarity. Color code: C: grey, N: violet, S: yellow, O: red, F: yellow-green. 34

Figure 2:4 Anion influence on crystal packing, the thermal ellipsoids represent 50% probability levels. A): $Cy5O_3SMe$ along a axis, B): $Cy5O_3SPh$ packing along c axis, C): $Cy5O_3SPhMe$ packing along b axis, D): Cy5TFSI packing along b axis. All solvent and disordered molecules as well as hydrogen atoms are omitted for clarity. Color code: C: grey, N: violet, S: yellow, O: red, F: yellow-green. 35

Figure 2:5 Topography of the active layer. The scanned area was fixed to 20·20 μm^2 for all compounds. 36

Figure 2:6 JV and EQE curves of the best performing OPV cells. A): Cells under light illumination, B): dark current measured right after fabrication, C): external quantum efficiency efficiency of aged devices (several weeks of storage in a glovebox). 37

Figure 3:1 A) Asymmetric unit representing the $Cy5[Al(pftb)_4]$ in ellipsoid view with 30% probability level. The hydrogen atoms and intercalated chlorobenzene solvent molecules are omitted for clarity. Color code: C: grey, N: violet, O: red, F: yellow, Al: purple. B) Molecular arrangement of $Cy5[Al(pftb)_4]$ over 2x1x2 unit cells in ellipsoid view with 30% probability level. Hydrogen atoms and intercalated chlorobenzene solvent molecules are omitted. Color code chromophore: C. grey, N, violet. The anions are colored red for clarity reasons. C) Bond length alternation comparison between different salts of the Cy5 chromophore. 71

Figure 3:2 A) Normalized UV-Vis absorbance spectra of $Cy5[Al(pftb)_4]$ from ethanol solution and 15 nm thick spin-casted film. B) UV-Vis solid state absorbance bandwidth dependence on lattice energy and comparison with the bandwidth in solution (R^2: 0.92 and Pearson's r: 0.96). The lattice energy represents the following materials: $Cy5O_3SMe$ (180.4 kJ mol^{-1}), $Cy5O_3SPh$ (175.4 kJ mol^{-1}), $Cy5O_3SPhMe$ (174.4 kJ mol^{-1}), Cy5TFSI (170.2 kJ mol^{-1}), $Cy5[Al(pftb)_4]$ (140.9 kJ mol^{-1}). 72

Figure 3:3 A) Fluorescence intensity obtained at 709 nm emission maxima from 10 nm thick spin-casted films plotted against the lattice energy of the corresponding Cy5 salts with R^2 of 0.99 and Pearson's r of -0.99. The lattice energy represents the following materials: $Cy5O_3SMe$ (180.4 kJ mol^{-1}), $Cy5O_3SPh$ (175.4 kJ mol^{-1}), $Cy5O_3SPhMe$ (174.4 kJ mol^{-1}), Cy5TFSI (170.2 kJ mol^{-1}), $Cy5[Al(pftb)_4]$ (140.9 kJ mol^{-1}). B) Fluorescence lifetime of $Cy5[Al(pftb)_4]$. 73

Figure 3:4 In situ thermogravimetric analysis and differential scanning calorimetry (endo up) of $Cy5[Al(pftb)_4]$. 74

Figure 3:5 AFM images of spin-casted $Cy5[Al(pftb)_4]$ films on V_2O_5 and MoO_3 substrates. On MoO_3 a dendritic crystal is observed. 74

Figure 3:6 Current density vs.Voltage and external quantum efficiency plots of the best performing $Cy5[Al(pftb)_4]$ cell. 75

Figure 3:7 OPV device parameters plotted against lattice energy of various Cy5 salts. The lattice energy represents the following materials: $Cy5O_3SMe$ (180.4 kJ mol^{-1}), $Cy5O_3SPh$ (175.4 kJ mol^{-1}), $Cy5O_3SPhMe$

(174.4 kJ mol^{-1}), Cy5TFSI (170.2 kJ mol^{-1}), Cy5[Al(pftb)$_4$] (140.9 kJ mol^{-1}). Each data point for EQE, FF, J_{sc}, V_{oc} and Eff (η) contain averaged values with their standard deviation. The data points for EQE were taken from best performing cells at maximum conversion wavelength. The linear correlation curves in red have an R^2/Pearson's r of 0.98/-0.98, 0.97/-0.98 and 0.99/-0.99 for EQE, V_{OC} and Eff (η) respectively. 76

Figure 4:1 On the left: cartoon depicting the molecular structure of the Cy3TFSI salt with the corresponding energy level alignment respective possible device fabrication. On the right: qualitative UV-Vis spectra of evaporated thin films on different substrates. 97

Figure 4:2 Dynamic TGA (10 °C min^{-1}) with corresponding DSC signal of starting material (Cy3I) and Cy3TFSI. 98

Figure 4:3 The upper row represents extracted weight losses as a function of time occurring during each isothermal step. The lower row represents the extracted slopes of the isothermal weight loss curves as function of temperature. 99

Figure 4:4 Molecular structure and anion coordination environment observed in the single crystal structures of Cy3I and Cy3TFSI. The shortest anion-chromophore distances are given in Å. The thermal ellipsoids represent 50% probability levels. The disorder in Cy3TFSI as well as the hydrogen atoms are omitted for clarity. Color code: C: grey, N: violet, S: yellow, O: red, F: yellow-green, I: purple. 100

Figure 4:5 Molecular arrangement over 2x2x2 unit cells with views along the a axis (left) and b axis (right). For clarity the Cy3TFSI packing is depicted in the wire frame model, while Cy3I contains the chromophore in wire frame and the iodide as thermal ellipsoid with 50% probability level. The disorder in Cy3TFSI as well as the hydrogen atoms are omitted for clarity. Color code: Cy3TFSI symmetry equivalent chromophores: red, anion: blue. Cy3I symmetry equivalent chromophores: blue and green, iodide: red or purple. 101

Figure 4:6 Topography of vacuum deposited Cy3TFSI films on different substrates. 102

Figure 4:7 Topography of coevaporated Cy3TFSI and C_{60} on TiO_2 and MoO_3 substrates. 102

Figure 4:8 JV and EQE curves of the best performing OPV cell. The EQE represents a sharp C_{60} peak at shorter wavelengths followed by an overlap of the second C_{60} absorption peak with Cy3TFSI. 103

List of Tables

Table 2:1 Crystallographic parameters of the measured compounds. The R_1/wR_2 values represent the quality of the solved crystal model. 33

Table 2:2 Averaged OPV performance data for all investigated cells with the corresponding standard deviation of all measured cells. 37

List of Equations

Equation 1:1 – Lattice energy attraction term. 18

Equation 1:2 – Lattice energy repulsion term. 18

Equation 1:3 – Equalibrium separation term. 18

Equation 1:4 – Born-Landé equation. 18

Equation 1:5 – Kapustinskii equation. 19

Equation 1:6 – Mallouk and Barlett equation. 19

Equation 1:7 – Ionic strength term. 19

Equation 1:8 – Normalized molecular volume. 19

Equation 1:9 – Molecular volume for closely packed structures. 19

Equation 1:10 – Lattice energy derived by Glasser and Jenkins. 20

Equation 1:11 – Energy difference between HOMO and LUMO. 20

Equation 1:12 – General Lambert-Beer Law. 21

Equation 1:13 – Absorbance. 21

Equation 1:14 – Lambert-Beer law normalized to a molar concentration. 21

Equation 1:15 – Lifetime of the emission process. 22

Equation 1:16 – Quantum Yield. 22

Equation 1:17 – Ratio between measured fluorescence lifetime and natural raiative lifetime. 22

Equation 1:18 – Calculation of opencircuit voltage. 23

Equation 1:19 – Calculation of the fill factor. 23

Equation 1:20 – Calculation of the power conversion efficiency. 24

Equation 1:21 – Calculation of the external quantum efficiency. 24

Chapter 1 General Introduction

1.1 General Prequel to the Topic

Salts are common naturally occurring compounds which have accompanied our lives over centuries. The first thought hearing this name is about rock salt known as sodium chloride, often also named white gold.[1] This trivial name evolved due to the fact that empires built their wealth on salt trade. Besides this well-known application as spice, nature and human beings employed salts of various compositions in salt concentration gradient driven osmosis,[2] generation of electrical and chemical gradients by proton pumps,[3] intercalation of metal ions to proteins,[4] and energy storage[5] just to name a few. Salts can be found almost everywhere. Such frequent usage of salts in complex organic systems as well as material science and their diverse behavior indicates the importance of this material class.

The following general introduction sections will guide the reader through basic description of an ionic structure beginning with inorganic salts and continuing towards complex molecular organic-inorganic hybrid salts. At the end the complex behavior of organic salts as light absorbers and their semiconducting properties will be introduced guiding the reader towards the core topic of this work, namely the investigation of organic salt cyanine dyes as optoelectronically active organic semiconductors. The reader will be able to understand and link salt structure describing terms namely: lattice energy and Coulomb interactions with physicochemical and semiconducting properties in particular: morphology, volatility, excited state lifetime, charge transfer states and organic photovoltaic descriptive parameters. Introduction of the lattice energy concept enables a general investigation of Coulomb interactions within a salt decoupled from the particular molecular structure of the cation or anion. Decoupling a salt like structure from its Lewis formula as aimed by this work sets a possible guideline for future theoretical predictions which will be useful for the re-emerging interest on cyanine dye salts.

1.2 Salts

1.2.1 The Basic Structure of Salts

A common understanding of salts arises when considering a chemical reaction of two elements with an incomplete electron octet. The driving force to reach a full outer shell and thus the next noble gas state leads to an electron migration from elements on the left side of the periodic system towards the elements on the right side of the periodic system.[6] Generally spoken the furthest away both salt forming elements are in the periodic system the higher their affinity to form salts. In all cases salts contain electron poor cations and electron rich anions. The cohesion of an ionic solid is due to the long range electrostatic interactions across all directions in space.[7] Therefore one ion attracts more than just one counterpart leading to an ionic crystal lattice. As a consequence of these large ionic lattices, salts have high melting points and small vapor pressure. They possess a high degree of hardness, but in contrary to metals they are brittle. A result of short range interaction of similar charged ions due to mechanical stress.[8] Solvents with high dielectric constant are suitable in dissolving such salts. These solutions usually exhibit electrical conductivity.[9]

1.2.2 Molecular Salts

In contrary to classical inorganic salts containing two elements of the periodic table, molecular salts contain polyatomic ions. Most prominent examples are: sulfate, sulfonate, perchlorate, ammonium and phosphonium just to name a few. Such inorganic ions can be derived from their free acids or bases. In contrary to salts containing monoatomic ions their physical properties are not strictly limited to high melting points.[10] Several compounds with melting temperatures around 100 °C were developed and classified as inorganic ionic liquids.[11] Among these, transition metal based polyoxometalate anions with sodium cations are even liquid at room temperature.[12] Besides their inorganic counterparts many complex organic[13], organic-inorganic[14], organometallic[15] and polymer hybrid[16] salts exist. Their synthetic pathway and physical properties entirely differ from the inorganic salts. The most prominent class of such salts is called ionic liquids and was firstly developed in 1914.[17] In the meantime ionic liquids evolved to a broad research field which is covered by an almost uncountable amount of papers and reviews.[18–20] Usually an organic molecular cation often containing *N*-heterocycles with bulky side chains is paired with either an organic or inorganic molecular anion.[21,22] The negative charge of these anions is often distributed over several atoms.[23] Such weakly coordinating feature paired with steric hindrance originating from the cation leads to melting points below 100 °C and even below room temperature in certain cases.[24] The volatility of such salts increases drastically due to an increased vapour pressure.[25] New physical properties regarding among others viscosity[26] paired with solubility[27] and electrochemistry[28,29] of organic compounds emerge. However interesting properties of organic or organic-inorganic hybrid salts are not limited to ionic liquids only. A material class called: “Group of Uniform Materials Based on Organic

Salts" (GUMBOS) is widely used in life and material sciences.[30–33] Cyanine dye salts are claiming a significant role within this material class. Their further structural features and physicochemical properties are extensively described in the introduction and discussion parts of the three research chapters.

1.2.3 Lattice Energy and Coulomb Interactions of Salts

Despite molecular structure differences of presented salts and diverse physical properties two parameters can be applied universally to each ionic structure. The lattice energy and Coulomb interactions describe the processes undergoing within an ionic structure very well regardless their chemical composition. These parameters represent the fundament of the entire thesis and will help the reader in terms of understanding and linking the three research chapters of this thesis.
The first approach defining lattice energy of an ionic solid was given by Born and Landé.[34] It contains two terms of which the first one describes an electrostatic attraction. The idea behind it is that counter charges generally attract each other.

$$\Delta U_{el} = -\frac{N_A M |Z^+||Z^-| e^2}{r}$$

Equation 1:1 – Lattice energy attraction term.

ΔU_{el}: Electrostatic attraction term, N_A: Avogadro's number, M: Madelung constant, $Z^{+/-}$: cation/anion charge number, e: elemental charge, ε_0: vacuum permittivity, r: distance between two ions of opposite charge.

In this case the Madelung[35] constant multiplied by $-e^2/r$ yields the potential energy for one single ion of the lattice.[36] The Avogadro number accounts for the energy of a mole of ions. The second term deals with the repulsive forces representing the potential energy. Here repulsive forces are considered, occurring when two equal charges are placed in close distance to each other. This term depends on the Born exponent representing the compressibility of the ionic solid.[37]

$$\Delta U_{rep} = \frac{N_A B}{r^n}$$

Equation 1:2 – Lattice energy repulsion term.

ΔU_{rep}: Repulsive term, B: repulsion coefficient, n: Born exponent representing the power of the distance.

Combined, the two equations give the lattice energy. Hereby the compressibility term was fused into an equilibrium separation term (r_0).

$$r_0 = \left(\frac{nB}{|Z^+||Z^-| e^2 M}\right)^{\frac{1}{n-1}}$$

Equation 1:3 – Equalibrium separation term.

It is worth noting that r and n can be determined experimentally therefore the repulsion coefficient can be calculated. Defining the lattice energy ΔU as a positive quantity, one obtains:

$$\Delta U = \frac{N_A M |Z^+||Z^-| e^2}{r_0} \times \left(1 - \frac{1}{n}\right)$$

Equation 1:4 – Born-Landé equation. r_0: equilibrium separation between two ions of opposite charge.

By considering the variables of this equation it becomes clear that many factors have to be either assumed or determined experimentally. Additionally an ion in the crystal lattice is affected also from many other surrounding ions. Therefore a sum of attractive and repulsive forces has to be found which is expressed by the Madelung constant. Madelung constants are highly dependent on the coordination of the ions in the crystal structure and which can be used to approximate the Madelung constant.[38] Another limitation is that these equations are valid only for spherical ions and binary salt compositions. This limitation was overcome by Kapustinskii resulting in an equation capable of describing a broader range of ionic compounds.[39]

$$\Delta U = \left(\frac{N_A v}{2}\right)\left(\frac{\alpha |Z^+||Z^-| e^2}{r}\right) \times \left(1 - \frac{1}{n}\right)$$

Equation 1:5 – Kapustinskii equation.

v: Number of ions in the molecule, α: structural coefficient containing M/(v/2).

The term describing the molar amount of ions was expanded with the number of ions per stoichiometric unit (v) considering cases deviating from a binary salt structure. Exemplifying NaCl would yield a v value of 2 while Al_2O_3 yields 5. The factor α deals with the Madelung constant and the structure of the lattice.[40] The reason allowing this modification lays in the proportionality of α to the inter-ion distance when varying the lattice. This means that each ionic structure can be transferred to NaCl type without changing the lattice energy. Therefore a constant value can be used, which is determined for the NaCl type lattice without calculating individual Madelung constants for each lattices.[39] However already at that time it was clear that the ion radii of complex anions needed some assumptions regarding their symmetry. Also the approach in calculating the Madelung constant for NaCl type itself was proven inaccurate.[41]

Over time the spherical radii where replaced by thermochemical ionic radii.[42–44] These modifications included coordination number, consideration of covalency and structure type. Decades after the development of Born-Landé and Kapustinskii equations Mallouk and Barlett introduced a description of ionic radii based on molecular volume.[45] Hereby the ion radii refers to the inverse of the cubic root of the molecular volume (V_m). This molecular volume is obtained by dividing the unit cell volume from X-ray analysis with the number of molecules per unit cell Z. Moreover with this approach the lattice enthalpy correlates linearly with the inverse cube root expression of the ionic radii for binary salts. Further improvements were made expanding this relationship towards a broader range of salts by introducing stoichiometric coefficients.[46]

$$\Delta U = |Z^+||Z^-| v \left(\frac{a}{V_m{}^{\frac{1}{3}}} + \beta\right)$$

Equation 1:6 – Mallouk and Barlett equation.

This equation is avoiding the use of the Madelung constant as well as any structural factors. However besides the well-known variables, new constants a and β are introduced. These represent fitting results of the lattice energy assembled from various literature sources against molecular volume calculated for each salt. Hereby the slope of the regression line is expressed by a and β represents the intercept. Their values for 1:1 salts are 117.3 kJ mol^{-1} nm and 51.9 kJ mol^{-1}. Slight variation in the goodness of the fit between 0.95-0.84 was observed for 1:1, 2:1 and 1:2 salts, while naturally the slope in such fits is always better defined than the intercept. The approach of Mallouk and Barlett obtaining lattice energies will be followed in this work.

In fact since the first equations describing lattice energy of a salts appeared in 1918 the community spent decades putting efforts to replace the not trivial factors of the original equation including the spherical ion radii, Madelung constant, structural factors and empirically found constants. Glasser and Jenkins in the millennium finally presented a universal equation free from empirical fitted parameters which needs only input from X-Ray single crystal data.[47] In a first instance the description of ionic charges and their constitutional formula as introduced by Kapustinskii was replaced by an ionic strength term.[48]

$$|Z^+||Z^-| v = \frac{1}{2}\sum n_i {z_i}^2 = 2I$$

Equation 1:7 – Ionic strength term.

n_i: number of i ions with integer charge, z_i: charge of the i ions, I: ionic strength.

The relation of the ion radii was generalized and expressed in form of a normalized molecular volume applicable to all salt structures.

$$r = \left(\frac{V_m}{2I}\right)^{\frac{1}{3}} = V_{norm}{}^{\frac{1}{3}}$$

Equation 1:8 – Normalized molecular volume.

For large lattice energies, thus closely packed structures the radius has to be corrected with a limiting factor (L) value of 1.7 though.

$$r = \left(\frac{V_m}{2I}\right)^{\frac{1}{3}} L = V_{norm}{}^{\frac{1}{3}} L$$

Equation 1:9 – Molecular volume for closely packed structures.

Further, the repulsion term of the original equation (1-1/n) was formally replaced by R. By analyzing compressibility data from literature against the corresponding lattice energy a constant value for R of 0.84 can be assumed. Additionally an electrostatic constant (A) of 129.39 kJ mol^{-1} nm is introduced. This constant refers to the NaCl lattice and stays unaffected due to the above presented normalization of the molecular volume. The trick is that by placing all these parameters in the original Kapustinkii equation they cancel each other yielding a generalized equation.

$$\Delta U = AI\left(\frac{2I}{V_m}\right)^{\frac{1}{3}} = \frac{AI}{{V_{norm}}^{\frac{1}{3}}}$$

Equation 1:10 – Lattice energy derived by Glasser and Jenkins.

This type of generalized equation allows users estimating the lattice energy of a salt by using values that are obtained entirely only from the X-Ray single crystal structure data. However the absolute lattice energy estimation for complex molecular organic ions is still an ongoing task involving an increased amount of computational approaches.[49–52]

1.3 General Organic Semiconductor Properties

All organic semiconducting materials despite their structural origins, whether they can be polymers, oligomers or small molecules either neutral or ionic nature, are dependent on conjugated π-electrons enabling semiconducting properties.[53] Generally spoken alternating single and double bonds of a carbon atom containing chain or cyclic structure are needed. Carbon atoms enable high variety of covalent bonds depending on their hybridization. Certain hybridization produces different geometries within the formed molecule. For the formation of a double bond trigonal planar sp^2 hybridization is required. In this case due to the small energy gap between s and p orbitals one electron of the 2s^2 orbital is promoted into the 2p$_z$ orbital. The so formed four unpaired electrons form three sp^2 orbitals and one unchanged 2p$_z$. Energetic arrangement favours 120° geometry of the three orbitals relatively to each other with the p$_z$ being perpendicular to these. If two hybridized C atoms meet the σ bond is formed from two sp^2 orbitals facing each other while the π bond is generated from the parallel overlap of two sp^2 orbitals. Remaining orbitals are used for CH bond formation.[54] Due to geometric reasons the π bonds are weak and electrons in these orbitals delocalize over the molecule backbone allowing electrons jump from one carbon to another. This induces the directional conductivity in such molecules.[55] In polymethine chains the π orbitals form lines above and below the C atoms, while in cyclic systems a planar ring forms on top and bottom of the cyclic carbon atoms.

Organic semiconductors are complex covalent bound molecules containing up to 100 atoms and often heteroatoms with lone pairs like nitrogen, sulfur or oxygen.[56] Therefore the electron distribution within such molecules cannot be explained only by a simple hybridization approach. Sticking with the common main group atom σ and π orbitals there can be constructive and destructive orbital interactions. The constructive interactions are responsible for the formation of σ and π bonding orbitals while σ* as well as π* antibonding orbitals are formed from the destructive interferences. The electrons in organic semiconductors usually move between π and π* orbitals when an appropriate external energy amount is applied. In the electronic ground state of an organic semiconductor the π orbital is referred as the highest occupied molecular orbital (HOMO) containing two electrons of different spin, while the π* is empty and represents therefore the lowest unoccupied molecular orbital (LUMO). From an energetic point of view LUMO is higher than the HOMO therefore the energy difference between these two states is referred as HOMO-LUMO gap.[57] From this energy gap one can estimate absorbance properties of an organic molecule since this gap narrows down from ultraviolet (UV) to near infrared (NIR) region. This phenomena is caused by the quantum mechanical relation of the conjugated chain length and the HOMO-LUMO gap. One can see a conjugated π system as a particle in the box. The energy difference (ΔE) between HOMO and LUMO can be expressed by the following equation.[58]

$$\Delta E = \frac{h^2(n+1)}{8mL^2}$$

Equation 1:11 – Energy difference between HOMO and LUMO.

ΔE: Energy difference between HOMO and LUMO, h: Planck's constant, L: length of the polymethine chain, m: mass of an electron, n: number of π electrons.

Since the chain length is accounting by a square it becomes clear that with an increasing conjugated chain length the energy difference decreases. This model is valid only under the approximation that the potential energy of the electrons is equally distributed

over the conjugated chain length. In a real molecule however the potential energy fluctuates due to attraction of electrons by the nuclei or repulsion due to close distance of two equal particles. Practically spoken the bigger the bond length alternation of a system the larger is the deviation of this equation from the real energy gap.

The transfer of an electron from HOMO to the LUMO is called excitation. Therefore an exciton, which is formally a quasi-particle consisting of an electron and a hole held together by a Coulomb field, represents an organic molecule in its excited state. One can distinguish three different exciton types differing in their electron hole distance also described as radius of the quasi-particle. Bound electron-hole pairs in organic materials are either localised on one molecule or spread over molecules within the unit cell. These represent the Frenkel-exciton type with low exciton diffusion lengths. Charge transfer excitons are widespread over few lattice distances and have a mid-range exciton diffusion length. The last type is represented by Wannier-Mott excitons which are widespread over a large number of unit cells.[59] In organic semiconductors, this type occurs only at low temperatures. The most frequent Frenkel-excitons found in organic semiconductors results from a low dielectric constant of the latter.[60] Therefore excitons of this type are located on the same molecule. Charge transfer excitons are distributing their carriers on two different molecules typically represented at the hetero interface between an electron donor and acceptor. While a Wannier-Mott type exciton possesses a very low binding energy and creates free charge carriers at room temperature as it is observed for inorganic materials. These descriptions will be important in the first two research chapters since tuning Coulombic interactions and lowering the charge transfer binding energy will be addressed.

If we consider the spin of the electrons within the orbitals, four possible combinations can occur: ½ ½, ½ -½,-½ ½ and -½ -½. From this applying the 2s+1 rule for the total spin angular momentum two states can be found. A zero value for s yields a singlet and 1 represents the triplet state.[61] Spin conservation rules are important to understand UV-vis and fluorescence properties of organic semiconductors.

1.3.1 UV-Vis and Photoluminescence Properties of Organic Semiconductors

The absorption of light by an organic semiconductor is represented by the Lambert-Beers law.

$$I = I_0 e^{-\alpha z}$$

Equation 1:12 – General Lambert-Beer Law.

α: absorption coefficient, z: light penetration depth of the investigated material, I_0: intensity of the incident light, I: residual intensity of light after interaction with the material.

This equation represents the intensity of the light absorbed by an organic semiconductor. Therefore a term called absorbance can be formulated.

$$A = \log_{10} \frac{I_0}{I}$$

Equation 1:13 – Absorbance.

This correlation was further normalized to a molar concentration of the investigated material.[62]

$$\log_{10} \frac{I_0}{I} = A = \varepsilon \times l \times c$$

Equation 1:14 – Lambert-Beer law normalized to a molar concentration.

ε: molar extinction coefficient, l: light path length, c: molar concentration of the material.

From this correlation the molar extinction coefficient is an important value describing organic semiconductors capability to absorb light and can be used in first instance to estimate the suitability of a compound being employed as light harvester.
However the excited state of an organic semiconductor is not stable and undergoes several fast post excitation processes. There are singlet states: S_0 represents the ground state, S_1 is the first singlet excited state and S_n shall refer to further singlet excited states as well as triplet states: T_1 is the first triplet excited state, T_n describes further triplet excited states. The triplet and singlet states can both decay radiative. Additionally, non-radiative processes exist such as intersystem crossing, internal conversion or bimolecular reactions such as energy or electron transfer.[63] All these phenomena can occur immediately after excitation and stay in competition to each other. The radiative S_1-S_0 transition is called fluorescence a typical lifetime of a few ns. Much slower is the spin forbidden T_1-

S_0 transition called phosphorescence corresponding to a slow radiative decay in a range of microseconds up to milliseconds. Additionally intersystem crossing with non-radiative losses is required for this phenomenon making it a rare case for organic molecules.[64] In both singlet or triplet states the excited state relaxes non-radiatively to the lowest vibronic state (Kasha's rule). Therefore radiative emission occurs from the lowest excited state. The difference between absorbance- and emission-maxima is called the Stokes shift.[65] It occurs due to internal and external relaxation after the optical transition. Additionally thermal motion or different geometrical arrangement within the conjugated carbon chain or bulk material in the solid state plays a role generating various localized energy states.
The amount of photons absorbed will mostly not correspond to the amount of photons emitted. The quantification of this loss is the photoluminescence quantum yield (PLQY). A ratio obtained from the number of photons emitted divided by the number of photons absorbed. Before describing the yield one needs to specify the lifetime of the emission process.[66]

$$\tau_{PL} = \frac{1}{k_{rad} + k_{non-rad}}$$

Equation 1:15 – Lifetime of the emission process.
τ_{PL}: measured fluorescence lifetime, k_{rad}: radiative rate, $k_{non-rad}$: non-radiative rate.

By building the ratio between radiative rate and the sum of radiative and non-radiative rates the first formulation of the quantum yield is obtained:

$$\varphi = \frac{k_{rad}}{k_{rad} + k_{non-rad}}$$

Equation 1:16 – Quantum Yield.

One can also express the quantum yield as the ratio between the measured fluorescence lifetime and the natural radiative lifetime.[67]

$$\varphi = \frac{\tau_{PL}}{\tau_{rad}}$$

Equation 1:17 – Ratio between measured fluorescence lifetime and natural raiative lifetime.

1.4 Organic Photovoltaic Properties

1.4.1 Organic Photovoltaic (OPV) Device Architectures

First organic photovoltaic devices where introduced in the 60s.[68,69] A simple sandwiching of an organic layer between two electrodes yielded the first OPV device. Important is to generate an electric filed through the film (so called built-in field) by employing different work functions for the electrodes. In this case the anode has a higher work function for holes to be injected, while the cathode possesses a lower work function for electron injection.[70] Critical in such devices is the exciton diffusion and eventually exciton dissociation. The organic layer has to be thin enough to allow sufficient exciton diffusion. In a particular device architecture dissociation takes place at a depletion region near the cathode (Schottky junction) which possesses high enough external electric field to overcome the Coulombic interactions of the excitons.

Over time one has discovered that a more efficient way of splitting excitons in devices can be implemented. Introducing an additional organic electron acceptor layer provided the necessary driving force for electron transfer to the electron acceptor and hence to the cathode.[71] Such a device stack is called bilayer geometry.[72] The electron donor layer which is represented by the organic material still has to be as thick as the exciton diffusion length. But the exciton dissociation into holes and electrons takes place at the donor/acceptor interface. An external electric field for splitting when compared to single layer devices becomes redundant. In contrary the dominant driving force for exciton splitting is caused by the potential drop due to energy level difference between donor and acceptor which is enough to overcome the Coulombic interaction. This process is called charge transfer (CT) and is generally ultrafast, i.e. in the 10-100 fs range.[73] Therefore it is possible to accumulate the electrons in the electron acceptor while the holes remain in the electron donor allowing efficient physical charge carrier separation. The device architecture was improved over many years by adding additional interlayers between the anode and the donor.[74] Such layers are called hole transport (HT) interlayers and improve the hole collection towards the anode significantly. Since the cathode is usually thermally evaporated, the metal particles tend to penetrate the soft organic layers and produce shunts with the counter-electrode. Therefore thin diffusion blocking layers of only a few nm are introduced.[74] Such additional potential gradients on both electrodes improve the figures of merit of the device enormously. This device architecture will be used thorough two chapters of the thesis, allowing simple fabrication within one working day and investigations of Coulomb interactions of the organic salts used.

Over decades of research it became clear that the highest limitation regarding OPV device efficiency was the limiting exciton diffusion length of the organic donor molecules. Typical exciton diffusion lengths of organic materials lay in the range of 10 nm while the maximum light absorbance is reached for electron donor layer thicknesses around 100 nm.[75] Therefore to surpass this exciton diffusion versus light absorbing yield problem a well-defined phase separated domain structure between electron donor and acceptor in a range of 10 nm is needed. Typically blending of an electron donor with an electron acceptor in so called bulk heterojunction (BHJ) gives phase separated domains.[76] These channels have to be homogenously distributed over all three dimensions within the blend. Most common routes to achieve blending are either vacuum co-deposition or solution based spin-casting.[77] On a lab scale spin-casting established as the main method for thin bulk heterojunction layer formation. However such device architecture needs further post fabrication treatments in order to function properly. Several processing conditions and post fabrication treatments were developed to achieve the required morphology. The proper choice of solvent and additives as co-solvent are the main prominent variables for tuning the blend fabrication process.[78] Thermal and solvent annealing are well established post treatment techniques.[79] Up to date this device geometry yields the highest (OPV) efficiency values with a power conversion efficiency of >10% under lab conditions.[80]

Besides the above described device architectures several variations and alternatives exist, which include among other hybrid[81–84], inverted[85] and tandem[86] device architectures. However these are not in the focus of this work and shall be mentioned only for further independent enthusiastic reading.

1.4.2 Organic Photovoltaic Device Working Principles

By now the reader understands the general structure of salts and can deal with terms like lattice energy and Coulomb forces. Basic theory of organic semiconductors gives an overview about processes turning an organic material to an organic semiconductor. This final chapter will introduce the reader towards processes ongoing in an OPV device.

When light illuminates the OPV cell previously described phenomena take place and current is generated. In general four parameters can be defined namely: open circuit voltage (V_{OC}), short circuit current density (J_{SC}) or short circuit current (I_{SC}), fill factor (FF) and power conversion efficiency (PCE) also named efficiency (η).[87] An organic solar cell can be seen as a photo diode in first instance. Depending on the applied bias one can distinguish between two operational modes. If the voltage and the current are both negative the device operates in the third quadrant of the current-voltage diagram. It behaves like a photodetector. When the voltage is shifted towards positive values and the current remains negative the device operates in the fourth quadrant. In this quadrant the photovoltaic effect is observed and a real power can be extracted. When the voltage is zero meaning that there is no bias on the electrodes a short circuit current can be obtained, the maximum possible current that the device can provide. In a first instance the J_{SC} refers directly to the number of absorbed photons per area, exciton splitting and their extraction.[88] Without an external resistor at the point where the current is zero one can obtain the maximum possible voltage which is represented by the V_{OC}. The V_{OC} of a donor-acceptor device geometry is dependent on the energy difference between HOMO of the donor and the LUMO of the acceptor.[89,90] Further the V_{OC} is dependent on the increase of entropy as expressed by the k_BT term.

$$V_{OC} = E_{HOMO\,(d)} - E_{LUMO\,(a)} - k_B \times T \times \ln\left(\frac{N_{(d)} \times N_{(a)}}{n_i \times p_i}\right)$$

Equation 1:18 – Calculation of opencircuit voltage.

$E_{HOMO\,(d)}$: HOMO energy level of the donor, $E_{LUMO\,(a)}$: LUMO energy level of the acceptor, k_B: Bolzman constant, T: temperature, $N_{(d/a)}$: density of states in the donor and acceptor, $n_{(i)}$,$p_{(i)}$: charge carrier density in the donor and acceptor.

Meaning that the temperature of a device will have a significant influence in lowering the V_{OC}.[91] Further the V_{OC} is dependent on the energetic disorder expressed by $N_{(a/d)}$ of the material, which is implemented in the logarithmic term. As well as the light intensity represented by the charge carrier density. The maximum obtainable power is the region where the product of the current and voltage gives the highest value. When considering the way of describing the max power point it becomes clear that the more rectangular the current-voltage curve is the higher is also the product between these which leads to a higher Power. The measure of the rectangularity is given by the FF which describes how far a curve is away from being rectangular.[92] Expressed as an equation it is the ratio between max. obtainable power point and max. theoretical power point.

$$FF = \frac{P_{(\mathrm{max.})}}{P_{(max.theo.)}} = \frac{V_{P_{(max.)}} \times I_{P_{(max.)}}}{V_{OC} \times I_{SC}}$$

Equation 1:19 – Calculation of the fill factor.

$P_{(max.)}$: maximum obtainable power, $P_{(max.\ theo.)}$: maximum obtainable theoretical power, $V_{P_{(max.)}}$: voltage at the maximum obtainable power point, $I_{P_{(max.)}}$: current at the maximum obtainable power point.

The consideration of all the three described parameters yields the overall device efficiency.[93]

$$PCE\ or\ \eta = \frac{P_{(max.)}}{P_{(in)}} = \frac{V_{P_{(max.)}} \times I_{P_{(max.)}}}{P_{(in)}} = \frac{V_{OC} \times I_{SC} \times FF}{P_{(in)}}$$

Equation 1:20 – Calculation of the power conversion efficiency.

$P_{(in)}$: incident power of light.

The incident power of light is usually normalized towards 1000 W m^{-2} under standard conditions.

1.4.3 External Quantum Efficiency (EQE)

The external quantum efficiency (EQE) also known as incident photon-to-charge conversion efficiency (IPCE) is the ratio between the number of extracted electrons and the flux of incident photons.[94]

$$EQE = \frac{number\ of\ extracted\ electrons\ per\ second}{number\ of\ incident\ photons\ per\ second} = \frac{h \times c \times I}{e \times \lambda \times P}$$

Equation 1:21 – Calculation of the external quantum efficiency.

h: Planck constant, c: speed of light, e: elementary charge, λ: wavelength, I: current of the solar cell, P: power of the incident light.

The number of incident photons is determined with help of a reference cell. With known response of the reference cell at each wavelength the corresponding power is determined. With this technique it is possible to extract the amount of current for a specific wavelength. The partial wavelength dependent currents are summed up for the whole spectrum giving additional information about J_{sc} and I_{sc} respectively.[95] It is a good countercheck if the current generation follows the UV-vis properties of the organic donor and gives insights into the quality of the device. Conclusions can be made if either the donor or the acceptor are the major contributors for the photocurrent of a device and additionally degradation phenomena if applicable can be identified.

By this time the reader is able to understand what the thesis is about and can follow both the general summary as well as the research chapters dealing with the description of ionic structures expressed in terms of a universal energy scale and the connection of these with measurable organic semiconductor describing parameters.

1.5 References

[1] R. M. Geertman, In *Encyclopedia of Separation Science*; Elsevier, 2000; pp. 4127–4134.

[2] C. C. Logisz, J. S. Hovis, *Biochim. Biophys. Acta - Biomembr.* **2005**, *1717*, 104.

[3] B. P. Pedersen, M. J. Buch-Pedersen, J. Preben Morth, M. G. Palmgren, P. Nissen, *Nature* **2007**, *450*, 1111.

[4] M. M. Yamashita, L. Wesson, G. Eisenman, D. Eisenberg, *Proc. Natl. Acad. Sci.* **1990**, *87*, 5648.

[5] R. Younesi, G. M. Veith, P. Johansson, K. Edström, T. Vegge, *Energy Environ. Sci.* **2015**, *8*, 1905.

[6] A. F. Holleman, E. Wiberg, N. Wiberg, In *Lehrbuch der Anorganischen Chemie*; De Gruyter: Berlin, 2007; pp. 112–185.

[7] E. Riedel, *Allgemeine und Anorganische Chemie*; De Gruyter: Berlin, 2008; Vol. 8.

[8] H. Ode, In *M 8: Diapirism and Diapirs*; AAPG Special Volumes, 1911; Vol. 153, pp. 53–78.

[9] A. A. Noyes, *Science* **1904**, *20*, 577.

[10] G. J. Janz, C. Solomons, H. J. Gardner, *Chem. Rev.* **1958**, *58*, 461.

[11] K. Kubota, T. Nohira, R. Hagiwara, *Electrochim. Acta* **2012**, *66*, 320.

[12] L. Dai, S. Yu, Y. Shan, M. He, *Eur. J. Inorg. Chem.* **2004**, *2004*, 237.

[13] R. L. Vekariya, *J. Mol. Liq.* **2017**, *227*, 40.

[14] U. Geiser, J. A. Schlueter, *Chem. Rev.* **2004**, *104*, 5203.

[15] F. Grepioni, G. Cojazzi, S. M. Draper, N. Scully, D. Braga, *Organometallics* **1998**, *17*, 296.

[16] S. Lankalapalli, V. R. M. Kolapalli, *Indian J. Pharm. Sci.* **2009**, *71*, 481.

[17] P. Walden, *Bull. Acad. Imp. Sci. St. Petersbg.* **1914**, *8*, 405.

[18] O. Green, S. Grubjesic, S. Lee, M. A. Firestone, *Polym. Rev.* **2009**, *49*, 339.

[19] M. Armand, F. Endres, D. R. MacFarlane, H. Ohno, B. Scrosati, *Nat. Mater.* **2009**, *8*, 621.

[20] T. P. Thuy Pham, C.-W. Cho, Y.-S. Yun, *Water Res.* **2010**, *44*, 352.

[21] S. Sowmiah, V. Srinivasadesikan, M.-C. Tseng, Y.-H. Chu, *Molecules* **2009**, *14*, 3780.

[22] R. Giernoth, *Angew. Chemie - Int. Ed.* **2010**, *49*, 2834.

[23] W. Levason, D. Pugh, G. Reid, *New J. Chem* **2017**, *41*, 1677.

[24] K. N. Marsh, J. A. Boxall, R. Lichtenthaler, *Fluid Phase Equilib.* **2004**, *219*, 93.

[25] J. P. Armstrong, C. Hurst, R. G. Jones, P. Licence, K. R. J. Lovelock, C. J. Satterley, I. J. Villar-Garcia, *Phys. Chem. Chem. Phys.* **2007**, *9*, 982.

[26] M. Tariq, M. G. Freire, B. Saramago, J. A. P. Coutinho, J. J. Canongia Lopes, L. Luı´s, P. N. Rebelo, *Chem. Soc. Rev* **2012**, *41*, 829.

[27] N. V Plechkova, K. R. Seddon, *Chem. Soc. Rev.* **2008**, *37*, 123.

[28] D. Wei, A. Ivaska, *Anal. Chim. Acta* **2008**, *607*, 126.

[29] M. Gorlov, L. Kloo, *Dalt. Trans.* **2008**, 2655.

[30] A. N. Jordan, **2013**.

[31] D. K. Bwambok, B. El-Zahab, S. K. Challa, M. Li, L. Chandler, G. A. Baker, I. M. Warner, *ACS Nano* **2009**, *3*, 3854.

[32] P. E. Kolic, N. Siraj, M. Cong, B. P. Regmi, X. Luan, Y. Wang, I. M. Warner, *RSC Adv.* **2016**, *6*, 95273.

[33] A. N. Jordan, S. Das, N. Siraj, S. L. de Rooy, M. Li, B. El-Zahab, L. Chandler, G. A. Baker, I. M. Warner, *Nanoscale* **2012**, *4*, 5031.

[34] M. Born, A. Lande, *Verh. Dtsch. Phys. Ges.* **1918**, *20*, 210.

[35] E. Madelung, *Phys. Z.* **1918**, *19*, 524.

[36] D. Quane, *J. Chem. Educ.* **1970**, *47*, 396.

[37] M. Born, J. Mayer, *Phys. Z.* **1932**, *75*, 1.

[38] D. H. Templeton, *Cit. J. Chem. Phys.* **1953**, *21*, 2999.

[39] A. F. Kapustinskii, *Q. Rev. Chem. Soc.* **1956**, *10*, 283.

[40] G. J. Moody, J. D. R. Thomas, *J. Chem. Educ.* **1965**, *42*, 204.

[41] D. Borwein, J. M. Borwein, K. F. Taylor, *J. Math. Phys.* **1985**, *26*, 2999.

[42] A. Kapustinskii, *Z. Krist.* **1933**, *86*, 359.

[43] D. W. Smith, *J. Chem. Educ.* **1977**, *10*, 283.

[44] H. D. B. Jenkins, K. P. Thakur, *J. Chem. Educ.* **1979**, *56*, 576.

[45] T. E. Mallouk, G. L. Rosenthal, G. Müller, R. Brusasco, N. Bartlett, *Inorg. Chem* **1984**, *23*, 3167.

[46] H. D. B. Jenkins, H. K. Roobottom, J. Passmore, L. Glasser, *Inorg. Chem.* **1999**, *38*, 3609.

[47] L. Glasser, H. D. B. Jenkins, *J. Am. Chem. Soc.* **2000**, *122*, 632.

[48] L. Glasser, H. D. B. Jenkins, *J. Chem. Eng. Data* **2011**, *56*, 874.

[49] U. P. R. M. Preiss, J. M. Slattery, I. Krossing, *Ind. Eng. Chem. Res.* **2009**, *48*, 2290.

[50] L. Glasser, H. D. B. Jenkins, *Phys. Chem. Chem. Phys.* **2016**, *18*, 21226.

[51] E. I. Izgorodina, U. L. Bernard, P. M. Dean, J. M. Pringle, D. R. Macfarlane, **2009**, *9*, 4834.

[52] I. Krossing, J. M. Slattery, C. Daguenet, P. J. Dyson, A. Oleinikova, H. Weingärtner, *J. Am. Chem. Soc.* **2006**, *128*, 13427.

[53] J. D. Myers, J. Xue, *Polym. Rev.* **2012**, *52*, 1.

[54] A. Köhler, H. Bässler, *Electron. Process. Org. Semicond.* **2015**, 389.

[55] D. R. T. Zahn, G. N. Gavrila, M. Gorgoi, *Chem. Phys.* **2006**, *325*, 99.

[56] A. Mishra, P. Bäuerle, *Angew. Chemie Int. Ed.* **2012**, *51*, 2020.

[57] J. L. Brédas, J. P. Calbert, D. A. da Silva Filho, J. Cornil, *Proc. Natl. Acad. Sci. U. S. A.* **2002**, *99*, 5804.

[58] H. Kuhn, *J. Chem. Phys.* **1949**, *17*, 1198.

[59] J. Knoester, V. M. Agranovich, In *Thin Films and Nanostructures*; 2003; Vol. 31, pp. 1–96.

[60] S. Torabi, F. Jahani, I. Van Severen, C. Kanimozhi, S. Patil, R. W. A. Havenith, R. C. Chiechi, L. Lutsen, D. J. M. Vanderzande, T. J. Cleij, J. C. Hummelen, L. J. A. Koster, *Adv. Funct. Mater.* **2015**, *25*, 150.

[61] A. Köhler, H. Bässler, *Mater. Sci. Eng. R Reports* **2009**, *66*, 71.

[62] D. F. Swinehart, *J. Chem. Educ.* **1962**, *39*, 333.

[63] A. Köhler, J. S. Wilson, R. H. Friend, *Adv. Eng. Mater.* **2002**, *4*, 453.

[64] S. Reineke, M. A. Baldo, *Sci. Rep.* **2015**, *4*, 3797.

[65] T.-B. Ren, W. Xu, W. Zhang, X.-X. Zhang, Z.-Y. Wang, Z. Xiang, L. Yuan, X.-B. Zhang, *J. Am. Chem. Soc.* **2018**, *140*, 7716.

[66] J. N. Demas, G. a. Crosby, *J. Phys. Chem.* **1971**, *75*, 991.

[67] N. C. Greenham, I. D. W. Samuel, G. R. Hayes, R. T. Phillips, Y. A. R. R. Kessener, S. C. Moratti, A. B. Holmes, R. H. Friend, *Chem. Phys. Lett.* **1995**, *241*, 89.

[68] J. C. BERNÈDE, *J. Chil. Chem. Soc.* **2008**, *53*.

[69] H. Spanggaard, F. C. Krebs, *Sol. Energy Mater. Sol. Cells* **2004**, *83*, 125.

[70] G. A. A. Chamberlain, *Sol. Cells* **1983**, *8*, 47.

[71] C. W. Tang, *Appl. Phys. Lett.* **1986**, *48*, 183.

[72] A. Tada, Y. Geng, Q. Wei, K. Hashimoto, K. Tajima, *Nat. Mater.* **2011**, *10*, 450.

[73] V. Coropceanu, J. Cornil, D. A. da Silva Filho, Y. Olivier, R. Silbey, J.-L. Brédas, *Chem. Rev.* **2007**, *107*, 926.

[74] Z. Yin, J. Wei, Q. Zheng, *Adv. Sci.* **2016**, *3*, 1500362.

[75] S. R. Forrest, *Philos. Trans. R. Soc. A Math. Phys. Eng. Sci.* **2015**, *373*, 20140320.

[76] R. Jean, *Acc. Chem. Res.* **2009**, *42*, 1719.

[77] L. Lu, T. Zheng, Q. Wu, A. M. Schneider, D. Zhao, L. Yu, *Chem. Rev.* **2015**, *115*, 12666.

[78] F. Zhang, K. G. Jespersen, C. Björström, M. Svensson, M. R. Andersson, V. Sundström, K. Magnusson, E. Moons, A. Yartsev, O. Inganäs, *Adv. Funct. Mater.* **2006**, *16*, 667.

[79] F. Padinger, R. S. Rittberger, N. S. Sariciftci, *Adv. Funct. Mater.* **2003**, *13*, 85.

[80] M. C. Scharber, N. S. Sariciftci, *Prog. Polym. Sci.* **2013**, *38*, 1929.

[81] M. Wright, A. Uddin, *Sol. Energy Mater. Sol. Cells* **2012**, *107*, 87.

[82] M. Urbani, M. Grätzel, M. K. Nazeeruddin, T. Torres, *Chem. Rev.* **2014**, *114*, 12330.

[83] M. K. Nazeeruddin, J. Ko, M. Grätzel, In *Organic Nanomaterials*; John Wiley & Sons, Inc.: Hoboken, NJ, USA, 2013; pp. 579–597.

[84] A. Hagfeldt, G. Boschloo, L. Sun, L. Kloo, H. Pettersson, *Chem. Rev.* **2010**, *110*, 6595.

[85] K. Wang, C. Liu, T. Meng, C. Yi, X. Gong, *Chem. Soc. Rev.* **2016**, *45*, 2937.

[86] T. Ameri, G. Dennler, C. Lungenschmied, C. J. Brabec, *Energy Environ. Sci.* **2009**, *2*, 347.

[87] T. Kirchartz, P. Kaienburg, D. Baran, *J. Phys. Chem. C* **2018**, *122*, 5829.

[88] L. J. A. Koster, V. D. Mihailetchi, H. Xie, P. W. M. Blom, *Appl. Phys. Lett.* **2005**, *87*, 203502.

[89] C. Uhrich, D. Wynands, S. Olthof, M. K. Riede, K. Leo, S. Sonntag, B. Maennig, M. Pfeiffer, *J. Appl. Phys.* **2008**, *104*, 043107.

[90] D. Cheyns, J. Poortmans, P. Heremans, C. Deibel, S. Verlaak, B. P. Rand, J. Genoe, *Phys. Rev. B* **2008**, *77*, 165332.

[91] B. Qi, Q. Zhou, J. Wang, *Sci. Rep.* **2015**, *5*, 11363.

[92] B. Qi, J. Wang, *Phys. Chem. Chem. Phys.* **2013**, *15*, 8972.

[93] J. Yu, Y. Zheng, J. Huang, *Polymers (Basel).* **2014**, *6*, 2473.

[94] A. Armin, M. Velusamy, P. Wolfer, Y. Zhang, P. L. Burn, P. Meredith, A. Pivrikas, *ACS Photonics* **2014**, *1*, 173.

[95] D. Bahro, M. Koppitz, A. Mertens, K. Glaser, J. Mescher, A. Colsmann, *Adv. Energy Mater.* **2015**, *5*, 1501019.

Chapter 2 Increasing Photovoltaic Performance of an Organic Cationic Chromophore by Anion Exchange

Donatas Gesevičius,[a,f] Antonia Neels[b], Sandra Jenatsch[a], Erwin Hack[c], Stavros Athanasopoulos[d], Lucas Viani[e], Frank Nüesch[a,g] and Jakob Heier[a]

a. Laboratory for Functional Polymers, Swiss Federal Laboratories for Materials Science and Technology, Empa, Überlandstrasse 129, Dübendorf, Switzerland
b. Center for X-ray Analytics, Swiss Federal Laboratories for Materials Science and Technology, Empa, Überlandstrasse 129, Dübendorf, Switzerland
c. Laboratory for Transport at Nanoscale Interfaces, Swiss Federal Laboratories for Materials Science and Technology, Empa, Überlandstrasse 129, Dübendorf, Switzerland
d. Departamento de Física, Universidad Carlos III de Madrid, Avenida Universidad 30, 28911 Leganés, Madrid, Spain
e. Institute for Fluid Dynamics, Nanoscience and Industrial Mathematics, Universidad Carlos III de Madrid, Avenida Universidad 30, 28911 Leganés, Madrid, Spain
f. Institute of Chemical Sciences and Engineering, ISIC, Ecole Polytechnique Fédérale de Lausanne, EPFL, Station 6, CH-1015 Lausanne, Switzerland
g. Institut des Matériaux, Ecole Polytechnique Fédérale de Lausanne, EPFL, Station 6, CH-1015 Lausanne, Switzerland
E-mail: frank.nueesch@empa.ch

2.1 Declaration of Contribution

This chapter is an exact copy of the article in Advanced Science which was published online on the 5th of December 2017. Unless otherwise stated Donatas Gesevičius was responsible for all the experiments and practical work. In all cases the idea development, interpretation of results and the writing of the manuscript was performed by Donatas Gesevičius. Antonia Neels was responsible for X-Ray analysis. Sandra Jenatsch measured CELIV. Erwin Hack performed the ellipsometry measurement and ellipsometry raw data analysis. Stavros Athanasopoulos and Lucas Viani performed DFT calculations. Frank Nüesch and Jakob Heier were responsible for proofreading, submitting and moderating scientific discussions.

https://onlinelibrary.wiley.com/doi/abs/10.1002/advs.201700496

DOI: https://doi.org/10.1002/advs.201700496

Adv. Sci., 2018, **5**, 1700496.

2.2 Keywords

Cyanine dyes, organic photovoltaics, morphology, single crystals.

2.3 Abstract

A symmetrical cyanine dye chromophore was modified with different counteranions to study the effect on crystal packing, polarizability, thermal stability, optical properties, light absorbing layer morphology and organic photovoltaic (OPV) device parameters. Four sulfonate-based anions and the bulky bistriflylimide anion were introduced to the 2-[5-(1,3-dihydro-1,3,3-trimethyl-2H-indol-2-ylidene)-1,3-pentadien-1-yl]-1,3,3-trimethyl-3H-indolium chromophore using an Amberlyst®A26 (OH^- form) anion exchanger. Anionic charge distribution clearly correlates with device performance, whereby an average efficiency of 2% was reached in a standard bilayer organic solar. We give evidence that the negative charge of the anion distributed over a large number of atoms is significantly more important than the size of the organic moieties of the sulfonate charge carrying group. This provides a clear strategy for future design of more efficient cyanine dyes for OPV applications.

2.4 Introduction

Cyanine dyes are a class of organic salts, with a positively charged chromophore and a corresponding anion. A common structural leitmotif for cyanine dyes consists of a polymethine chain flanked by indolenine derivatives.[1–4] The first report on the synthesis of cyanine dyes dates back to 1856 and the first application of such organic salts was as colour sensitizer in photography.[5] Since then, more applications emerged in the field of life sciences as fluorescent marker reagents,[6,7] non-linear optics,[8,9] data storage in CD-R,[10–12] and as organic semiconductors in organic photovoltaic devices (OPV) and photodiodes.[3,13–18]

Symmetrical polymethine dyes usually contain two nitrogen flanking groups. The dye in this study is an indocyanine chromophore, which consists of two symmetrical indoles connected by a polymethine chain.[19,20] Traditionally Fisher indole synthesis with a phenylhydrazine and the corresponding 3-methyl-2-butanone as reactants has been used to form the half-dye.[21,22] This can then be connected via amine condensation of a malonaldehyde bis(phenylimine) hydrochloride to a chosen polymethine chain. In modern synthesis however, microwave reactors and “more green” routes have been developed to form the half-dyes,[23] resulting in a higher yield, shorter reaction times and less toxic reagents and side products.

For OPV applications, researchers have focused on tuning the HOMO-LUMO energy gap of the chromophore. The two major strategies to do this are increasing the length of the polymethine chain by adding vinylene groups or the introduction of new terminal heterocycles.[4]

The corresponding anion of an indocyanine is defined by the reaction process, which requires methylation of the indole ring nitrogen. Because this often results in unwanted halides or halogenates (Cl^-, I^-, ClO_4^-), techniques were introduced to substitute these small and hard (Cl^-) or partly redox active (I^-, ClO_4^-) anions. At the same time new features like enhanced thermal stability and solubility were introduced.[24] Salt metathesis using two-phase liquid/liquid systems is the most commonly used technique.[25–27] However, it often requires several purification steps either by recrystallization or column chromatography, which lowers the yield of the desired organic salt.

Cyanine dyes with symmetrical distribution of charge density between the two nitrogen atoms are characterized by zero bond length alternation and show a phenomenon called the cyanine limit.[28–30] Beyond a certain polymethine chain length, the symmetry of the electronic structure collapses. Similarly, the charge density of the chromophore can also be influenced by the corresponding anion. It was reported previously that especially hard and small anions can induce charge localisation.[31–33] Unfortunately the electronic properties of such a system cannot be predicted with the required accuracy from their delocalised analogue. The anions used in this work maintain the so-called ideal polymethine state, which is favourable for OPV applications.

Few reports have focused on the crystal structure and packing behaviour of cyanine-based organic salts.[27,34–37] To the best of our knowledge, none of these reports has connected crystal packing with thin film morphology and OPV performance data. The influence of anions based on antimonates and phosphates on OPV performance in bilayer cells,[13,16] mobility, exciton diffusion length and long-term stability[38] were discussed for a series of cyanine based organic salts. All these publications consider the near infrared region only, while counterion dependence of dyes absorbing in the visible region has rarely been investigated. Also, most salts require halogenated solvents for thin film fabrication.

In this study, we combine the products of tailored chemical engineering with the direct response from the application in OPV devices. We present a simple, general and effective ion exchange method, which does not require halogenated solvents and was not used before in cyanine dye chemistry. The method was applied on a series of sulfonates with different organic moieties and also on a bistriflylimide anion. The size of the organic moieties bound to the negative charge carrying sulfonate group varies, while in the bulky bistriflylimide anion negative charge is distributed over several atoms. These two types of counterions were chosen to study the influence of charge distribution on electronic properties of the dye.

2.5 Results and Discussion

2.5.1 General Ion Exchange Pathway

The small and hard halide anions in cyanine dye salts can have a negative influence on redox stability and charge delocalisation when applied in organic photovoltaic devices. To overcome this unfavourable effect, we exchanged the chloride anion in our starting material 2-[5-(1,3-dihydro-1,3,3-trimethyl-2H-indol-2-ylidene)-1,3-pentadien-1-yl]-1,3,3-trimethyl-3H-indolium chloride by redox stable organic sulfonates or the bistriflylimide. Hereafter we will denote these dyes as Cy5O$_3$SMe, Cy5O$_3$SPh, Cy5O$_3$SPhMe, Cy5O$_3$SNaphth, Cy5TFSI (**Figure 2:1**).

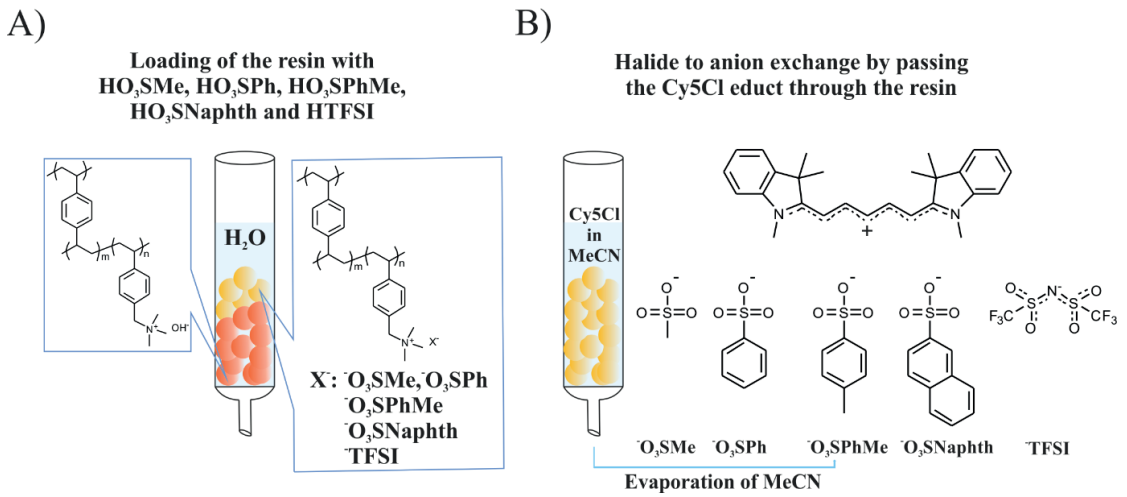

Figure 2:1 Schematic representation of the ion exchange procedure. A): The anion exchange resin is loaded with the corresponding anions. Acids are acting as anion source. B): A solution of the starting material is passed through the resin equilibrated with MeCN.

The target was to introduce a one-step ion exchange method that does not necessitate further purification steps, and that can be potentially scaled-up for industry. The Amberlyst® A26 (OH^- form) wet anion exchange resin was chosen for this purpose (**Figure 2:1A**). Sulfonic acids and bistriflylamine are strong acids with high dissociation degree. Therefore, the corresponding anions should behave like weak bases, a desired feature for an anion. The crosslinked styrene-divinylbenzene copolymer matrix functionalised with a quaternary ammonia moiety of the anion exchange resin preferably binds small and hard anions while the larger and softer ones are released. Direct loading of the resin from aqueous solutions of the corresponding acids was achieved with a capacity of 1.2 mmol of anion per 1 g of wet anion exchange resin. The process consists of an acid-base reaction giving water as a side product. Subsequently, after equilibration of the column with acetonitrile, salt metathesis occurs driven by the "Hard and Soft Lewis Acids and Bases" (HASAB) principle (**Figure 2:1B**). The ion exchange performed in this study is quantitative, and the chemically pure compounds are obtained after evaporation of all volatile compounds. The molecules were analysed by multicore NMR spectroscopy, elemental analysis and ion chromatography. A detailed description is provided in the ion exchange section of the supporting information. To the best of our knowledge this anion exchange method was applied for the first time in cyanine dye chemistry and can be expanded for a wider anion class such as carboxylates, amides, borates, nitrates or perchlorates.

2.5.2 Anion Influence on Thermal, Optical and Electrochemical Properties

The synthesised compounds have extraordinarily high relative extinction coefficients in the range of 3.45-3.60 x 10^5 L mol^{-1} cm^{-1}. The absorption band in ethanol solution ranges from 500 to 700 nm, which is attributed to π-π^* transitions (**Figure 2:2A**). A strong dependence on the anion regarding the peak shape and absorbance range becomes visible in UV-Vis spectra of 10 nm thick films (**Figure 2:2B**). In the solid state, the absorbance band broadens by about 4030 cm^{-1} and spans the range from 475 to 800 nm. This broadening is favourable for OPV applications and is caused to a significant extent by aggregation effects in the solid state. In ethanol solution, a vibronic shoulder shifted by 1070 cm^{-1} is visible, suggesting 0 → 0 transitions for the main peak and 0 → 1 or 0 → 2 transitions for the shoulders at shorter wavelengths caused by a dominant vibrational mode.[39] In spincast films the shoulder is blue shifted by about 1230 cm^{-1} and reaches almost the same intensity as the absorbance maximum, pointing towards dimerization as proposed in the literature.[40]

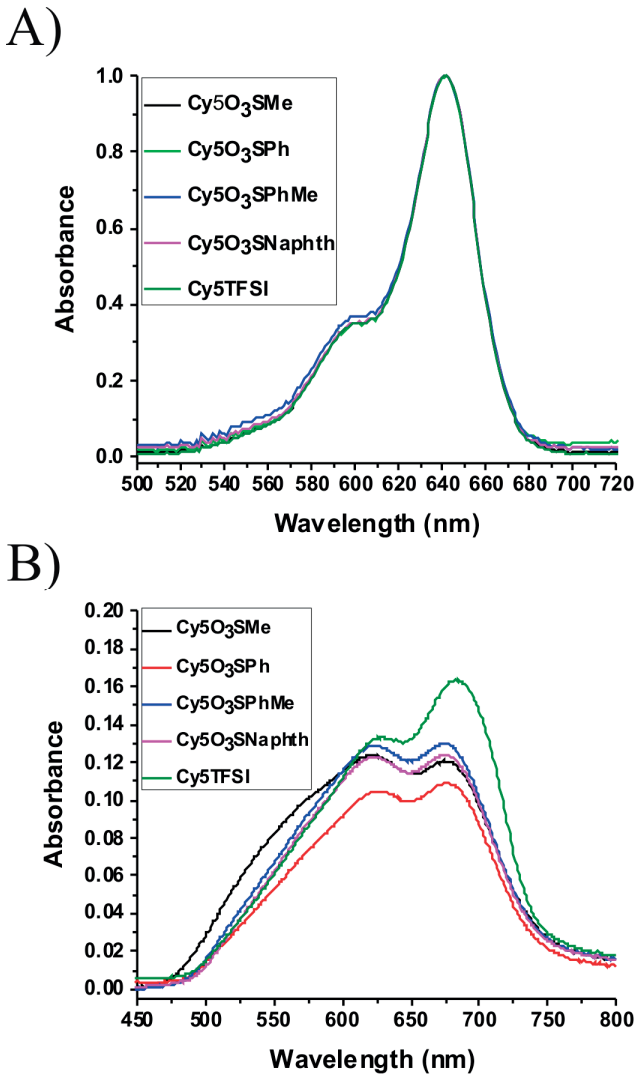

Figure 2:2 A) Normalized UV-Vis spectra of the cyanine dye salts from Ethanol solution, B) UV-Vis spectrum of 10 nm thick films in solid state. The chromophores with sulfonate anions were spincasted from ethanol solution, while TFP was used as a solvent for the Cy5TFSI compound.

The $Cy5O_3SMe$ compound shows an additional broad shoulder at shorter wavelengths, which may be a signature of H-aggregate formation. The absorbance maximum of Cy5TFSI is red shifted by 8.1 nm compared to the absorbance maxima of chromophores with

sulfonate anions, which could be caused by several synergy effects. Exciton-band shifts, stemming from head to tail orientation of transition dipole moments of neighbouring molecules, decreasing polarity of the Cy5TFSI and optical interference in thin films could lower the excitation energy. The unit cell of the corresponding crystal indeed shows such a molecular arrangement (**Figure 2:4D**). However, the HOMO-LUMO gap and the oscillator strengths obtained from ethanol solution spectra are not affected by the anion (**Table S5**). Notable is the smaller solid state optical band gap, mainly due to the absorbance broadening towards longer wavelengths. As expected, the anion does not influence the relative HOMO and LUMO energy levels of the chromophore in dimethylformamide solution. In all compounds an electrochemical energy gap of 1.39 eV was obtained. The anions themselves are not redox active within the potential window of the chromophore or C_{60}. With relative HOMO energy levels of -5.41±0.01 eV and LUMO energy levels of -4.03±0.01 eV, a high open circuit voltage can theoretically be expected (**Table S7**), even though the energy levels shift in the solid state.[38] In summary, optical absorbance, ellipsometry and cyclic voltammetry measurements (**Table S5, S7**) revealed that all synthesized organic salts are low band gap organic semiconductors, with high electron affinity and high positive oxidation potential. The observed properties render these compounds suitable candidates for donor materials in organic heterojunction solar cells. All synthesized compounds possess good relative thermal stability up to 250 °C (**Figure S3, Table S3**). Notable is the clear difference between sulfonate-based anions and the bulkier bistriflylimide, which manifests a decomposition temperature higher by 10 °C compared to the biggest sulfonate anion. From the smallest methylsulfonate to the biggest bistriflylimide anion the decomposition resistance increases even up to 30 °C. The mass losses observed for all chromophores with sulfonate anions in the temperature range between 60 and 120 °C suggests crystal water loss, which can be reconciled with results obtained from elemental analysis. At higher temperatures an atmospheric reaction occurs with Cy5TFSI and $Cy5O_3SNaphth$ compounds, this mass gain could be explained by adsorption of N_2 gas. All synthesised compounds show a two stage degradation, in which the integral of the first stage is of lower value than the integral of the second step. This suggests that the anion decomposes first, followed by a complex degradation of the dye backbone which occurs over a temperature range of more than 100 °C. It was not possible to identify and assign the degradation products with our thermal gravimetric analysis (TGA) setup. A clear increase of the relative decomposition temperature reflects the increasing stability of the organic salt by using anions with their negative charge distributed over several atoms.

2.5.3 Anion Influence on Crystal Packing, and Electronic Structure

Single crystals suitable for X-ray analysis could be obtained for four out of five compounds by cooling saturated solutions of the corresponding organic salts. All single crystals contained solvent molecules, and additionally, water molecules were found for $Cy5O_3SMe$. Solvent, water and disordered molecules as well as hydrogen atoms are omitted in **Figure 2:3 and Figure 2:4** for clarity. Symmetry lowering occurs with increasing size of the anion.

Table 2:1 Crystallographic parameters of the measured compounds. The R_1/wR_2 values represent the quality of the solved crystal model.

Anion	**^-O_3SMe**	**^-O_3SPh**	**$^-O_3SPhMe$**	**^-TFSI**
Crystal system	monoclinic	monoclinic	triclinic	triclinic
Space group	C2/c	$P2_1/c$	P-1	P-1
Unit cell volume/Å^3	18052	10222	1987	1650
R_1/wR_2/all data	0.0880/0.2821	0.1457/0.3179	0.0607/0.1777	0.0519/0.1253

A large influence of the anion on the chromophore backbone geometry can be observed. Two of the chromophores in $Cy5O_3SMe$ are almost planar (bending angles of 176°/175°) while one chromophore experiences a strong concave bending with an angle of 168° and additional tilt of the indolium rings with torsion angles between C13b-C14b-C15b-C16b of 176.1(5)° and between C6b-C7b-C8b-C9b of 177.8(5)° (**Figure S13, S14**, **Table S11**). In $Cy5O_3SPh$ the indolium rings of two chromophores are showing an anti-conformation with torsion angles between C13a/b-C14a/b-C15a/b-C16a/b of 177.4(4)°/177.4(4)° and between C6a/b-C7a/b-C8a/b-C9a/b of 176.5(4)°/179.5(4)°, while the third chromophore reveals an additional concave bending of 165° with a syn conformation of the nitrogen atoms. $Cy5O_3SPhMe$ shows an almost planar structure with torsion angles between C13-C14-C15-C16 of 178.7(4)° and C6-C7-C8-C9 of 177.3(3)°. The strongest concave bending of 143° and additional anti conformation of the indolium rings with torsion angles C13-C14-C15-C16/C6-C7-C8-C9 of 175.16(14)°/171.90(14)° occurs in Cy5TFSI. As expected, the negative charge in sulfonate based anions can be localised on one oxygen atom that has a significantly longer S-O distance, while in bistriflylimide the negative charge is delocalised over seven atoms according to the bond lengths (**Table S13**). Therefore, we observe a clear tendency to longer chromophore-anion contacts with increasing size of the organic moiety and charge delocalisation (**Figure 2:3, Table S14**).

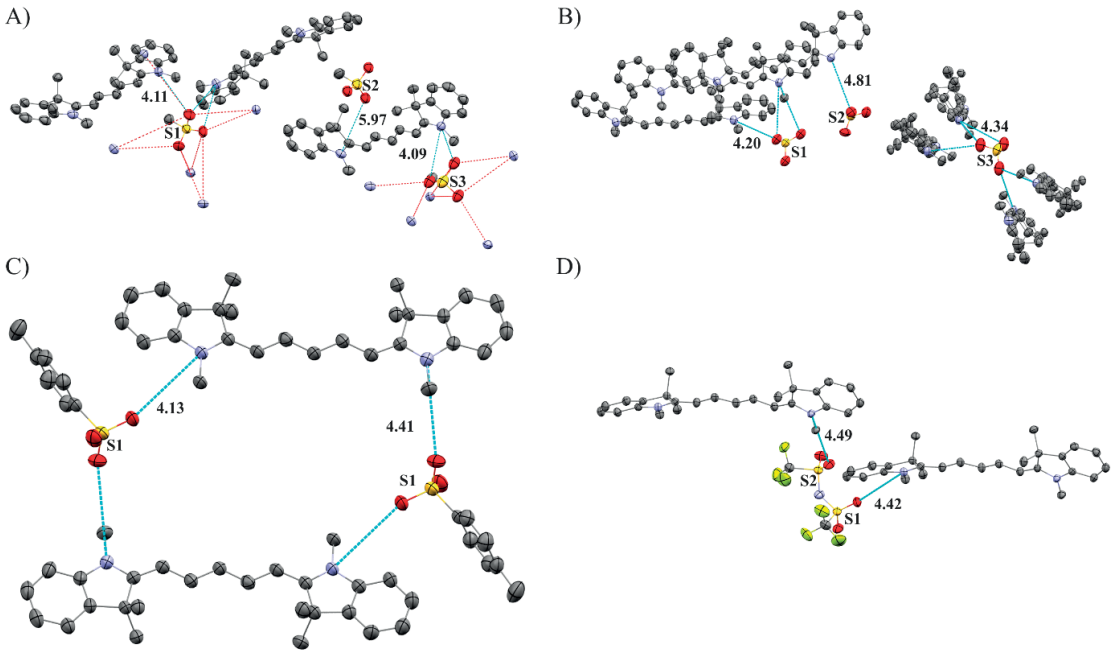

Figure 2:3 Anion coordination environment observed from single crystal data. The shortest anion-chromophore distances observed with Mercury are given in Å. A): $Cy5O_3SMe$, B): $Cy5O_3SPh$, C): $Cy5O_3SPhMe$, D): Cy5TFSI. The thermal ellipsoids represent 50% probability levels. All solvent and disordered molecules as well as hydrogen atoms are omitted for clarity. Additionally anionic contacts to the nitrogen atoms of surrounding chromophores are shown in the case of $Cy5O_3SMe$ and $Cy5O_3SPh$. In the case of $Cy5O_3Ph$ only the SO_3^- charge carrying group is shown for clarity. Color code: C: grey, N: violet, S: yellow, O: red, F: yellow-green.

In all crystal structures the anions are coordinating with the chromophore in a highly asymmetrical manner. However, a detailed insight into the coordination behaviour of the anions is more complex. The anions in $Cy5O_3SMe$ triplets cannot be assigned to one specific chromophore. Furthermore, similar anion coordination distances indicate overlapping electrostatic interactions within the triplet (**Figure 2:3A**). In fact, each anion triplet interacts with two chromophore triplets, due to the position of the anions within two chromophore triplet layers. The chromophores are arranged in sheets separated by layers of anions. Within these sheets the chromophores form a zigzag structure with an angle of 82° (**Figure 2:4A**). All methyl sulfonate anions are coordinating asymmetrically, with a broad variation for shortest anionic contact to a nitrogen atom (4.09-5.97 Å). Neighbouring chromophore molecules are stacked in staircase fashion, with shortest intermolecular carbon-nitrogen contacts between 3.57-3.69 Å for the indolium rings and carbon-nitrogen contacts between indolium ring and the polymethine chain of 3.62-3.64 Å as well as carbon-carbon contacts between two polymethine chains of 3.69 Å indicating weak π interactions (**Figure S14**). Stronger π stacking is prevented by the large tilt angle of 23° within the chromophore triplet, which results in large aromatic backbone carbon-carbon distances of over 6.25 Å. A similar behaviour can be found in $Cy5O_3SPh$ where the shortest anion contacts of the three anions lie between 4.20-4.80 Å (**Figure 2:3B**). The unit cell reveals a crossbone like packing, where each anion interacts with two chromophore triplets (**Figure 2:4B**). The chromophore triplets show a stacking similar to the one found in $Cy5O_3SMe$, even though the tilt angles within the chromophore triplets differ. Two chromophores are facing each other with a tilt of 24° while the third chromophore faces away with a tilt of 31°. Weak intermolecular π interactions can be found between indolium rings with shortest nitrogen to carbon contacts of about 3.46 Å as well as 3.54-3.66 Å nitrogen-carbon contacts between the indolium ring and the polymethine chain (**Figure S14**). These fluctuations in stacking angle and anion coordination distances found in $Cy5O_3SMe$ and $Cy5O_3SPh$ are also favoured by solvent intercalation effects. The number of chromophore interactions per anion is reduced to two in $Cy5O_3SPhMe$ and Cy5TFSI (**Figure 2:3C, 2:3D**). The *p*-methylphenylsulfonate shows 4.13 Å and 4.41 Å contacts to N1 and N2 of two different chromophores, while in Cy5TFSI the coordination distance increases to 4.51 Å and 4.49 Å for N1 and N2, respectively The slight decrease in dielectric constant (**Table S9**) can be correlated to the coordination distance of the anion, which reduces the polarizability. It can be assumed, that the strong geometrical distortions in the Cy5TFSI chromophore backbone are mainly caused by sterical effects of the bulky bistriflylimide anion (**Figure 2:4D**, **Table S12**). The anion slightly influences the charge localisation on the polymethine chain which can be visualised by the bond length alternation (BLA), which is here the difference between longest and shortest C-C bond length. All compounds show low bond

length alternation from 3.3 to 0.8 pm, with a general trend to lower values with increasing size and charge delocalisation of the anion (**Table S10**).

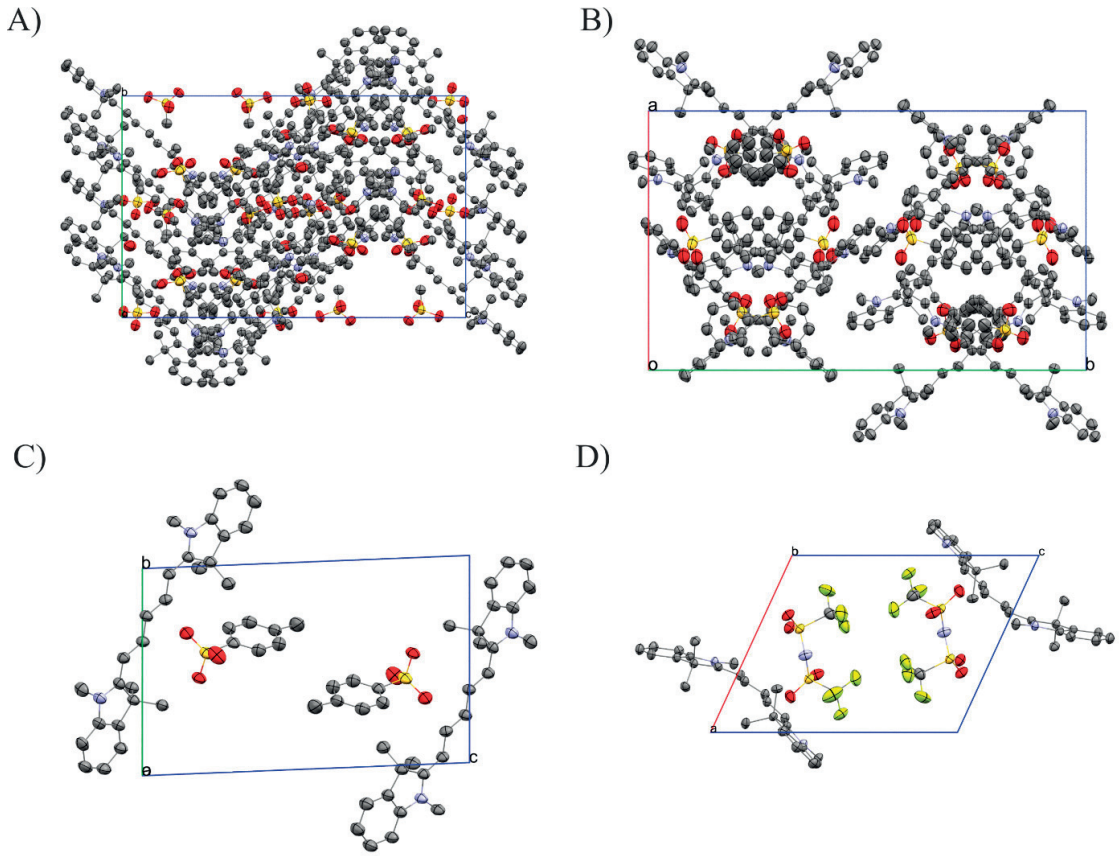

Figure 2:4 Anion influence on crystal packing, the thermal ellipsoids represent 50% probability levels. A): $Cy5O_3SMe$ along a axis, B): $Cy5O_3SPh$ packing along c axis, C): $Cy5O_3SPhMe$ packing along b axis, D): Cy5TFSI packing along b axis. All solvent and disordered molecules as well as hydrogen atoms are omitted for clarity. Color code: C: grey, N: violet, S: yellow, O: red, F: yellow-green.

The terminal nitrogen atoms show similar bond lengths between N1-C8 and N2-C14 in a range of 1.358(8)-1.361(6) Å, which is in agreement with the expected iminium fragment bond length. Notable is that the N1-C1 and N2-C21 bond lengths between 1.403(6) and 1.414(9) Å respectively, are in the range of an amine moiety, which indicates that the aromatic units of the indolium ring do not participate in the charge delocalisation (**Table S10**). Therefore, it can be assumed, that the electrons delocalised within the polymethine chain, which is terminated by the two nitrogen atoms of the indolium moieties, are forming the π-orbitals of the chromophore. With a low maximal BLA of 0.8 pm the polymethine chain of Cy5TFSI is delocalized, despite the strongest asymmetrical coordination of the $TFSI^-$ and strongest geometrical distortions of the chromophore backbone. This is in agreement with the expectation that a weakly coordinating anion should reduce interactions with the cation.

2.5.4 Anion Influence on Thin Film Morphology

To achieve uniform and defect-free thin films of 10 nm thickness of the dye on top of the hole transporting layer is a challenging task because the cyanines tend to crystalize or dewet by forming either dye droplets or micrometre sized aggregates. The best cyanine layer quality was achieved from environmentally friendly ethanol solutions for the sulfonate based salts, and from 2,2,3,3-tetrafluoro-1-propanol (TFP) for the bistriflylimide salt. Despite optimized spincoating conditions, the morphology of the spincast films differs significantly. The overall surface roughness parameters are low, though large differences in local surface morphology occur. The line profiles show local peaks or pinholes the number of which increases with decreasing size of the anion (**Figure 2:5**).

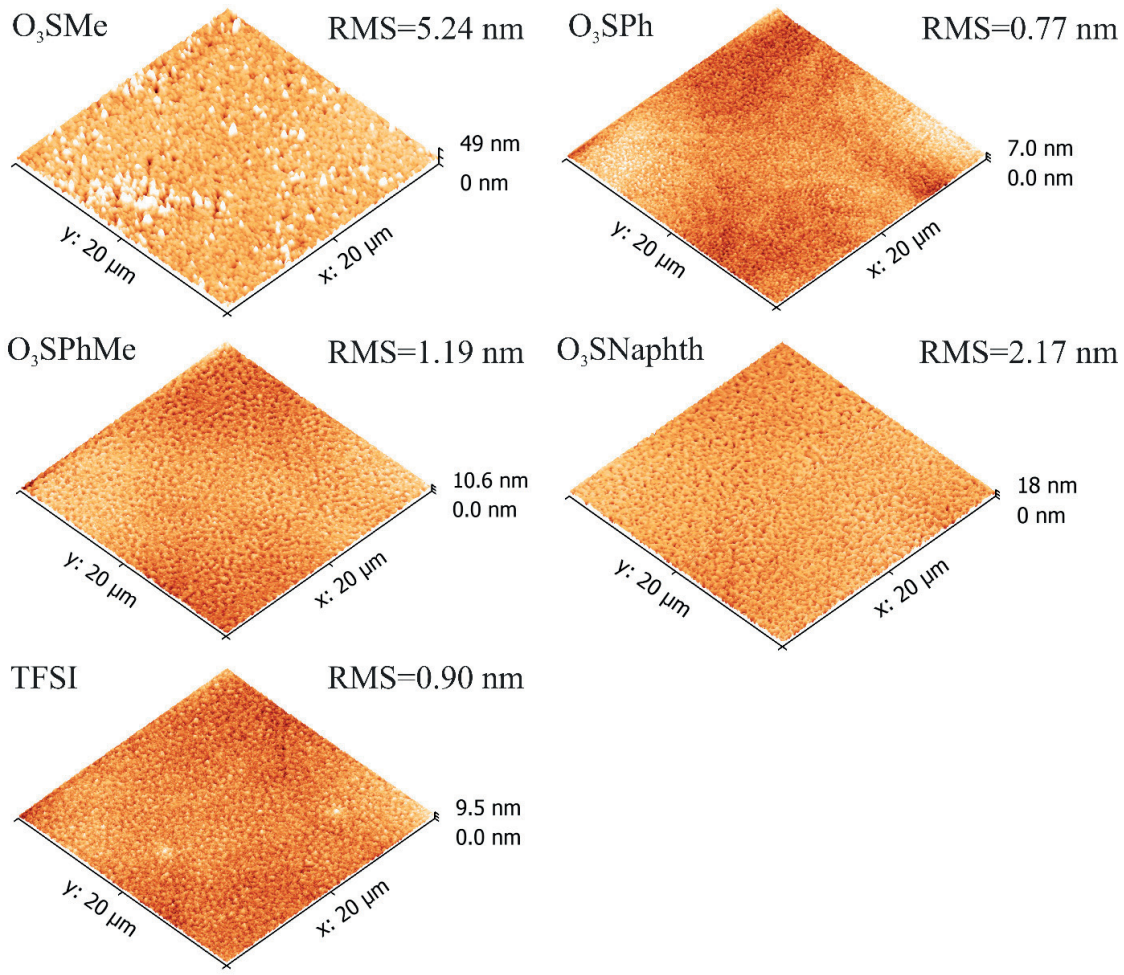

Figure 2:5 Topography of the active layer. The scanned area was fixed to 20·20 μm^2 for all compounds.

The 2-naphthalenesulfonate anion causes a pinhole rich surface, while the Cy5O_3SMe shows a local increase of dye layer thickness up to 40 nm. The smoothest pinhole and spike free surface is achieved with the bistriflylimide anion. Cy5O_3SPh and Cy5O_3SPhMe gave similar surfaces, which are slightly rougher compared to the Cy5TFSI surface. Based on AFM data, the smoothest and most defect free surfaces are obtained from dyes possessing the anion with larger negative charge delocalisation. However, the AFM study does not allow one to draw precise conclusions of the origin of the observed thin film morphologies. In principle, incompatibility in surface energy between the hole transport layer and the dye in combination with residual solvent traces, can cause dewetting processes. Also, dye aggregation caused by intermolecular π interactions cannot be excluded. The crystal packing diagram (**Figure 2:4A**) and the UV-Vis spectrum (**Figure 2:2B**) of the chromophore with the smallest methylsulfonate anion indicate strong aggregation behaviour, which could lead to locally thicker dye layers (**Figure 2:5 O_3SMe**). The AFM measurements allow the conclusion that a larger spacing between the chromophores, which is provided by introduction of large counterions, suppresses both dewetting phenomena and aggregate formation during spincasting.

2.5.5 Anion Influence on OPV Device Performance

All synthesized compounds were used as light absorbing materials in a bilayer organic photovoltaic device with standard geometry (**Figure S15**). Cy5O_3SPh, Cy5O_3SPhMe and Cy5O_3SMe OPV devices show large parasitic dark currents, in the range of 0.15-0.04 mA cm^{-2} at -0.8 V (**Figure 2:6B**). On the contrary, Cy5O_3SNaphth and Cy5TFSI OPV devices show low values of 0.001 mA cm^{-2} at -0.8 V. Occurrence of low parallel resistance produces alternative current pathways within the device, which results in low V_{OC} and J_{SC} values. Especially the V_{OC} of Cy5O_3SMe, Cy5O_3SNaptht and Cy5TFSI correlate with the roughness parameters of the thin film surface. A

clear distinction can be made between the sulfonate anions and the bistriflylimide regarding the OPV device parameters. The organic moiety size effect of the sulfonate anions enhances the V_{OC}, J_{SC}, FF and η by up to 35%, 15%, 15% and 79%, respectively, mainly due to improved morphology without spikes and pinholes (**Table 2:2**). Large improvement in all relevant OPV parameters occurs for the bistriflylimide which has negative charge delocalisation over several atoms. The OPV device with Cy5TFSI gives a relative increase of V_{OC}, J_{SC}, FF and η of up to 48%, 72%, 64% and 440% compared to the Cy5O_3SMe based device.

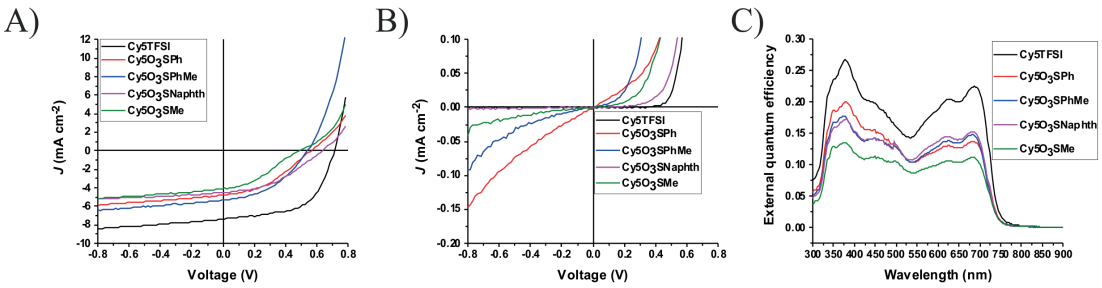

Figure 2:6 JV and EQE curves of the best performing OPV cells. A): Cells under light illumination, B): dark current measured right after fabrication, C): external quantum efficiency efficiency of aged devices (several weeks of storage in a glovebox).

Such a drastic increase in all relevant OPV parameters are not easy to explain by the very smooth active layer surface and large chromophore spacing alone. It can be speculated that several synergetic effects contribute substantially to the V_{OC} increase, like stronger stabilisation of the chromophore in the excited state by the TFSI anion and a HOMO energy level shift of the chromophore in the solid state towards a larger donor-acceptor energy gap. Similar findings regarding HOMO energy levels were observed by the group of *Lunt* performing ultraviolet photoelectron spectroscopy (UPS) on cyanine dye films.[38] Unfortunately all devices showed short term degradation with a more rapid decrease of the cyanine contribution to the external quantum efficiency (EQE) than for C_{60} (**Figure S20**). Nevertheless, the performance enhancement for Cy5TFSI devices aged for several weeks in the glovebox correlates with the external quantum efficiency, which reaches its maximum at 26% for the Cy5TFSI (**Figure 2:6C**). Notable is that the TFSI anion does influence the carrier mobility. The measured values are in the range of 10^{-5} cm^2 V^{-1} s^{-1} for high charge extraction rates which is higher than the mobilities obtained for salts with sulfonate anions (**Figure S9, S10**). This observation could expand the previously reported assumption that the hole mobility is mainly determined by the cation.[15] Despite good OPV data for the best Cy5TFSI cell, the devices suffer from large variations of the measured values from cell to cell (**Table 2:2**).

Table 2:2 Averaged OPV performance data for all investigated cells with the corresponding standard deviation of all measured cells.

Anion	N cells	Voc (V)	Jsc (mA cm^{-2})	FF (%)	Eff (%)
TFSI	32	0.68 ± 0.05	6.03 ± 0.49	51.53 ± 9.31	1.96 ± 0.57
O_3SNaphth	8	0.62 ± 0.05	4.94 ± 0.35	37.84 ± 1.8	1.13 ± 0.12
O_3SPhMe	6	0.51 ± 0.12	4.52 ± 0.42	41.5 ± 5.29	1.22 ± 0.33
O_3SPh	8	0.51 ± 0.02	4.43 ± 0.28	35.43 ± 1.62	0.98 ± 0.07
O_3SMe	8	0.46 ± 0.04	4.29 ± 0.16	35.05 ± 2.32	0.68 ± 0.05

A remarkable improvement of reproducibility is achieved with high vacuum treatment of the Cy5TFSI active layer before device assembly, suggesting a TFP solvent residue effect (**Table S16**). Similar findings were reported before when using TFP as solvent for spincoating.[41] Remaining variations are mainly due to the multistep manual fabrication process of the devices. Further improvement trials were applied to the best Cy5TFSI compound regarding thickness adjustment, annealing at different temperatures and investigation of solvent additive effects. They are presented in **Figure S16-S18**. As expected, with increasing thickness of the active layer all relevant OPV parameters decrease, especially the EQE (**Figure S19**). Such a drop can be caused by the increased resistance of the semiconducting film and exciton recombination. Therefore, 10 nm is the optimal film thickness for the Cy5TFSI, suggesting a short exciton diffusion length of approximately 10 nm.

2.5.6 Conclusion

Four sulfonate based anions with different organic moieties and the bistriflylimide anion were introduced to a 2-[5-(1,3-dihydro-1,3,3-trimethyl-2H-indol-2-ylidene)-1,3-pentadien-1-yl]-1,3,3-trimethyl-3H-indolium chromophore to study effects that are caused either by the size of the organic moiety or charge delocalisation. A two-step halide-for-anion exchange method was introduced, using

Amberlyst®A26 (OH^- form) anion exchange resin, yielding the desired cyanine salts quantitatively and in high purity, without the need of halogenated solvents. Single crystal data revealed trends in anion coordination distance, influence on cyanine backbone geometry, bond length alternation and molecular packing. Despite asymmetrical coordination the anions maintain the ideal polymethine state which is favourable for OPV applications. The materials have good optical properties and exhibit an appropriate energy level to the acceptor material and hole transport layer for application in OPV devices. Drastic enhancement of all relevant OPV parameters was observed when the bistriflylimide anion was used with a negative charge delocalisation over several atoms. The negative charge delocalisation effect of the anion significantly favours the ideal polymethine state, chromophore spacing, thermal stability, redox stability, smooth surfaces of thin films and charge carrier mobility. This initial study will allow us to design more efficient cyanine dyes for OPV applications in ongoing work.

2.6 Experimental Section

2.6.1 Materials and Methods

All chemicals and solvents were purchased from commercial sources (*Aldrich, VWR, FEW Chemicals, Kurt J. Lesker*) and used as received, unless otherwise stated. Reactions were carried out under air atmosphere using common lab glass ware. NMR multicore spectra were recorded on a *Bruker AV-400* spectrometer (^{1}H-NMR: 400 MHz, ^{13}C{^{1}H}-NMR: 100 MHz, ^{19}F{^{1}H}-NMR: 377 MHz). Chemical shifts (δ) are reported in ppm (parts per million) with the solvent residual signal (^{1}H/^{13}C{^{1}H}: 7.20/79 for $CDCl_3$) as reference. J coupling constants are given in Hz. Multiplicities are reported as singlet (s), doublet (d), triplet (t), quartet (q), multiplet (m). Elemental analysis data were obtained from the Micro Laboratory of ETH Zürich with the instrument *Leco TruSpec Micro* for C, H, N, S, F and O, while Cl was determined by ion chromatography. Thermal gravimetric analysis was recorded on a *Netzsch TG 209 F1*.

2.6.2 Device Fabrication and Characterisation

Glass/ITO substrates were cleaned in acetone (*VWR*, 99.5% GPR RECTAPUR), isopropanol (*VWR*, EMPLURA), ethanol (*VWR*, 99.5% AnalaR NORMAPUR®) detergent (Hellmanex® III, 2 wt% water solution) and finally washed four times with deionised water. Evaporation of MoO_3 (99.97%) as the hole transport layer and C_{60} (99.5%) electron acceptor as well as Tris(8-hydroxyquinolinato)aluminium (99.99%) diffusion blocking layer and silver (99.99%) as the top electrode were performed in a glovebox using vapour deposition techniques. The pressure in the evaporation chamber did not exceed $6x10^{-6}$ mbar. The deposition rate was kept constant at 0.1 Å s^{-1} The active light absorbing layer was spincoated at a constant speed of 4000 rpm for 1 min in the glovebox under nitrogen atmosphere. The corresponding dye solutions (**Figure S2, Table S2**) were prepared in the glovebox under nitrogen atmosphere and were filtrated over a 0.45 µm filter before spincasting. The cell areas were defined with 3.1 and 7.1 mm^2 by using a mask for cathode deposition. The solar cells were characterised under inert gas atmosphere on a calibrated solar simulator (Spectra Nova) using a Xe lamp with 100 mW cm^{-2} simulated AM1.5G solar irradiation. The light intensity was adjusted using a calibrated silicon reference cell from Rera Solutions. External quantum efficiency was performed on a SpeQuest RR-2100.

2.6.3 Further Characterisation

UV-Vis spectra were measured on a Varian Cary 50. Measurement of *n* and *k* was performed using a spectroscopic ellipsometer M2000-VI (J.A. Woollam). Hole mobility measurement was performed on a Paios 3 instrument from Fluxim AG. The AFM analysis was performed on a scanning probe microscope Nanosurf Mobile S in tapping mode. Cyclic voltammetry (CV) measurements were performed on a PGStat 30 potentiostat (Autolab) using a three cell electrode system (Au working electrode, Pt counter electrode and an Ag/AgCl reference electrode). Single crystal diffraction patterns were recorded on a Stoe Mark II-Imaging Plate Diffractometer System (Stoe & Cie, 2015) equipped with a graphite-monochromator. Data collection was performed at –100˚C using Mo-Kα radiation (λ = 0.71073 Å). The structures were solved by direct methods using the program SHELXS[1] and refined by full matrix least squares on F^2 with SHELXL[1]. The hydrogen atoms were included in calculated positions and treated as riding atoms using SHELXL-97 default parameters. All non-hydrogen atoms were refined anisotropically. CCDC 1556701, 1556700, 1556698, 1556699 contain the supplementary crystallographic data for $Cy5O_3SMe$, $Cy5O_3SPh$, $Cy5O_3SPhMe$, Cy5TFSI, respectively. These data can be obtained free of charge from The Cambridge Crystallographic Data Centre via www.ccdc.cam.ac.uk/data_request/cif. Detailed information about the background of the described experiments can be found in the supporting information.

2.7 Supporting Information

2.7.1 General Information

2.7.2 General Notation for this Work

- Dyes are Indole derivatives connected with a methine chain

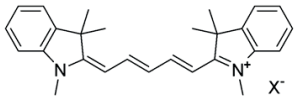

=Cy5X

2-[5-(1,3-dihydro-1,3,3-trimethyl-2H-indol-2-ylidene)-1,3-pentadien-1-yl]-1,3,3-trimethyl-3H-indolium

- Anions have sulfonates or imide as characteristic functional group

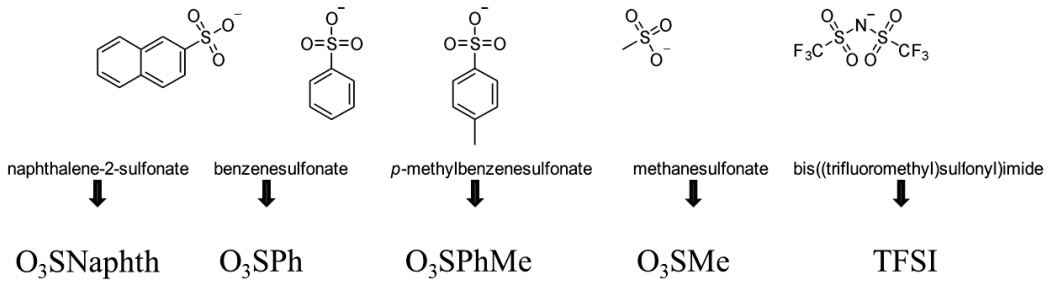

Figure S1. Overview of the used notation of the synthesized compounds for this work.

2.7.3 Anion Exchange Procedure

2.7.4 General Loading of the Resin

An appropriate amount of the wet anion exchange resin Amberlyst® A26 (OH^- form) was packed in a glass column (0.5 cm diameter). The column bed was then equilibrated with water until a constant pH value was reached. Then a 1% water solution of the corresponding acid was passed through the column until the eluate had reached the same pH as the original acid solution. During anion loading a change in colour of the resin from pink to pale yellow was obtained.

The pH changed from approximately 5 to 2. Then the resin was washed with water until constant pH was reached and equilibrated with the selected solvent media used for anion exchange. For the anion exchange a 1% solution of the Cy5Cl in the selected solvent mixture was passed through the column. After evaporation of the solvent the obtained residue was dried in FV. All steps were carried out at room temperature using gravity as driving force. For the regeneration of the resin a 1 mol/L solution of NaOH was passed through the column until constant pH (12), and then washed with water again until constant pH (5).

2.7.5 Determination of Resin Capacity

0.1723 g (1.79 mmol) of $MeSO_3H$ 1% water solution was prepared and passed through the column. After washing of the resin with water until constant pH the amount of unspent acid was determined by volumetric titration. 0.2014 mol/L NaOH solution was prepared as titrant, 3',3''-Dibromthymolsulfonphthaleine was used as indicator.

Table S1. Summarized data from the volumetric titration.

Compound	NaOH	$MeSO_3H$
Starting amount (g)	0.2014	0.1723
Starting volume (mL)	25	-
Starting mole (mmol)	5.04	1.79
Volume titrant used (mL)	2.8	-
n used (mmol)	0.564	-
n unspent (mmol)	-	0.564

$$C_{resin} = \frac{n_{acid} - n_{acid\ unspent}}{m_{resin}} = \frac{1.79\ mmol - 0.56\ mmol}{1\ g} = 1.2\ mmol\ g^{-1}$$

C_{resin} = capacity of the resin, n_{acid} = mole before column, $n_{acid\ unspent}$ = mole after column, m_{resin} = amount of wet anion exchange resin Amberlyst® A26 (OH^- form).

2.7.6 Synthesis of Cy5O3SMe x H_2O

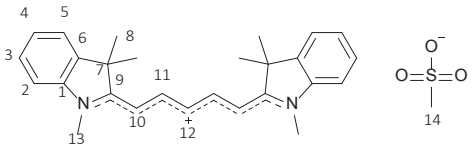

0.25 g of Cy5Cl solved in 100 mL MeCN were passed through 0.5 g of the anion exchange resin loaded with the Methanesulfonate. After evaporation of the solvent and drying for 24 h at $9.3x10^{-3}$ mbar a shiny blue solid was obtained. Yield: quantitative.

For X-Ray analysis suitable crystals were obtained by slowly cooling of a saturated chlorobenzene solution.

[$C_{28}H_{35}N_2O_4S$] 495.66 g mol^{-1}

^{1}H NMR (400 MHz, Chloroform-*d*) δ: 8.07 (t, *J* = 13.1 Hz, 2H, H(11)), 7.40 – 7.37 (m, 2H, H(3), 7.37 – 7.33 (m, 2H, H(5)), 7.21 (td, *J* = 7.5, 0.8 Hz, 2H, (4)), 7.11 (d, *J* = 7.9 Hz, 2H, H(2)), 6.82 (t, *J* = 12.5 Hz, 1H, H(12)), 6.33 (d, *J* = 13.7 Hz, 2H, H(10)), 3.70 (s, 6H, (H13)), 2.85 (s, 3H, H(14)), 1.71 (s, 12H, H(8)), 1.66 (s, 2H, H_2O) ppm.

^{13}C NMR (101 MHz, Chloroform-*d*) δ: 173.4 (C9), 153.9 (C11), 142.9 (C1), 141.0 (C6), 128.7 (C3), 126.6 (C4), 125.2 (C12), 122.20 (C5), 110.6 (C2), 104.0 (C10), 49.3 (C7), 39.8 (C14), 31.9 C(13), 28.0 (C8) ppm.

Elemental analysis: Calculated: [C] 67.71, [H] 7.31, [N] 5.64, [O] 12.89, [S] 6.46.

Found: [C] 67.71, [H] 7.28, [N] 5.54, [O] 11.05, [S] 6.43.

2.7.7 Synthesis of Cy5O3SPh

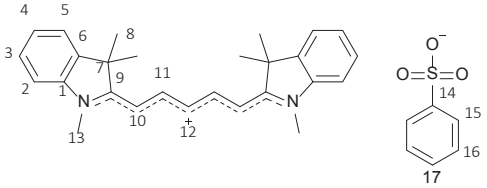

0.25 g of Cy5Cl solved in 100 mL MeCN were passed through 0.5 g of the anion exchange resin loaded with the Phenylsulfonate. After evaporation of the solvent and drying for 24 h at 9.3x10^{-3} mbar a shiny blue solid was obtained. Yield: quantitative.

For X-Ray analysis suitable crystals could be obtained by slow evaporation of benzene. The greenish shiny needles formed on the vial bottom.

[$C_{33}H_{35}N_2O_3S$] 539.71 g mol^{-1}

^{1}H NMR (400 MHz, Chloroform-*d*) δ: 8.18 (t, *J* = 12.9 Hz, 2H, H(11)), 8.09 – 7.99 (m, 2H, H(15)), 7.34 (m, 6H, H(3,5,17,18), 7.20 (t, *J* = 7.4 Hz, 2H, H(4)), 7.09 (d, *J* = 7.9 Hz, 2H, H(2)), 6.79 (d, *J* = 12.5 Hz, 1H, H(12)), 6.30 (d, *J* = 13.7 Hz, 2H, H(10)), 3.67 (s, 6H H(13)), 1.69 (s, 12H, H(8)) ppm.

^{13}C NMR (101 MHz, Chloroform-*d*) δ: 173.4 (C9), 154.1 (C11), 147.8 (C14), 142.9 (C1), 141.0 (C6), 128.7 C(17), 128.6 (C3) 127.8 C(16), 126.6 (C4), 126.57 C(15), 125.1 (C12), 122.2 (C5), 110.5 (C2), 104.0 (C10), 49.3 (C7), 31.9 C(13), 27.9 C(8) ppm.

Elemental analysis: calculated [C] 70.94, [H] 6.85, [N] 5.01, [O] 11.45, [S] 5.74.

Found [C] 70.89, [H] 6.64, [N] 4.82, [O] 10.29, [S] 5.57.

2.7.8 Synthesis of $Cy5O_3SPhMe$

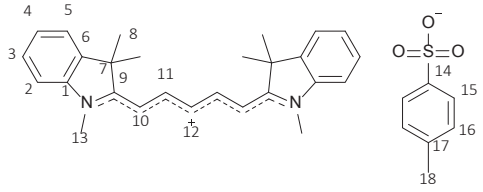

0.25 g of Cy5Cl solved in 100 mL MeCN were passed through 0.5 g of the anion exchange resin loaded with the *para* methyphenyll-sulfonate. After evaporation of the solvent and drying for 24 h at 9.3x10^{-3} mbar a shiny blue solid was obtained.

For X-Ray analysis suitable crystals were obtained by slowly cooling of a saturated benzene solution.

[$C_{36}H_{43}N_2O_3S$] 583.81 g mol^{-1}

^{1}H NMR (400 MHz, Chloroform-*d*) δ: 8.09 (t, *J* = 13.1 Hz, 2H, H(11)), 7.99 – 7.82 (m, 2H, H(15)), 7.44 – 7.28 (m, 4H, H(3,5)), 7.20 (td, *J* = 7.5, 0.9 Hz, 2H, H(4)), 7.13 (d, *J* = 7.9 Hz, 2H, H(16)), 7.08 (d, 7.9 Hz, 2H, H(2)) 6.80 (t, *J* = 12.5 Hz, 1H, H(12)), 6.30 (d, *J* = 13.6 Hz, 2H, H(10)), 3.66 (s, 6H, H(13)), 2.32 (s, 3H, H(18)), 1.66 (s, 12H, H(8)) ppm.

^{13}C NMR (101 MHz, Chloroform-*d*) δ: 173.3 (C9), 154.1 (C11), 145.0 (C14), 142.9 (C1), 140.9 (C6), 138.3 (C17), 128.6 (C16), 128.3 (C3), 127.01 (C4) 126.7 (C15), 125.0 (C12), 122.1 (C5), 110.5 (C2), 104.0 (C10), 49.2 (C7), 31.9 (C13), 27.9 (C8), 21.3 (C18) ppm.

Elemental analysis: calculated [C] 73.61, [H] 6.90, [N] 5.05, [O] 8.65, [S] 5.78.

Found [C] 73.49, [H] 6.94, [N] 4.84, [O] 9.04, [S] 5.34.

2.7.9 Synthesis of Cy5O3SNaphth x H2O

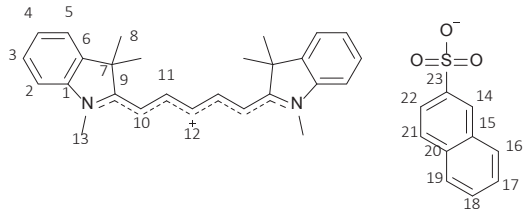

0.25 g of Cy5Cl solved in 100 mL MeCN were passed through 0.5 g of the anion exchange resin loaded with the *2*-Naphthalenesulfonate. After evaporation of the solvent and drying for 24 h at 9.3x10^{-3} mbar a shiny blue solid was obtained. Yield: quantitative.

[$C_{37}H_{38}N_2O_3S$] 590.78 g mol^{-1}

^{1}H NMR (400 MHz, Chloroform-*d*) δ: 8.58 – 8.50 (bs, 1H, H(14)), 8.13 (dd, *J* = 8.6, 1.7, 1H, H(22) 8.10 (t, *J* = 13.3 Hz, 2H, H(11), 7.90 – 7.82 (m, 2H, H(16,19)), 7.79 (dd, *J* = 7.7, 3.8 Hz, 1H, H(21)), 7.49 – 7.39 (m, 2H, H(18,17)), 7.32 (td, *J* = 7.9, 1.3 Hz, 2H, H(3)), 7.24 (d, *J* = 1.2 Hz, 2H, H(5)), 7.17 (td, *J* = 7.4, 0.9 Hz, 2H, H(4)), 7.05 (d, *J* = 7.9 Hz, 2H, H(2)), 6.74 (t, *J* = 12.4 Hz, 1H, H(12)), 6.25 (d, *J* = 13.7 Hz, 2H, H(10)), 3.61 (s, 6H, H(13)), 1.91 (s, 2H, H_2O), 1.64 (s, 12H, H(8)) ppm.

^{13}C NMR (101 MHz, Chloroform-*d*) δ: 173.4 (C9), 154.1 (C11), 144.9 (C23), 142.9 (C1), 141.0 (C6), 133.6 (C20), 132.9 (C15), 128.8 (C19), 128.5 (C3), 127.6 (21), 127.6 (C16), 126.5 (C12), 126.1 (C18), 125.8 (C17), 125.5 (14) , 124.6 (C22) 124.8 (C4), 122.2 (C5), 110.5 (C2), 104.0 (10), 49.3 (C7), 31.9 (C13), 27.9 (C8) ppm.

Elemental analysis: calculated [C] 73.00, [H] 6.62, [N] 4.60, [O] 10.51, [S] 5.27.

Found [C] 72.98, [H] 6.56, [N] 4.47, [O] 10.27, [S] 4.98.

2.7.10 Synthesis of Cy5TFSI

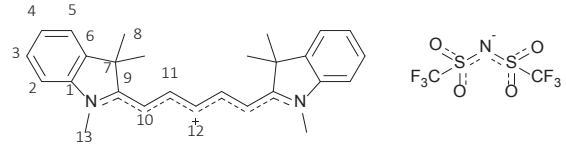

0.25 g of Cy5Cl solved in 100 mL MeCN were passed through 0.5 g of the anion exchange resin loaded with the bis(trifluoromethane)sulfonimide. After evaporation of the solvent and drying for 24 h at 1.9x10^{-2} mbar a shiny blue solid was obtained.

For X-Ray analysis suitable crystals were obtained by slowly cooling of a saturated ethylacetate solution.

[$C_{29}H_{31}F_6N_3O_4S_2$] 663.39 g mol^{-1}

^{1}H NMR (400 MHz, Chloroform-*d*) δ: 7.90 (t, *J* = 13.1 Hz, 1H, H(11)), 7.42 – 7.37 (m, 2H, H(3)), 7.37– 7.34 (m, 2H, H(5)), 7.25 (d, *J* = 7.5 Hz, 2H, H(4)), 7.13 (t*, *J* = 7.9 Hz, 2H, H(2)), 6.71 (t, *J* = 12.5 Hz, 1H, H(12)), 6.24 (d, *J* = 13.6 Hz, 2H, H(10)), 3.63 (s, 6H, H(13)), 1.72 (s, 12H, H(8)) ppm. *overlap with solvent signal.

^{13}C NMR (101 MHz, Chloroform-*d*) δ: 173.4 (C9), 153.4 (C11), 142.7 (C1), 140.9 (C6), 128.7 (C3), 126.37 (C4), 125.3 (C12), 122.2 (C5), 120.2 (q, J = 322 Hz, (CF_3)) 110.4 (C2), 103.8 (C10), 49.3 (C7), 31.4 (C13), 27.9 (C8) ppm.

^{19}F NMR (377 MHz, Chloroform-*d*) δ: -78.7 (s, 6F) ppm.

Elemental analysis: calculated [C] 52.48, [H] 4.71, [N] 6.33, [O] 9.64, [S] 9.66, [F] 17.17.

Found [C] 52.31, [H] 4.66, [N] 6.24, [O] -, [S] 9.72, [F] 17.20.

2.7.11 Thin Film Morphology and Thickness Evaluation

2.7.12 Screening of Suitable Solvents on Glass/MoO_3 Substrate

A 20 nm layer of MoO_3 was evaporated on glass to simulate real device conditions. All dyes were spincoated on these glass/MoO_3 substrates from preselected solvents and investigated with AFM.

2.7.13 Determination of Resulting Film Thicknesses After Solution Spincoating

UV-Vis spectra showed different values of absorptivity's in processed films despite that the initial dye concentration was kept constant. Obviously the usage of different solvents produces different films thicknesses. This makes tuning of individual film thicknesses necessary for each dye-solvent system. Ellipsometry was chosen as a measurement technique **(Figure S11, S12**). The used substrate is a 1 mm thick microscopic glass coated with a 20 nm MoO_3 layer. The aim is to find the right concentration for each dye that gives 10 nm thick films on MoO_3 layers. For all dyes the chosen spin coating speed was 4000 rpm for 60 sec.

Table S2. Thickness-concentration dependence for the compounds. *Determined only from that concentration.

c (mol L^{-1})	M_{dye} (g mol^{-1})	m_{dye} (mg)	$V_{Solv.}$ (mL)	d_{film} (nm)	$n_{\lambda(683\ nm)}$	$k_{\lambda(683\ nm)}$
Cy5O$_3$SPh*(H$_2$O) from Ethanol						
1*10^{-3}	558.74	0.4	0.7	4.0		
5*10^{-3}	558.74	2.0	0.7	13.9		
7.38*10^{-3}	558.74	2.9	0.7	24.4		
1*10^{-2}	558.74	3.9	0.7	40.0	2.57*	1.11*
Cy5O$_3$SPhMe from Ethanol						
1*10^{-3}	554.75	0.4	0.7	6.0		
5*10^{-3}	554.75	1.9	0.7	15.4		
7.38*10^{-3}	554.75	2.9	0.7	21.1		
1*10^{-2}	554.75	3.9	0.7	29.3	2.57*	1.13*
Cy5O$_3$SNaphth*(H$_2$O) from Ethanol						
1*10^{-3}	608.80	0.4	0.7	4.1		
5*10^{-3}	608.80	2.1	0.7	18.5		
7.38*10^{-3}	608.80	3.2	0.7	20.3		
1*10^{-2}	608.80	4.3	0.7	33.3	2.56*	1.17*
Cy5O$_3$SMe*(H$_2$O) from Ethanol						
1*10^{-3}	496.67	0.4	0.7	5.3		
5*10^{-3}	496.67	1.7	0.7	13.1		
7.38*10^{-3}	496.67	2.6	0.7	19.6		

c (mol L^{-1})	M_{dye} (g mol^{-1})	m_{dye} (mg)	$V_{Solv.}$ (mL)	d_{film} (nm)	$n_{\lambda(683\ nm)}$	$k_{\lambda(683\ nm)}$
1*10^{-2}	496.67	3.5	0.7	26.0	2.58*	1.01*
			Cy5TFSI from TFP			
1*10^{-3}	663.69	0.5	0.7	1.4		
5*10^{-3}	663.69	2.3	0.7	9.7		
7.38*10^{-3}	663.69	3.4	0.7	14.4		
1*10^{-2}	663.69	4.7	0.7	18.7	2.54*	1.24*

The obtained thickness values were plotted against concentration. With the linear fit equation it is possible to determine the concentration of a dye needed for a certain film thickness on a glass/MoO_3 substrate.

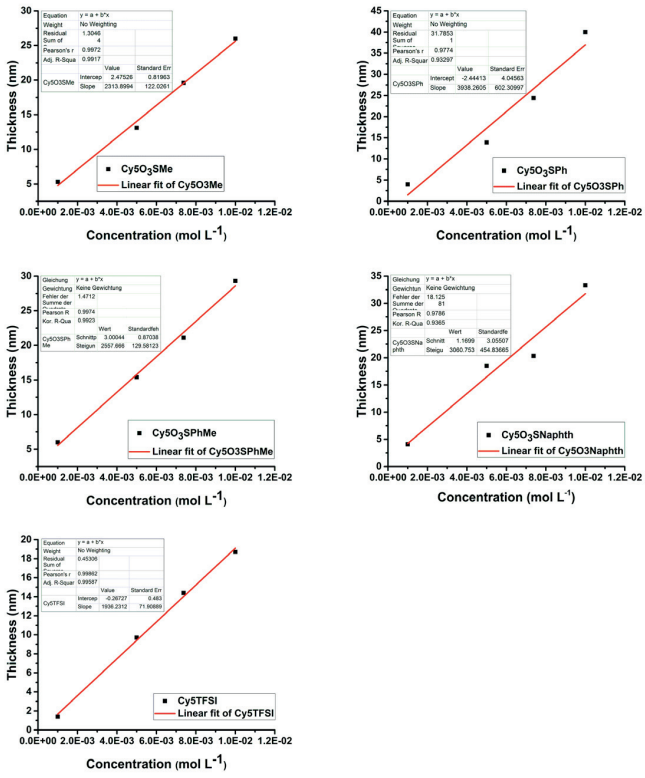

Figure S2. Thickness as a function of concentration for the used cyanines on glass/MoO_3 substrate.

2.7.14 Thermal Behaviour of the Dyes

The samples were weighed under air atmosphere, while the measurement was performed under nitrogen flow in a temperature range from 20-600 °C. From 600-900 °C the sample was exposed to oxygen.

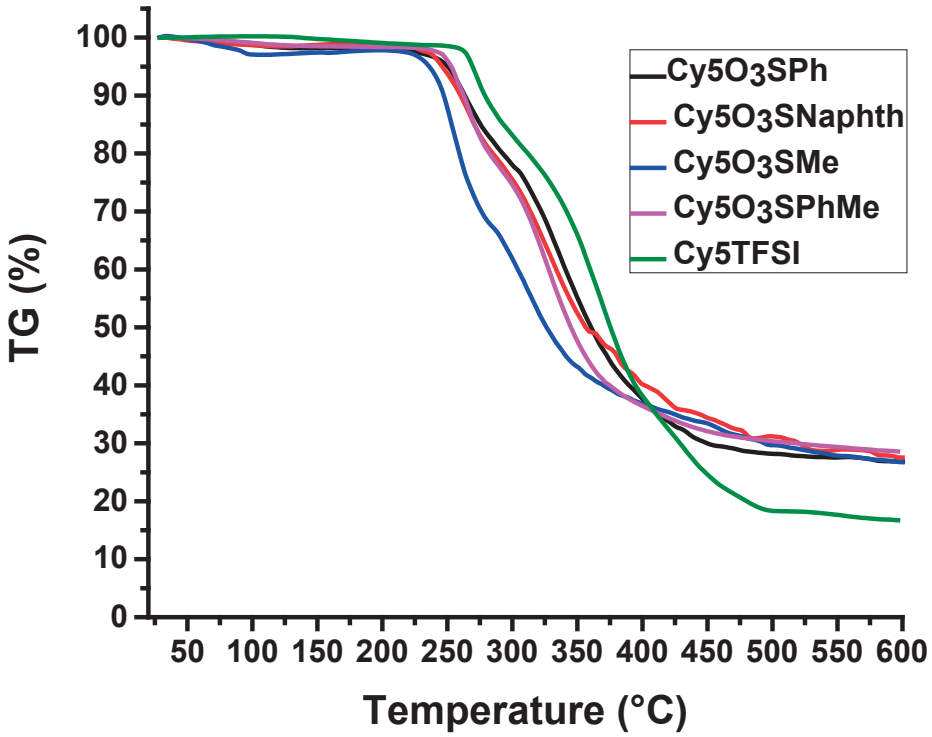

Figure S3. TGA curves of the compounds.

Table S3. Decomposition temperatures and calculated integrals from the TGA data.

Cyanine	Decomp. Temp/°C	First step (Mid-point)	First step Integral	Second step (Mid-point)	Second step Integral
Cy5O$_3$SPh *(H$_2$O)	235	235-302 (263)	21	302-600 (337)	51
Cy5O$_3$SPhMe	250	250-286 (267)	21	286-600 (329)	50
Cy5O$_3$SNaphth*(H$_2$O)	240	240-280 (261)	18	280-600 (310)	43
Cy5O$_3$SMe*(H$_2$O)	230	230-283 (253)	30	283-600 (310)	41
Cy5TFSI	260	260-305	19	305-600 (370)	65

Cyanine	Decomp. Temp/°C	First step (Mid-point)	First step Integral	Second step (Mid-point)	Second step Integral
		(271)			

2.7.15 UV-Vis absorbance

To determine the molar extinction coefficient ethanolic solutions of the cyanine compounds of 6.37 x 10^{-4} mol/L each were prepared. Subsequently solutions with three different concentrations were prepared by diluting the initial solution (**Table S4**).

Table S4. Used concentrations for the generation of calibration points in UV-Vis.

Solution	Compound concentration c (mol L^{-1})				
	Cy5O$_3$SMe *(H_2O)	**Cy5O$_3$SPh *(H_2O)**	**Cy5O$_3$SPhMe**	**Cy5O$_3$SNaphth *(H_2O)**	**Cy5TFSI**
1	3.469x10^{-7}	4.550x10^{-7}	7.341x10^{-7}	6.184x10^{-7}	4.927x10^{-7}
2	1.363x10^{-6}	1.539x10^{-6}	1.783x10^{-6}	1.262x10^{-6}	9.352x10^{-6}
3	2.393x10^{-6}	3.509x10^{-6}	4.123x10^{-6}	3.168x10^{-6}	2.363x10^{-6}

All measurements were performed in a 0.1 mm quartz glass cuvette using 99.8 % ethanol as reference for the baseline. The relative molar extinction coefficient for each compound was calculated by dividing the slope of the resulting plots of concentration against absorbance intensity by 10^{-1} cm.

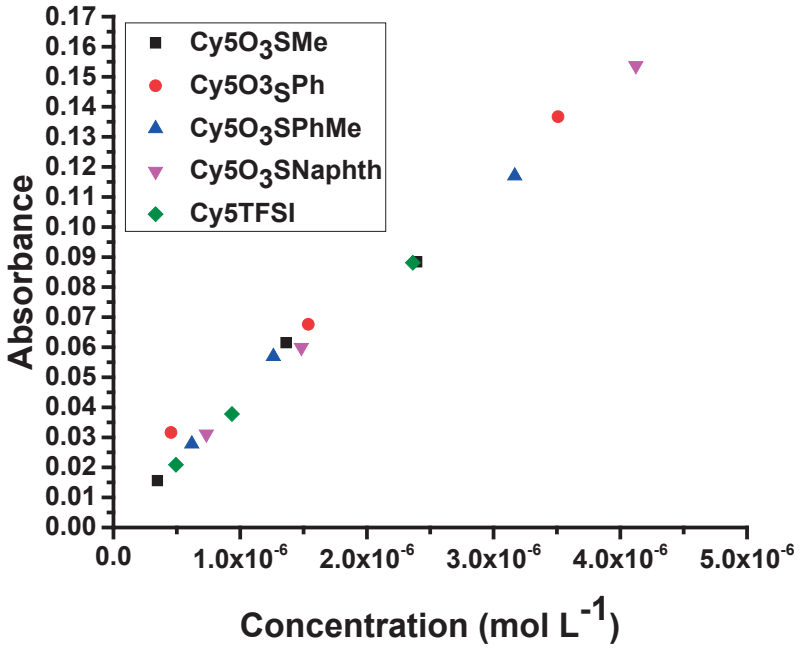

Figure S4. Concentration dependent absorbance.

The calculated extinction coefficients are summarized in **Table S5**. Since the cyanine dyes are known for the large exciton binding energy which results in strong bounded electron-hole pairs it, becomes clear that the optical bandgap and the electronic bandgap energies differ. A photon can have enough energy to create an exciton but not enough to separate the exciton into free electron and hole, so that the optical bandgap energy is much lower than the electrical band gap energy. The optical band gap can be calculated from the onset of the absorbance at higher wavelengths with the following equation.

$$\mathrm{E_{g(opt)}} = \frac{\mathrm{h \times c}}{\lambda_{\mathrm{onset}}}$$

λ_{onset}: Onset of absorption band at higher wavelength, h: Planck constant, c: speed of light.

One further value helpful to predict the excited state behaviour is the oscillator strength. The oscillator strength describes the probability of a transition from a lower to an upper energy state. The higher the value the easier the electrons can be excited and the stronger absorbing is the dye.

$$f = 4.319 \times 10^{-9} \int \varepsilon(\upsilon)\, d\upsilon$$

$\varepsilon(\upsilon)$: Molar extinction coefficient as a function of wavenumber, υ: Wavenumber.

First the wavelength was converted into wavenumbers with the following formula:

$$\upsilon = 1/(\lambda * 10^{-7})$$

Then the extinction coefficient was calculated for each wavenumber with the following formula:

$$\varepsilon_{(\upsilon)} = A/(c * d)$$

c: concentration in mol·L^{-1}, d: thickness of cuvette in cm, A: absorbance.

The calculations were performed for each recorded data point of the spectra. The resulting values were plotted, the wavenumber scale is reversed.

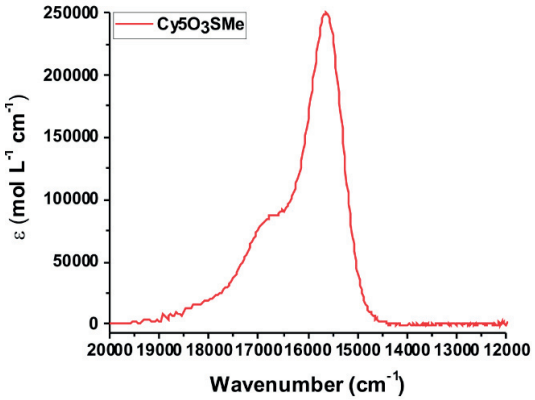

Figure S5. Extinction coefficient ε as function of wavenumber for $Cy5O_3SMe$ solution.

The peak in **Figure S5** was assumed to represent the full band of the lowest energy π-π* transition and was integrated to calculate the oscillator force.

Table S5. Calculated data from recorded UV-Vis spectra. * Onset energy at higher wavelengths obtained from EtOH solution, ** obtained from thin film.

Compound	ε_{max} (L mol^{-1} cm^{-1})	λ_{max} (nm)	λ_{onset} (nm)	$E_{(onset)}$* (eV)	f	$E_{g(opt)}$** (eV)
$Cy5O_3SPh$* (H_2O)	3.56 x10^5	641	672	1.74	1.51	1.68
$Cy5O_3SPhMe$	3.45 x10^5	641	672	1.74	1.63	1.68
$Cy5O_3Naphth$*(H_2O)	3.60 x10^5	641	674	1.74	1.10	1.68
$Cy5O_3SMe$* (H_2O)	3.56 x10^5	641	675	1.74	1.10	1.68

Compound	ε_{max} (L mol^{-1} cm^{-1})	λ_{max} (nm)	λ_{onset} (nm)	$E_{(onset)}$* (eV)	f	$E_{g(opt)}$** (eV)
Cy5TFSI	3.58 x10^5	641	670	1.75	1.59	1.67

2.7.16 Cyclic Voltammetry for Determination of HOMO/LUMO Energy Levels

Cyclic voltammetry (CV) measurements were performed on a PGStat 30 potentiostat (Autolab) using a three cell electrode system (Au working electrode, Pt counter electrode and an Ag/AgCl reference electrode). Two electrolyte solutions of tetrabutylammonium perchlorate and tetrabutylammonium chloride were prepared in DMF each 0.1 mol/L. Each measurement needs 50 ml of tetrabutylammonium perchlorate (25 mL account for the measurement and 25 mL for cleaning) and 10 mL of tetrabutylammonium chloride (4 mL for measurement and 6 mL for cleaning) solutions. Following amounts of the dyes were used (**Table S6**).

Table S6. Weighted quantities of the dyes.

Dye	m (mg)	n (mol)
Cy5O$_3$SPh*(H$_2$O)	10.2	1.82x10^{-5}
Cy5O$_3$SPhMe	5.1	9.19x10^{-6}
Cy5O$_3$SNaphth*(H$_2$O)	10.2	1.68x10^{-5}
Cy5O$_3$SMe*(H$_2$O)	10.1	2.03x10^{-5}
Cy5TFSI	9.6	1.45x10^{-5}

The Ferrocene solution was prepared qualitatively by adding a spatula of ferrocene in 10 mL of electrolyte solution. All potentials were referenced to NHE by adopting a potential of +0.72 V vs. NHE for Fc/Fc+ in DMF.[3] The rotating disk was equilibrated before first measurement for 30 min at 3000 rpm. Then the rotation speed was reduced to 50 rpm and was kept constant for all measurements. Before each measurement step the solution was fumigated with argon for 15 min. The solvent window was determined by running 30 cycles from -1.5 V until 1.5 V with a scanning rate of 2 V/s, subsequently the scanning rate was reduced to 0.1 V/s and the baseline curve was recorded. Then the corresponding dye was added to the solution and the above described measurement procedure was repeated. The negative potential window was adjusted to -0.75 V for all chromophores.

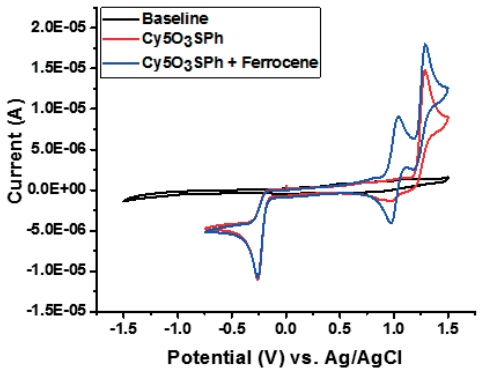

Figure S6. Cyclic voltammetry data of the Cy5O$_3$SPh compound.

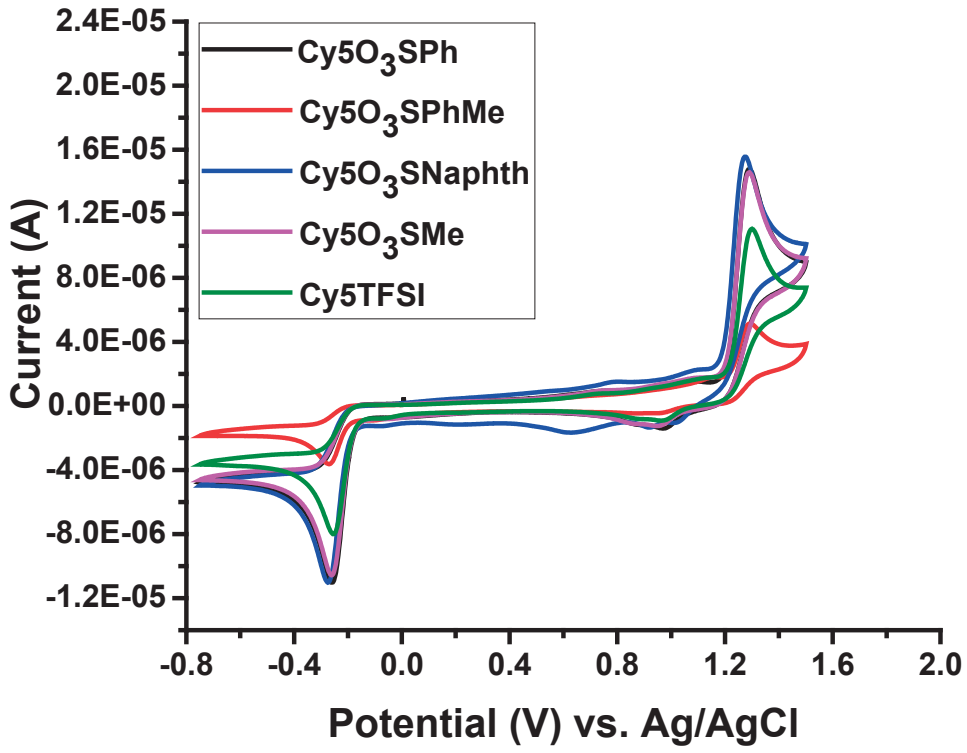

Figure S7. Cyclic voltammograms of all compounds.

The calculations of the $E_{g(el)}$ (HOMO/LUMO gap) are based on the assumption that a positive cathodic current can be referred to a reduction process, while a negative anodic current to an oxidation process. Therefore the oxidation potential corresponds to electron extraction from the HOMO level, while the reduction potential is associated with the electron affinity and indicates the LUMO level. By analysing the recorded spectra graphically it is possible to determine the respective reduction $E_{red(dye)}^{onset}$ or oxidation $E_{ox(dye)}^{onset}$ onset potentials. It is notable that the recorded cyclic voltammograms are showing irreversible processes for all investigated dyes, so that the intersection onset of the corresponding peak has to be chosen as the respective potential. While for the ferrocene which undergoes a reversible process the potential is calculated according to:

$$E_{1/2(Ferrocene)}^{ox} = \frac{E_{pc}^{ox} + E_{pa}^{ox}}{2}$$

$E_{1/2(Ferrocene)}^{ox}$: half-curve potential, E_{pa}^{ox}: anodic peak potential, E_{pc}^{ox} : cathodic peak potential.

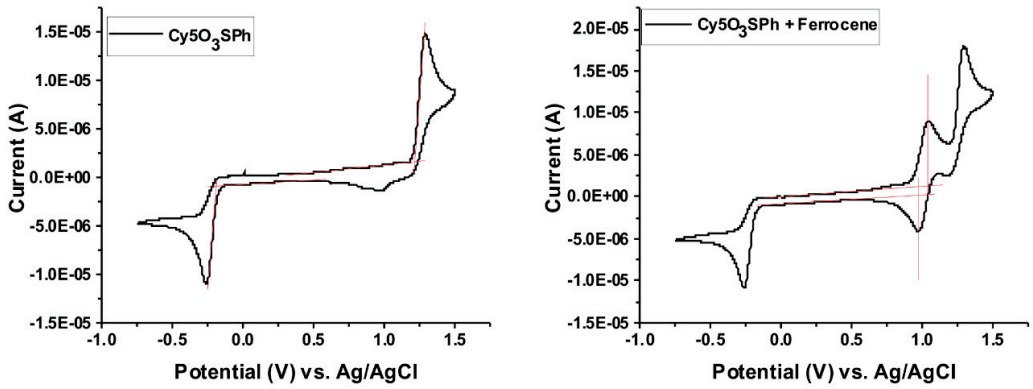

Figure S8. Drawn lines as example for intersection determination in $Cy5O_3SPh$ (left) for the dye and $Cy5O_3SPh$ + Ferrocene (right) for the Ferrocene reference.

The potentials were measured against a Ag/AgCl reference. The used conversion constant for ferrocene in DMF is 0.72 V.[3] The correction value against NHE for ferrocene was calculated as follows:

$$Korr._{Ferrocene}=0.72-E^{ox}_{1/2(Ferrocene)}$$

To calculate the corrected values for the onset potentials against NHE potential the following assumptions were made:

$$E^{onset}_{ox(dye)\ vs.\ NHE} = E^{onset}_{ox(dye)} + Korr._{Ferrocene}$$

$$E^{onset}_{red(dye)\ vs.\ NHE} = E^{onset}_{red(dye)} + Korr._{Ferrocene}$$

The calculation of the HOMO and LUMO was performed by using empirical equations.[4] The used onset potentials were corrected against NHE as described above.

$$E_{HOMO} = -\left(E^{onset}_{ox(dye)\ vs.\ NHE} + 4.5\right)eV$$

$$E_{LUMO} = -\left(E^{onset}_{red(dye)\ vs.\ NHE} + 4.5\right)eV$$

$$E_{g(el)} = E_{HOMO} - E_{LUMO}$$

Table S7. Calculated data from the CV measurement.

Substance	$E^{onset}_{ox(dye)}$ /V	$E^{onset}_{red(dye)}$/V	$E^{0}_{\frac{1}{2}ox(FeCp_2)}$/V	E_{HOMO}/eV	E_{LUMO}/eV	$E_{g(el)}$/eV
$Cy5O_3SPh$	1.20	-0.19	1.01	-5.41	-4.02	1.39
$Cy5O_3SPhMe$	1.20	-0.19	1.00	-5.42	-4.03	1.39
$Cy5O_3SNaphth$	1.18	-0.19	1.00	-5.40	-4.03	1.38
$Cy5O_3SMe$	1.20	-0.18	1.00	-5.42	-4.04	1.38

Substance	$E_{ox(dye)}^{onset}$ /V	$E_{red(dye)}^{onset}$/V	$E_{\frac{1}{2}^{ox(FeCp_2)}}^{0}$/V	E_{HOMO}/eV	E_{LUMO}/eV	$E_{g(el)}$/eV
Cy5TFSI	1.21	-0.17	1.01	-5.42	-4.04	1.38

2.7.17 Carrier Mobility using the CELIV Method

$$\mu = \frac{2d_{dye}\left[d_{dye} + \left(\frac{\varepsilon_{dye}}{\varepsilon_{C_{60}}}\right) \times d_{C_{60}}\right]}{3At^2{}_{max}} \times \frac{1}{\left[1 + 0.36\left(\frac{\Delta j}{j_0}\right)\right]}$$

t_{max} : time at maximum current, d_{dye} : thickness of the dye film, d_{C60} : thickness of the C_{60} layer, $\varepsilon_{dye/C_{60}}$: dielectric constants of the dye and C_{60}, Δj: peak height, j_0 : capacitive current, A : slope of the voltage.

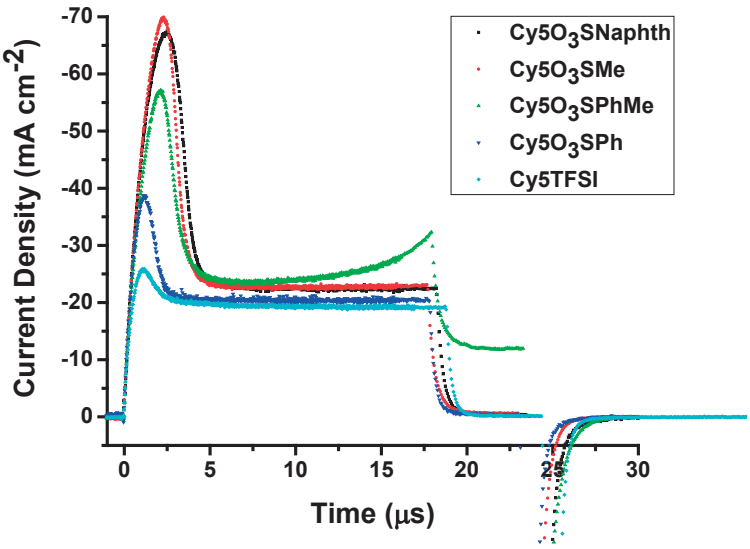

Figure S9. Time dependent current density.

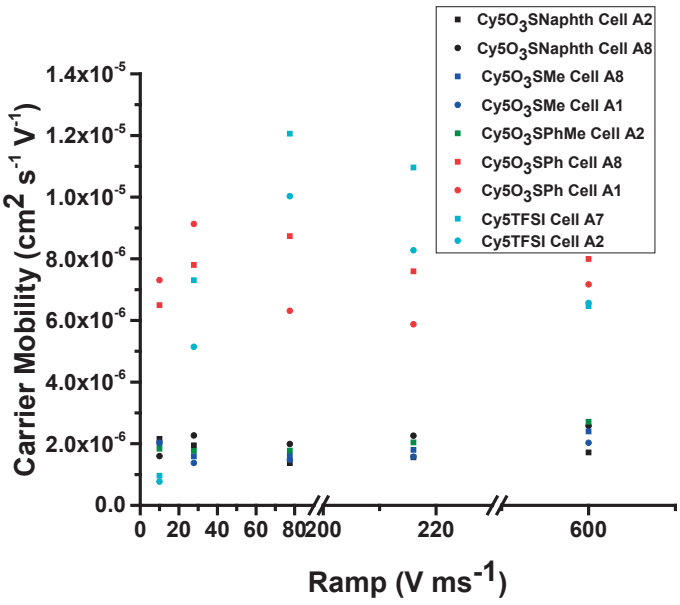

Figure S10. Carrier mobility vs the voltage ramp.

Table S8. Calculated mobilities for the cyanine compounds at a ramp of 216 V/ms. T_{max}/τ_{RC} acts as an indicator for the reliability of the values.

Cyanine	T_{max}/τ_{RC}	μ ($cm^2\ V^{-1}\ s^{-1}$)
$Cy5O_3SPh^*(H_2O)$	6.20	$7.59x10^{-6}$
$Cy5O_3SPhMe$	10.77	$2.04x10^{-6}$
$Cy5O_3SNaphth^*(H_2O)$	17.86	$2.26x10^{-6}$
$Cy5O_3SMe^*(H_2O)$	17.07	$1.79x10^{-6}$
Cy5TFSI	11.09	$1.10x10^{-5}$

2.7.18 Relative Permittivity

$$\varepsilon_r = n^2 - k^2$$

ε_r: relative permittivity (dielectric constant or function), n: real part of the index of refraction, k. imaginary part of the index (extinction coefficient)

The orientational polarization or dipole polarisation appears at low frequencies around 10^4 Hz. The n and k values are dependent on the wavelengths. At higher wavelengths however the slope is very low and at a certain wavelength the k value becomes 0.

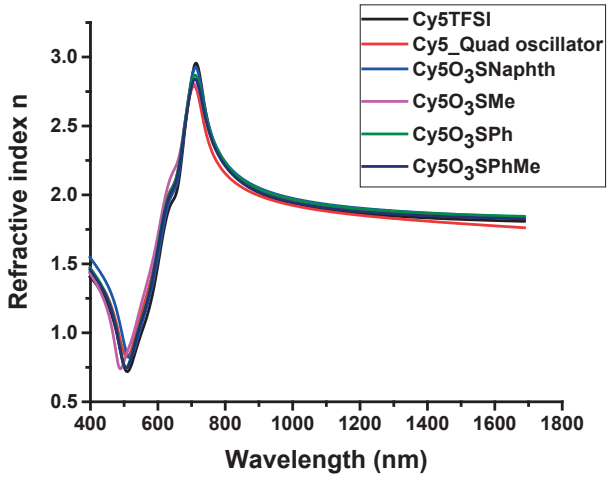

Figure S11. Function of n depending on the wavelength.

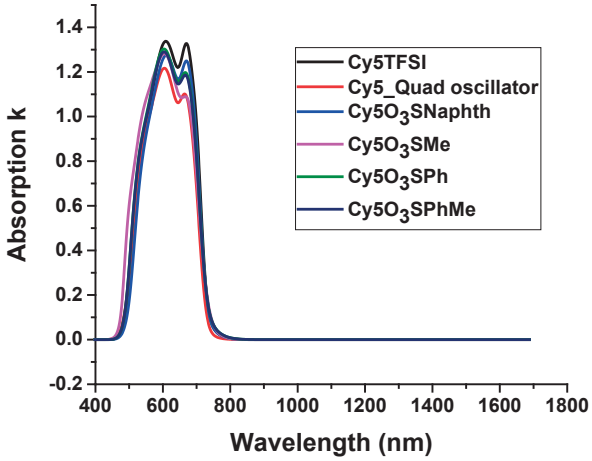

Figure S12 Function of k depending on the wavelength.

Therefore this area was chosen for the calculation of the dielectric constant. The n are given in this table as averaged values over the selected wavelength region.

Table S9. Calculated relative permittivity values for the cyanines.

Cyanine	n	λ/nm	ε_r
Cy5O$_3$SPh*(H$_2$O)	1.88	979-1688	3.53
Cy5O$_3$SPhMe	1.88	975-1688	3.53
Cy5O$_3$SNaphth*(H$_2$O)	1.89	965-1688	3.57
Cy5O$_3$SMe*(H$_2$O)	1.88	1010-1688	3.53
Cy5TFSI	1.86	973-1688	3.46

2.7.19 Crystal Structures

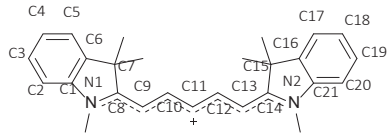

Figure S13. Cyanine atom numbering.

The cyanines were numbered according to the cif file. In the case of Cy5O$_3$SMe and Cy5O$_3$SPh compounds with chromophore/anion triplets in the asymmetric unit the chromophores are numbered with additional b/c letters. This deviation from the cif file is necessary for clarity. The relevant anion atoms were numbered according to the cif file. In the case of Cy5O$_3$SMe and Cy5O$_3$SPh with anion triplets in the asymmetric unit the anions are described with the central S atom as S1/S2/S3.

Table S10. Anion influence on bond lengths (Å) of the chromophore polymethine chain. *Difference between longest and shortest bond length.

Atom	Anion			
	O$_3$SMe	**O$_3$SPh**	**O$_3$SPhMe**	**TFSI**
N1-C1	1.405(6)	1.403(6)	1.408(4)	1.4089(16)
N1b-C1b	1.406(9)	1.415(6)		
N1c-C1c	1.412(6)	1.409(6)		
N1-C8	1.358(8)	1.356(5)	1.357(4)	1.3560(16)
N1b-C8b	1.363(6)	1.364(5)		
N1c-C8c	1.344(9)	1.362(5)		
C8-C9	1.376(7)	1.392(6)	1.377(5)	1.3850(18)
C8b-C9b	1.384(9)	1.388(6)		
C8c-C9c	1.395(7)	1.371(6)		

Atom	Anion			
	O_3SMe	O_3SPh	O_3SPhMe	TFSI
C9-C10	1.398(9)	1.378(6)	1.380(5)	1.3939(19)
C9b-C10b	1.392(7)	1.396(6)		
C9c-C10c	1.363(7)	1.400(6)		
C10-C11	1.378(6)	1.384(6)	1.388(5)	1.3874(19)
C10b-C11b	1.373(9)	1.386(6)		
C10c-C11c	1.389(7)	1.367(6)		
C11-C12	1.396(10)	1.387(6)	1.382(5)	1.3878(19)
C11b-C12b	1.390(7)	1.393(6)		
C11c-C12c	1.372(10)	1.399(6)		
C12-C13	1.391(7)	1.395(6)	1.391(5)	1.3896(19)
C12b-C13b	1.375(9)	1.398(6)		
C12c-C13c	1.395(7)	1.382(6)		
C13-C14	1.379(10)	1.385(6)	1.378(5)	1.3907(19)
C13b-C14b	1.398(7)	1.386(6)		
C13c-C14c	1.379(10)	1.387(6)		
C14-N2	1.361(6)	1.353(5)	1.350(4)	1.3510(17)
C14b-N2b	1.349(8)	1.368(5)		
C14c-N2c	1.360(6)	1.347(5)		
N2-C21	1.414(9)	1.403(6)	1.414(4)	1.4084(17)
N2b-C21b	1.409(6)	1.419(5)		
N2c-C21c	1.416(9)	1.418(5)		
BLA*	2.2	1.7	1.3	0.8
	2.5	1.2		
	3.2	3.3		

Table S11. Anion influence on bending of the chromophore skeleton and indolenium ring conformation. Plane angle measurements between two indolenium rings were performed with Mercury 3.8 (°).

Atoms	**Anions**			
	O_3SMe	**O_3SPh**	**O_3SPhMe**	**TFSI**
Plane angle between two indolenium rings	176.48 (planar)	169.11 (anti)	176.32 (planar)	143.42 (anti)
(N conformation relatively to each other)	168.06 (syn)	169.65 (anti)		
	175.63 (planar)	164.85 (anti)		
C13-C14-C15C-16	179.2(5)	177.4(4)	178.7(4)	175.16(14)
C13b-C14b-C15b-C16b	176.1(5)	177.4(4)		
C13c-C14c-C15c-C16c	176.2(6)	179.4(4)		
C6-C7-C8-C9	179.8(5)	176.5(4)	177.3(3)	171.90(14)
C6b-C7b-C8b-C9b	177.8(5)	179.5(4)		
C6c-C7c-C8c-C9c	178.9(6)	172.2(4)		

Table S12. Anion influence on cyanine chromophore geometry (°).

Atoms	**torsion angles**			
	O_3SMe	O_3SPh	O_3SPhMe	TFSI
C9-C10-C11-C12	179.5(5)	179.9(4)	180.0(3)	174.39(14)
C9b-C10b-C11b-C12b	178.6(5)	179.8(4)		
C9c-C10c-C11c-C12c	179.9(7)	176.0(4)		
C8-N1-C1-C2	179.6(5)	177.4(4)	179.6(4)	179.6(4)
C8b-N1b-C1b-C2b	179.4(5)	179.7(4)		
C8c-N1c-C1c-C2c	179.0(6)	172.4(4)		
C8-C7-C6-C5	177.5(5)	177.4(4)	178.3(4)	174.74(14)
C8b-C7b-C6b-C5b	178.3(5)	179.7(4)		
C8c-C7c-C6c-C5c	179.2(7)	174.7(4)		
C14-N2-C21-C20	179.5(5)	178.6(5)	179.7(4)	178.78(14)
C14b-N2b-C21b-C20b	176.4(5)	179.8(4)		
C14c-N2c-C21c-C20c	178.7(6)	178.7(5)		
C14-C15-C16-C17	179.9(5)	178.5(4)	179.7(4)	177.06(14)
C14b-C15b-C16b-C17b	178.2(6)	179.6(4)		

Atoms	torsion angles			
	O_3SMe	O_3SPh	O_3SPhMe	TFSI
C14c-C15c-C16c-C17c	175.5(7)	179.2(5)		

Table S13. Anion charge distribution (Å).

Atoms	Anion			
	O_3SMe	O_3SPh	O_3SPhMe	TFSI
S1-O1	1.436(4)	1.441(10)	1.451(2)	1.4282(11)
S1-O2	1.462(3)	1.423(6)	1.454(3)	1.4246(11)
S1-O3	1.456(3)	1.519(8)	1.457(2)	
S2-O4	1.382(12)	1.448(4)		1.4172(12)
S2-O5	1.463(10)	1.447(4)		1.4259(13)
S2-O6	1.440(11)	1.432(4)		
S3-O7	1.425(14)	1.470(8)		N3-S1
S3-O8	1.552(10)	1.538(12)		1.5616(14)
S3-O9	1.502(15)	1.451(11)		N3-S2
				1.5760(14)

Table S14. Shortest anion-chromophore coordination distance (Å). The nitrogen atoms of the chromophore are acting as anchor groups for the measurement. Measurements were performed with Mercury 3.8.

Atom	Anion			
	O_3SMe	O_3SPh	O_3SPhMe	TFSI
N1-O	4.108	4.321	4.408	4.492
N1b-O	4.626	4.968		
N1c-O	4.254	4.342		
N2-O	4.244	4.619	4.129	4.424
N2b-O	4.266	4.807		
N2c-O	4.092	4.200		

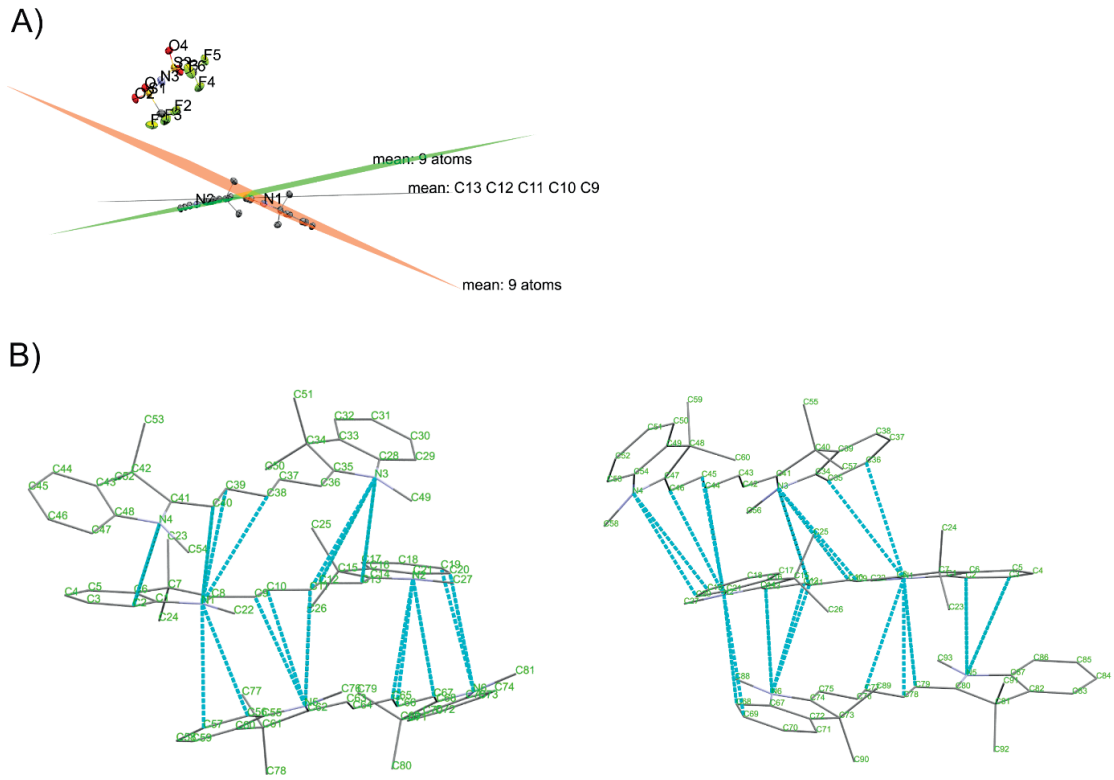

Figure S14. A) Chromophore bending angle measurement example. B) Observed π-interaction contacts and tilting within the chromophore triplets. Left: Cy5O$_3$SMe, Right: Cy5O$_3$SPh.

2.7.20 Organic Photovoltaic Device Fabrication

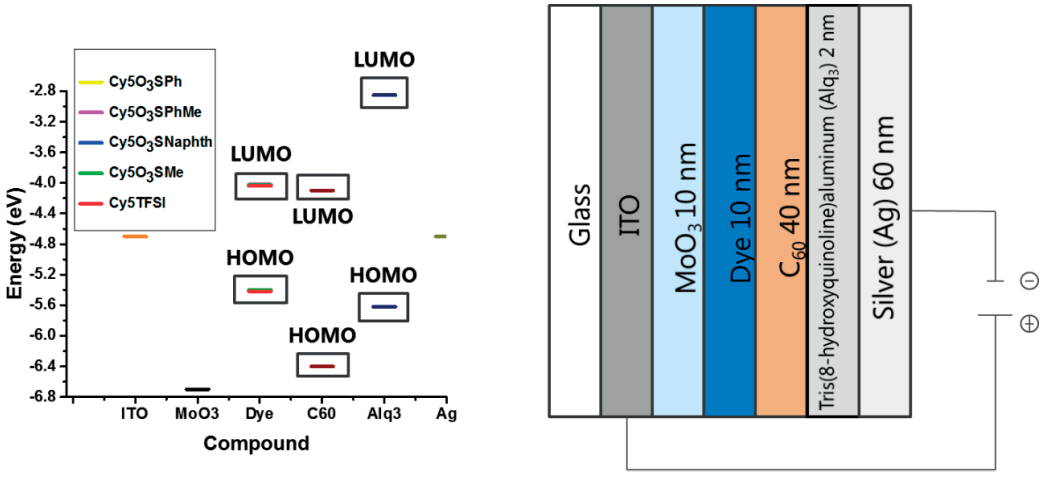

Figure S15. Band energy situation in fabricated cells against vacuum level and architecture of the manufactured cells.

The devices were made out of seven layers: glass, indium tin oxide, molybdenum oxide (10 nm) as hole transport layer, dye layer (10 nm) as light absorbing active layer, C_{60} (40 nm) as electron acceptor, aluminumquinoline (2 nm) as diffusion blocking layer and silver

(60 nm) as bottom electrode. The metals and C_{60} were deposited by thermal evaporation while the dye layer was spincast from solution.

2.7.21 Statistics of the Cy5TFSI Cell

- Detailed insight reveals a broad deviation in all cell parameters
- Indication that the active layer morphology is not optimal

Film surface is very smooth, which indicates that the problem lies inside the volume of the active layer

Table S15. Detailed statistics of the best performing Cy5TFSI. Only working cells were analyzed.

	N total	Mean	Standard Deviation	Minimum	Median	Maximum
Voc (V)	33	0.66	0.09	0.27	0.70	0.72
Jsc (mA cm^{-2})	33	5.82	0.50	5.00	5.79	7.37
Eff (%)	33	2.00	0.54	0.49	2.03	3.02
FF (%)	33	50.91	7.44	32.04	53.35	59.19

2.7.22 Optimization Trials of the Cy5TFSI Cell

2.7.23 Vacuum Treatment of the Active Layer

The results indicated that residues of TFP could cause broad deviations in cell performance data. Therefore after spincoating of the active layer the device was stored for 16 h at 1 x 10^{-6} mbar before further processing. All the average values improve after this additional vacuum treatment this indicates that TFP remains in the thin film volume. For further studies TFP should be avoided, even if it forms a very smooth film surface.

Table S16. Detailed statistics obtained after vacuum treatment of the active layer.

	N total	Mean	Standard Deviation	Minimum	Median	Maximum
Voc (V)	15	0.63	0.05	0.56	0.64	0.69
Jsc (mA cm^{-2})	15	5.87	0.42	5.43	5.72	6.83
Eff (%)	15	2.13	0.39	1.53	1.97	2.86
FF (%)	15	57.05	3.92	49.24	56.05	62.50

2.7.24 Thermal Annealing Followed After Vacuum Treatment

Remaining TFP traces could change the 3D morphology of the active layer by accelerating crystallization. Therefore thermal annealing was performed with the aim to evaporate residual TFP. Devices were heated at different temperatures for 1 h.

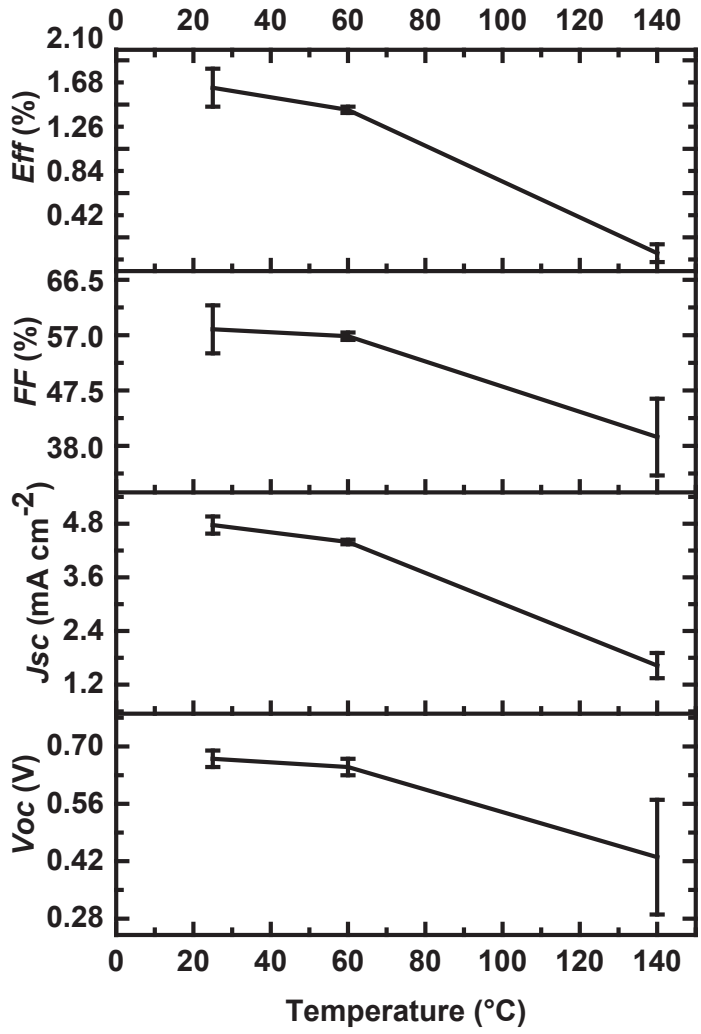

Figure S16. OPV parameters plotted against dependence of temperature. 8 Cells were investigated for each temperature step.

Unfortunately the additional thermal treatment worsens all of the OPV parameters. Optimal conditions are thus reached already after vacuum treatment.

2.7.25 Additive Effect

To observe if an antisolvent could prevent the TFP effect different concentrations of diiodooctane (DIO) were added to the Cy5TFSI solution before spincasting.

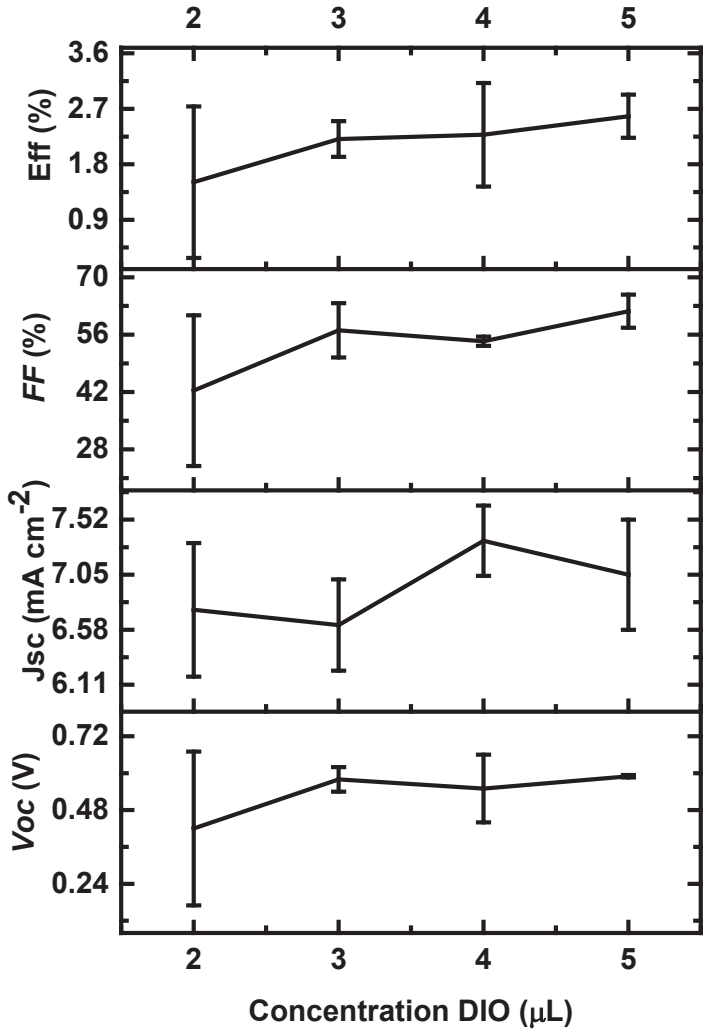

Figure S17. DIO concentration effect on OPV device parameters.

A large gap between working and short circuited cells was obtained. Only 4 of 8 cells from each device were not short circuited. A slight improvement of the fill factor and performance occurs, while the open circuit voltage and the short circuit current density remains the same. The short circuit current is increased compared to the values obtained after vacuum treatment. All other values do not reach the averages obtained after vacuum treatment. Therefore it can be concluded that DIO does not have a significant favorable effect on device parameters.

2.7.26 Active Layer Thickness Variation

A thicker active layer is capable of absorbing more light and generating more free charges. Most of the organic materials have a very low exciton diffusion length of 10 nm, so that thick light absorbing layers result in charge recombination. To find out if this exciton diffusion length limitation also applies to the synthesized materials four devices with different active layer thickness were prepared.

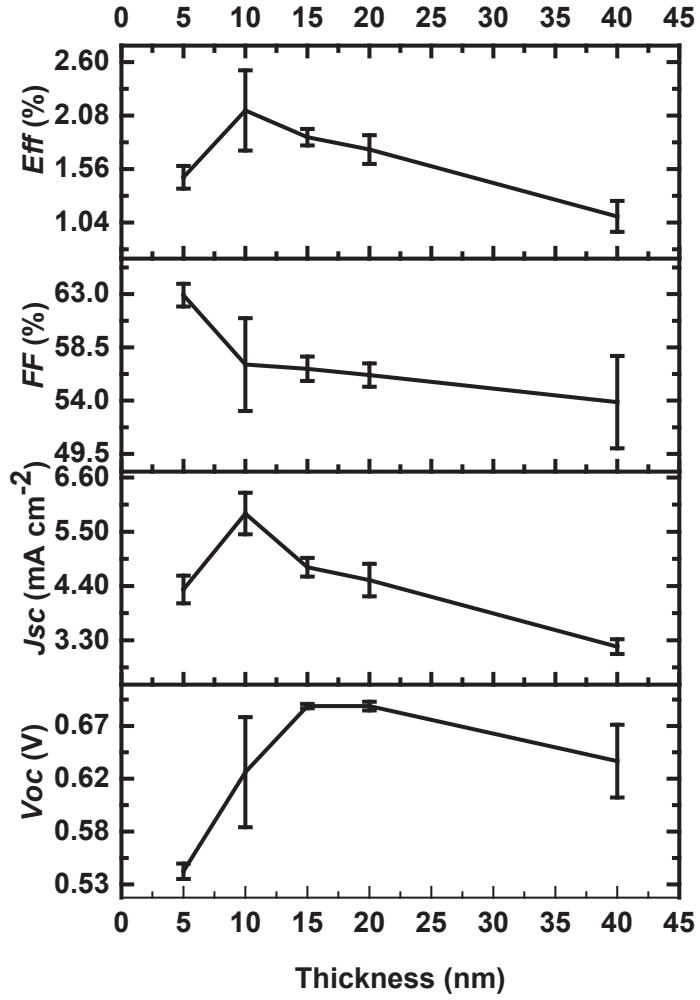

Figure S18. OPV parameters dependence on active layer thickness based on data from 8 cells for each thickness.

Except for the fill factor which reaches its maximum for an active layer thickness of 5 nm, all the OPV parameters reach their maxima at 10 nm active layer thickness. Therefore it can be assumed that the used compounds have an exciton diffusion length of 10 nm. The thickness dependent trends obtained in external quantum efficiency (EQE) spectra support this assumption.

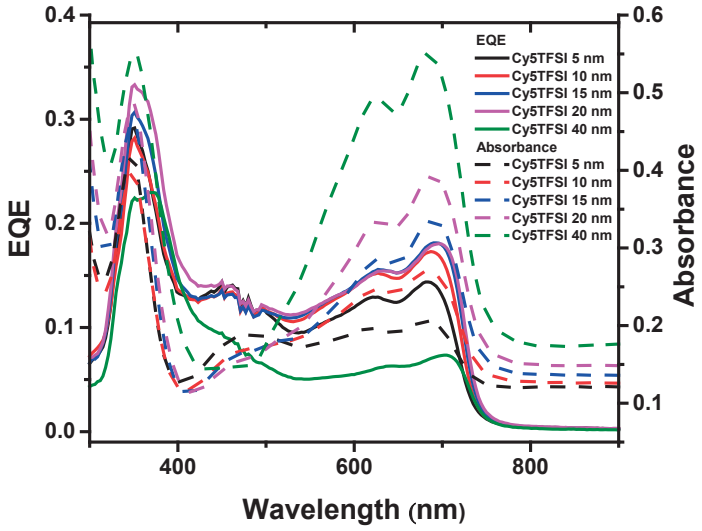

Figure S19. EQE and absorbance of aged devices (storage of several weeks in a glovebox) as function of active layer thickness.

2.7.27 Aging behavior

Unfortunately, devices all show a fast degradation within a few hours in the dark. Interestingly this manifests in the relative contributions of the active components to the EQE spectrum. We exemplify this behavior in bilayer solar cells using $Cy5O_3SPh$ as electron donor and C_{60} as acceptor. **Figure S20** clearly shows that the cyanine contribution to the EQE decreases more significantly than the C_{60} after storing the device for 16 h in a glove box. Correspondingly, the short circuit current density $J_{sc} = \int EQE(\lambda)*\Phi_{AM1.5}(\lambda)*e\, d\lambda$ obtained by integrating over $EQE(\lambda)$, the photon flux $\Phi_{AM1.5}(\lambda)$ of the AM1.5 solar spectrum and multiplying by the elementary charge e yields values of 4.30 mA cm^{-2} and 2.94 mA cm^{-2} for fresh and aged devices, respectively.

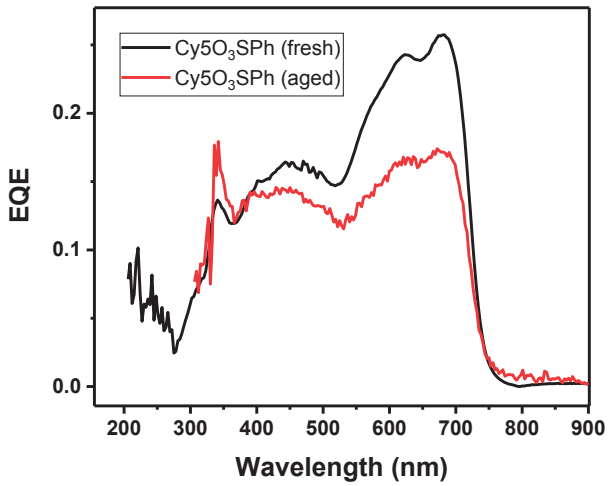

Figure S20. EQE of devices using $Cy5O_3SPh$ as active layer. Fresh devices (black) were measured right after fabrication, while aged devices (red) were stored in a glovebox for 16h in the glove box.

2.7.28 DFT Calculations of Cyanine Dyes Based on Single Crystal Data

We have used Density Functional Theory to obtain an insight into the electronic structure and charge distribution for the different anion-chromophore pairs of Cy5O$_3$SPh, Cy5TFSI and Cy5O$_3$SPhMe and we have considered two different structures. Firstly, we have performed calculations on each inequivalent pair in the asymmetric unit cell, as obtained from the crystallographic data. Secondly, we have further energy-minimised each molecule within the unit cell at the B3LYP/6-31G* level. More specifically, all molecules within the unit cell were brought to their local minimum through an optimization within their local environment using the QM/MM scheme implemented in the NWChem software. All atoms surrounding the molecule of reference, within a radius of 12 Angstrom from the atoms in the QM part, were kept fixed, creating a neutral pocket in which the molecule was then relaxed using B3LYP/6-31G*. Since more than one molecule is present in the unit cell, this procedure was performed in a cyclic fashion, i.e. one molecule was relaxed each time in a self-consistent way until convergence was reached. Following the QM/MM optimization we computed the electronic structure for each anion-chromophore pair.

DFT calculations were performed using the Coulomb attenuated CAM-B3LYP exchange-correlation functional and a split valence double zeta polarised 6-31+G* basis set. Singlet vertical excitation energies have been computed from linear response time dependent density functional theory (TD-DFT). All calculations were performed with the NWChem program, version 6.5[5] and for the visualization of the orbitals and potential maps we used the MView software.[6]

Figure S21 displays the Kohn-Sham HOMO and LUMO orbital plots for the different anion-chromophore pairs. We find that for all compounds the HOMO and the LUMO frontier orbitals are localized on the cyanine chromophore. In particular, the LUMO displays a stronger localization over the polymethine chain compared with the HOMO and the delocalization pattern of both levels is not affected by the type of the anion. This is consistent with the cyclic voltammetry measurements suggesting that the anion does not have a strong influence on the HOMO and LUMO energy levels when considering solution or gas-phase conditions.

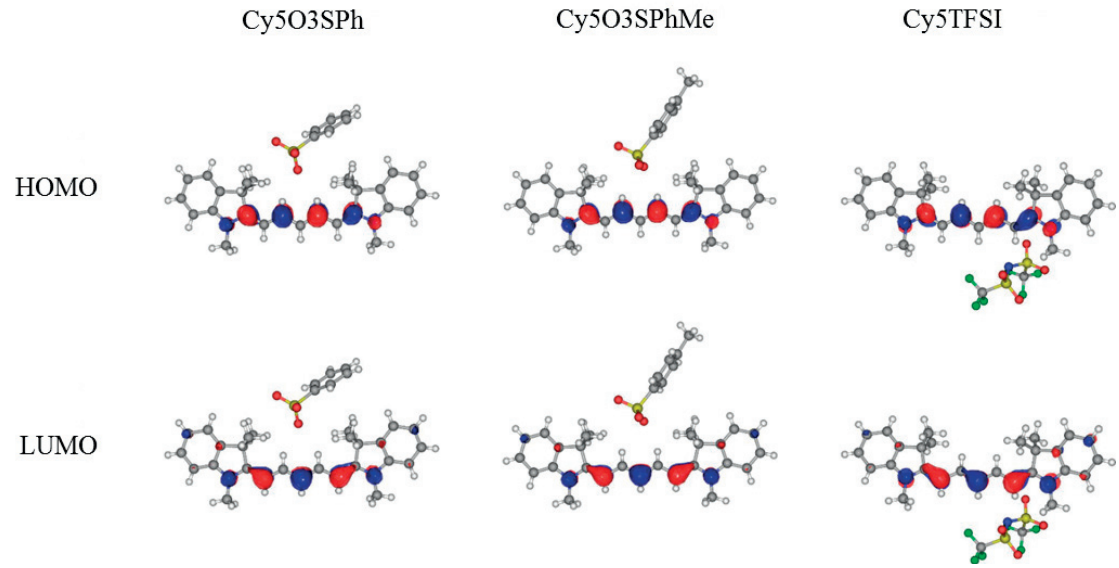

Figure S21. Kohn-Sham HOMO and LUMO frontier molecular orbital distributions of the anion-chromophore pairs calculated at the CAM-B3LYP/6-31+G* level.

The molecular electrostatic potential maps depicted in **Figure S22** can provide information about the charge distribution of each anion-chromophore pair. We observe that the negative charge of the sulfonate anions is mainly localized on the oxygen atoms, while the bistriflylimide anion appears as a large diffuse electron cloud. The general trend is that all chromophores form an electrostatic interaction pocket in the gap between the polymethine chain and the two indolium rings. The sulfonate based anions interact electrostatically with the chromophore within this pocket. This suggests potential nucleophilic attack regions within the chromophore and represents a weak point of cyanine dye salts. Due to the crystallographic environment of the first chromophore-anion pair in Cy5O3SPh the anion does not show strong interactions with the chromophore. A weaker electrostatic interaction with the chromophore is also observed for the bistriflylimide anion.

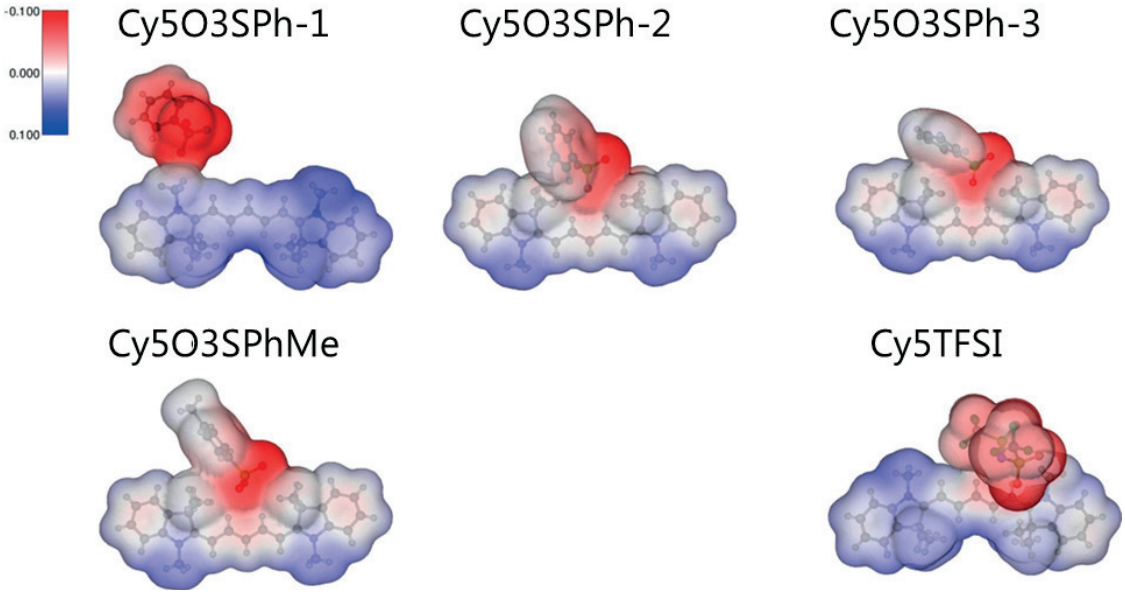

Figure S22. Molecular electrostatic potential map of the anion-chromophore pairs calculated at the CAM-B3LYP/6-31+G* level.

2.7.29 Literature Supporting Information

[1] Sheldrick, G. M. (2008). Acta Cryst. A64, 112-122.
[2] Spek, A. L. (2003). J.Appl.Cryst. 36, 7-13.
[3] C. G. Zoski, *Handbook of electrochemistry*; Elsevier, 2007.
[4] J. L. Bredas, R. Silbey, D. S. Boudreaux, R. R. Chance, *J. Am. Chem. Soc.* **1983**, *105*, 6555.
[5] M. Valiev, E. J. Bylaska, N. Govind, K. Kowalski, T. P. Straatsma, H. J. J. Van Dam, D. Wang, J. Nieplocha, E. Apra, T. L. Windus, W. A. de Jong, Comput. Phys. Commun. 2010, 181, 1477
[6] L. Viani, MView: A Tool for Visualization and Analysis of Molecular Properties, www.mview-Tools.com

2.8 Acknowledgements

We thank Dr. Matthias Nagel (Empa) for suggestions and Dr. Mohammed Makha (Empa) for his help with the thermal evaporation techniques. The use of the Scanning Probe Microscopy User Laboratory at Empa is gratefully acknowledged. We thank the Swiss National Science Foundation for financial support under grant number 160116. This project has also received funding from the Universidad Carlos III de Madrid, the European Union's Seventh Framework Program for research, technological development and demonstration under grant agreement nº 600371, el Ministerio de Economía, Industria y Competitividad (COFUND2014-51509), el Ministerio de Educación, cultura y Deporte (CEI-15-17) and Banco Santander.

2.9 References

[1] V. Z. Shirinian, A. A. Shimkin, In *Heterocyclic Polymethine Dyes*; Springer Berlin Heidelberg: Berlin, Heidelberg, 2008; pp. 75–105.
[2] A. Ajayaghosh, *Acc. Chem. Res.* **2005**, *38*, 449.
[3] J. Roncali, P. Leriche, P. Blanchard, *Adv. Mater.* **2014**, *26*, 3821.
[4] J. L. Bricks, A. D. Kachkovskii, Y. L. Slominskii, A. O. Gerasov, S. V Popov, *Dye. Pigment.* **2015**, *121*, 238.
[5] C. H. G. Williams, *Trans. Roy. Soc. Edinburgh* **1856**, 377.
[6] C. Shi, J. B. Wu, D. Pan, *J. Biomed. Opt.* **2016**, *21*, 50901.

[7] W. Sun, S. Guo, C. Hu, J. Fan, X. Peng, *Chem. Rev.* **2016**, *116*, 7768.
[8] U. Lawrentz, W. Grahn, K. Lukaszuk, C. Klein, R. Wortmann, A. Feldner, D. Scherer, *Chem. - A Eur. J.* **2002**, *8*, 1573.
[9] R. V. Markov, P. A. Chubakov, A. I. Plekhanov, Z. M. Ivanova, N. A. Orlova, T. N. Gerasimova, V. V. Shelkovnikov, J. Knoester, *Nonlinear Opt.* **2000**, *25*, 365.
[10] H. Tian, F. Meng, In *Functional Dyes*; 2006; pp. 47–84.
[11] J. Tan, D. Ma, X. Sun, S. Feng, C. Zhang, *Dalton Trans.* **2013**, *42*, 4337.
[12] K. Y.-J. Liao; Wen-Yih, Huang; Chien-Liang, Huang; Der-Ray, Chiang; Don-You, Hu; Andrew Teh, Lee; Hong-Ji, Ye; Shi-jae, Preparation of cyanine dye for high density optical recording disk, US patent US5958087 A, **1999**.
[13] M. Young, J. Suddard-Bangsund, T. J. Patrick, N. Pajares, C. J. Traverse, M. C. Barr, S. Y. Lunt, R. R. Lunt, *Adv. Opt. Mater.* **2016**, *4*, 1028.
[14] H. Zhang, G. Wicht, C. Gretener, M. Nagel, F. Nüesch, Y. Romanyuk, J.-N. Tisserant, R. Hany, *Sol. Energy Mater. Sol. Cells* **2013**, *118*, 157.
[15] O. Malinkiewicz, T. Grancha, A. Molina-Ontoria, A. Soriano, H. Brine, H. J. Bolink, *Adv. Energy Mater.* **2013**, *3*, 472.
[16] A. C. Véron, H. Zhang, A. Linden, F. Nüesch, J. Heier, R. Hany, T. Geiger, *Org. Lett.* **2014**, *16*, 1044.
[17] G. Wicht, S. Bücheler, M. Dietrich, T. Jäger, F. Nüesch, T. Offermans, J. N. Tisserant, L. Wang, H. Zhang, R. Hany, *Sol. Energy Mater. Sol. Cells* **2013**, *117*, 585.
[18] M. Bates, R. R. Lunt, *Sustain. Energy Fuels* **2017**, *0*, 1.
[19] A. Mishra, R. K. Behera, P. K. Behera, B. K. Mishra, G. B. Behera, *Chem. Rev.* **2000**, *100*, 1973.
[20] M. Panigrahi, S. Dash, S. Patel, B. K. Mishra, *Tetrahedron* **2012**, *68*, 781.
[21] Zhifei Dai, Bixian Peng, *Dye. Pigment.* **1998**, *36*, 169.
[22] R. Nanjunda, E. A. Owens, L. Mickelson, S. Alyabyev, N. Kilpatrick, S. Wang, M. Henary, W. D. Wilson, *Bioorg. Med. Chem.* **2012**, *20*, 7002.
[23] E. A. Owens, N. Bruschi, J. G. Tawney, M. Henary, *Dye. Pigment.* **2015**, *113*, 27.
[24] K. Funabiki, K. Yagi, M. Nomoto, Y. Kubota, M. Matsui, *J. Fluor. Chem.* **2015**, *174*, 132.
[25] P. E. Kolic, N. Siraj, M. Cong, B. P. Regmi, X. Luan, Y. Wang, I. M. Warner, *RSC Adv.* **2016**, *6*, 95273.
[26] A. N. Jordan, S. Das, N. Siraj, S. L. de Rooy, M. Li, B. El-Zahab, L. Chandler, G. a. Baker, I. M. Warner, *Nanoscale* **2012**, *4*, 5031.
[27] M. Matsui, S. Ando, M. Fukushima, T. Shibata, Y. Kubota, K. Funabiki, *Tetrahedron* **2015**, *71*, 3528.
[28] S. Dähne, R. Radeglia, *Tetrahedron* **1971**, *27*, 3673.
[29] L. M. Tolbert, X. Zhao, .
[30] C. Kuhn, *Synth. Met.* **1991**, *43*, 3681.
[31] P.-A. Bouit, C. Aronica, L. Toupet, B. Le Guennic, C. Andraud, O. Maury, *J. Am. Chem. Soc.* **2010**, *132*, 4328.
[32] O. D. Kachkovski, O. I. Tolmachov, Y. L. Slominskii, M. O. Kudinova, N. O. Derevyanko, O. O. Zhukova, *Dye. Pigment.* **2005**, *64*, 207.
[33] R. L. Gieseking, M. K. Ravva, V. Coropceanu, J.-L. Brédas, *J. Phys. Chem. C* **2016**, *120*, 9975.
[34] X.-F. Zhang, J.-L. Zhao, W.-B. Bi, D.-D. Zhang, Z.-Y. Yang, L.-Y. Wang, *J. Chinese Chem. Soc.* **2013**, *60*, 503.
[35] Z. Dai, B. Peng, X. Chen, *Dye. Pigment.* **1999**, *40*, 219.
[36] H. Jia, Y. Lv, S. Wang, D. Sun, L. Wang, *RSC Adv.* **2015**, *5*, 4681.
[37] S. Haslinger, G. Laus, V. Kahlenberg, K. Wurst, T. Bechtold, S. Vergeiner, H. Schottenberger, *Crystals* **2016**, *6*, 40.
[38] J. Suddard-Bangsund, C. J. Traverse, M. Young, T. J. Patrick, Y. Zhao, R. R. Lunt, *Adv. Energy Mater.* **2016**, *6*, 1501659.
[39] D. S. Pisoni, L. Todeschini, A. C. A. Borges, C. L. Petzhold, F. S. Rodembusch, L. F. Campo, *J. Org. Chem.* **2014**, *79*, 5511.
[40] W. West, S. Pearce, *J. Phys. Chem.* **1965**, *566*, 1894.
[41] S. Jenatsch, R. Hany, A. C. Véron, M. Neukom, S. Züfle, A. Borgschulte, B. Ruhstaller, F. Nüesch, *J. Phys. Chem. C* **2014**, *118*, 17036.

Chapter 3 Superweak Coordinating Anion as Superstrong Enhancer of Cyanine Organic Semiconductor Properties

Donatas Gesevičius,[a,f] Antonia Neels[b], Sergii Yakunin,[c,d] Erwin Hack,[e] Maksym V. Kovalenko,[c,d] Frank Nüesch[a,g] and Jakob Heier[a]

a. Laboratory for Functional Polymers, Swiss Federal Laboratories for Materials Science and Technology, Empa, Überlandstrasse 129, Dübendorf, Switzerland.
b. Center for X-ray Analytics, Swiss Federal Laboratories for Materials Science and Technology, Empa, Überlandstrasse 129, Dübendorf, Switzerland.
c. Laboratory for thin films and photovoltaics, Swiss Federal Laboratories for Materials Science and Technology, Empa, Überlandstrasse 129, Dübendorf, CH-8600, Switzerland.
d. Department of Chemistry and Applied Biosciences, Swiss Federal Institute of Technology Zurich, Vladimir Prelog Weg 1, Zurich,CH-8093, Switzerland.
e. Laboratory for Transport at Nanoscale Interfaces, Swiss Federal Laboratories for Materials Science and Technology, Empa, Überlandstrasse 129, CH-8600 Dübendorf, Switzerland.
f. Institute of Chemical Sciences and Engineering, ISIC, Ecole Polytechnique Fédérale de Lausanne, EPFL, Station 6, CH-1015 Lausanne, Switzerland.
g. Institut des Matériaux, Ecole Polytechnique Fédérale de Lausanne, EPFL, Station 6, CH-1015 Lausanne, Switzerland. E-mail: jakob.heier@empa.ch

3.1 Declaration of Contribution

This chapter is an exact copy of an article to be published in ChemPhysChem, which was accepted for publication by the 31st of October 2018. Unless otherwise stated Donatas Gesevičius was responsible for all the experiments and practical work. In all cases, the idea development, interpretation of results and the writing of the manuscript was performed by Donatas Gesevičius. Antonia Neels was responsible for X-Ray analysis. Sergii Yakunin and Maksym Kovalenko where responsible for the photoluminescence measurements. Erwin Hack was supporting the ellipsometry raw data analysis. Frank Nüesch and Jakob Heier where responsible for proofreading, submitting and moderating scientific discussions.

DOI: 10.1002/cphc.201800863R1

3.2 Keywords

Superweak coordinating anions, cyanine dyes, fluorescence, lattice energy, organic photovoltaics.

3.3 Abstract

The tetrakis(nonafluoro-*tert*-butoxy)aluminate superweak coordinating anion was employed to introduce pseudo gas-phase conditions to the 2-[5-(1,3-dihydro-1,3,3-trimethyl-2H-indol-2-ylidene)-1,3-pentadien-1-yl]-1,3,3-trimethyl-3H-indolium chromophore. The resulting formation of a photoactive organic-inorganic hybrid salt has led to a highly stabilized excited state of the organic chromophore mainly due to the minimized lattice energy and Coulomb interactions. These highly beneficial features caused by the well dispersed negative charge of the anion have led to an enhanced neat spin-casted film fluorescence intensity, prolonged fluorescence lifetime, smooth thin film surfaces and a record power photovoltaic efficiency of 3.8% when compared to organic salts of this particular chromophore containing anions with localised negative charge. Clear evidence is given that a superweak coordinating anion is an emerging key parameter in cyanine dye photochemistry. This approach can be seen as a general guideline to prepare highly efficient ionic dyes for organic semiconductor applications.

3.4 Introduction

The concept of weakly coordinating anions (WCA's) was introduced in the seventies.[1] It was shown that in condensed matter the cation-anion interactions can never reach a non-coordinative state but rather can be minimized, which is commonly called "pseudo gas-phase condition".[2,3] To achieve this state, weakly coordinating anions underwent decades of development. The challenge is rooted into the creation of an anion with a low overall negative charge and its simultaneous delocalisation over the whole molecule. The central core of such anions contains usually strong *Lewis* acids (B, Al, Ga, Sb, As) which are shielded with large non-polarizable moieties to prevent degradation and eliminate possible basicity and nucleophilic sites.[4] Most commonly, bulky perfluorinated moieties are used with the ability to form additional stabilising fluorine contacts to the *Lewis* acidic centre.[5] The most common classes of WCA's are the perfluorinated metalates, perfluorinated tetraarylborates, carboranes, alkoxy/aryloxy metalates and teflates.[3,4,6–11] Concerning practical applications of such anions in organic semiconductor research, stability against moisture, oxygen and redox reactions as well as high temperatures is crucial. Due to the large size of up to several nanometres, weakly coordinating anions tend to degrade into smaller coordinating species.[12–15] Perfluoroborates exhibit often a high redox tendency which has to be avoided in organic photovoltaic (OPV) applications.[16,17] A more prominent example is the C_{60}^- anion whose application in OPV research is ruled out because of its reduction potential below 0 V vs NHE.[18–20] Considering all mentioned factors, only the perfluorinated alkoxy aluminates, tetrakis(nonafluoro-*tert*-butoxy)aluminate in particular, unifies the desired properties, making it the least coordinating anion that can be used for OPV applications.[21]

Organic semiconductors as such were discovered over 60 years ago and underwent decades of intense research.[22,23] To date, organic salts, especially cyanine dyes represent only a small group among all small molecule organic semiconductors.[24] Comparing anionic and cationic chromophores to neutral chromophores, cyanine dyes exhibit optical properties that outperform their neutral counterparts in many aspects. This is mainly caused by the chromophore geometry, in which an odd numbered polymethine chain is connecting an auxochrome group as well as an antiauxochrome moiety on the other end.[25,26] Considering the structural properties of cyanine dyes it becomes clear why the counterion has such a tremendous influence on the chromophore's electronic, conformational and optical properties; especially in neat spin-casted films and organic electronic devices.[24,27–33] The single positive charge of the chromophore in its ground state electron configuration is compensated by the anion. On the contrary, exciting a cyanine and transferring an electron to an acceptor in an OPV device creates formally a doubly positively charged molecule for a short period, a highly unfavourable state for the cyanine chromophore when considering the standard ionisation potential approach for molecules.[34,35] Additionally, typical exciton radii in organic materials are smaller than the unit cell volume.[36] Therefore in conventional organic semiconductors[36,37] and especially salts,[31] where strong Coulomb forces are dominant, excitons are trapped in low energy excited states and are prone to non-radiative recombination. On the contrary, free charge carriers at donor-acceptor heterojunctions can only be generated, when electrons escape the Coulomb field, which was identified as the rate-limiting process in organic-salt-based photovoltaics.[38] Considering the simple Coulomb equation for point charges shows that the Coulomb field is significantly dependent on the distance between cations and anions.[39] Therefore, anions that lower the lattice energy and Coulomb interactions by spreading their charge over a large volume stabilize the excited state and reduce the binding energy of charge transfer states. It had also been shown that small point charges, such as anions, can introduce symmetry breaking within the polymethine chain and lead to a dipolar state.[40–43]

This work combines the two presented concepts, which leads to the creation of an organic/inorganic hybrid salt between a cyanine dye and a superweak coordinating anion unifying desirable properties from both classes of materials. Effects of the superweak coordinating anion on lattice energy, fluorescence intensity and fluorescence lifetime of spin-casted neat films as well as OPV device parameters are presented. This study allows the direct comparison among salts of 2-[5-(1,3-dihydro-1,3,3-trimethyl-2H-indol-2-ylidene)-1,3-pentadien-1-yl]-1,3,3-trimethyl-3H-indolium chromophore between point like charge sulfonate anions with different organic moieties, the bistriflylimide with its negative charge delocalised over seven atoms and tetrakis(nonafluoro-*tert*-butoxy)aluminate introduced in this study with its negative charge spread over more than 36 atoms. Indeed, the superweak coordinating anion boosted the fluorescence intensity and quantum yield of neat spin-casted films as well as open circuit voltage, external quantum efficiency and performance of organic photovoltaic devices, as will be presented in further sections of this work. Most interestingly, linear correlations can be found between the lattice energy of the cyanine salts and fluorescence intensity as well as organic photovoltaic parameters allowing future predictions of these.

3.5 Results and Discussion

3.5.1 Anion Exchange and Solid State Features

The 2-[5-(1,3-dihydro-1,3,3-trimethyl-2H-indol-2-ylidene)-1,3-pentadien-1-yl]-1,3,3-trimethyl-3H-indolium tetrakis(nonafluoro-*tert*-butoxy)aluminate (Cy5[Al(pftb)$_4$]) (**Figure 3:1A**) was obtained via a salt metathesis reaction in chlorobenzene (see Supporting information for the anion-exchange procedure).

Slow cooling of a saturated chlorobenzene solution yielded single crystals suitable for X-ray analysis. The Cy5[Al(pftb)$_4$] crystallizes in a monoclinic crystal system, space group $P2_1/c$, with one chromophore anion pair per asymmetric unit, additionally containing two intercalated and disordered chlorobenzene molecules. Within two unit cells the packing of Cy5[Al(pftb)$_4$] shows well-separated chromophores due to the superweak coordinating anion, which prevents any close intermolecular interactions (**Figure 3:1B**).

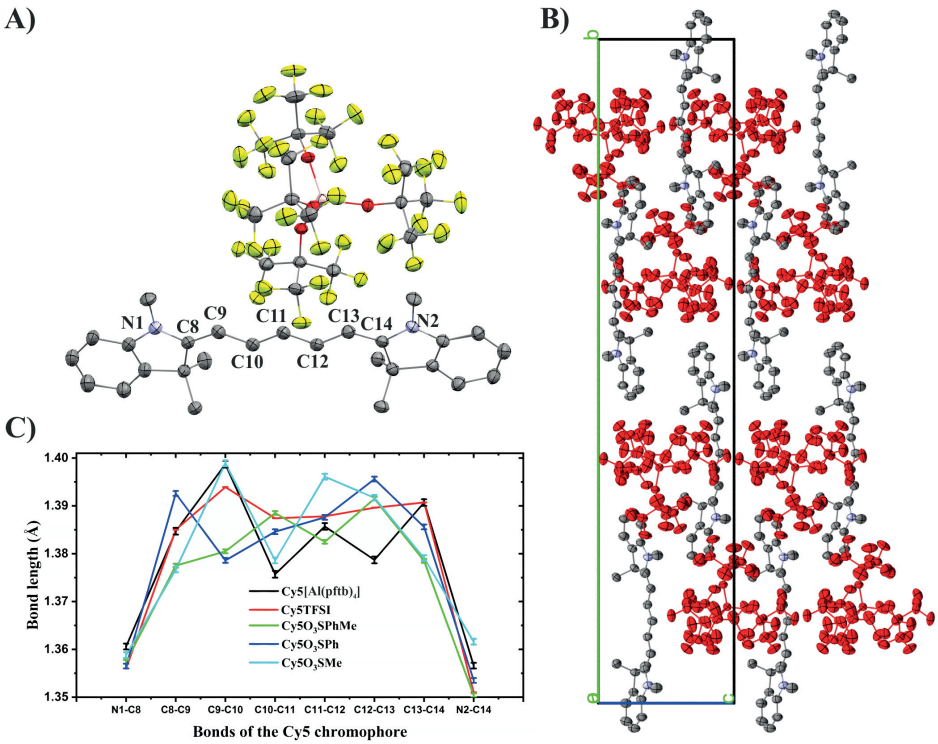

Figure 3:1 A) Asymmetric unit representing the Cy5[Al(pftb)$_4$] in ellipsoid view with 30% probability level. The hydrogen atoms and intercalated chlorobenzene solvent molecules are omitted for clarity. Color code: C: grey, N: violet, O: red, F: yellow, Al: purple. B) Molecular arrangement of Cy5[Al(pftb)$_4$] over 2x1x2 unit cells in ellipsoid view with 30% probability level. Hydrogen atoms and intercalated chlorobenzene solvent molecules are omitted. Color code chromophore: C. grey, N, violet. The anions are colored red for clarity reasons. C) Bond length alternation comparison between different salts of the Cy5 chromophore.

A direct comparison of the bond length alternation of the Cy5[Al(pftb)$_4$] compound with different crystalized salts of the pentamethine chromophore, evaluated previously,[43] shows surprisingly high values for the Cy5[Al(pftb)$_4$] compound (**Figure 3:1C**). While previous results suggested a clear trend towards the ideal polymethine state with increasing anion size, [Al(pftb)$_4$]$^-$ breaks the expected trend and introduces a similar bond length alternation as observed for the point charge like sulfonates or also other investigated anions (**Figure 3:1C**).[39,41,43] Particularly the C9-C10 bond length possesses a pronounced single bond character including Cy5O$_3$SMe and Cy5TFSI. These findings can relativize the until now assumed importance of bond length alternation based on single crystal structure data, since we do not observe any drawbacks neither in optical properties nor in organic photovoltaic parameters, as presented in the following.

One way to physically express the qualitative meaning of "weakly coordinating" and to describe the interactions within a salt is to estimate their lattice energy. Single crystal data provides a unique opportunity to estimate molecular volume as well as to calculate lattice energy and Coulomb interactions of all crystalized pentamethine chromophore salts (**Table S1, S2**). These values can be correlated to photophysical or organic photovoltaic device properties allowing a general description of organic salt semiconductor properties. All presented values were estimated by a method described in the literature.[44,45] As expected, the lattice energy represents the inverse of the molecular volume and reaches its minimum for the [Al(pftb)$_4$] anion containing Cy5 salt.

3.5.2 Optical and Thermal Properties

Cy5[Al(pftb)$_4$] exhibits a high molar extinction coefficient of 3.55 x 10^5 L mol^{-1} cm^{-1} extracted from an absorption band ranging from 500 to 700 nm in ethanol solution, proving that the anion does not influence the optical properties; the latter being very similar to those in other salt solutions of this chromophore (**Figure 2A, S3, Table S5, S6**).[43] Major differences lie in the UV-Vis solid state spectrum of Cy5[Al(pftb)$_4$], which is free of aggregates and approaches the monomeric state regarding the shoulder to peak ratio (1:0.72, 1353 cm^{-1}) and band width of 5793 cm^{-1}, which is only about 1669 cm^{-1} wider than the solution band width of 4124 cm^{-1}. Applying the lattice energy concept in **Figure 3:2B** a first quantitative correlation against solid state optical properties is made, quantifying anions influence on the peak width.

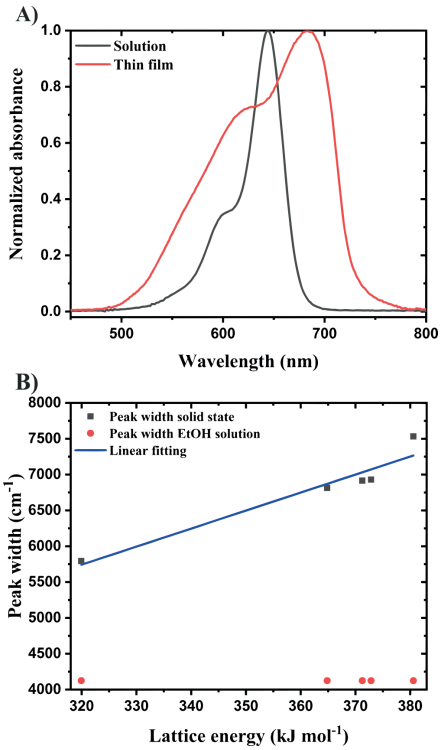

Figure 3:2 A) Normalized UV-Vis absorbance spectra of Cy5[Al(pftb)$_4$] from ethanol solution and 15 nm thick spin-casted film. B) UV-Vis solid state absorbance bandwidth dependence on lattice energy and comparison with the bandwidth in solution (R^2: 0.93 and Pearson's r: 0.96). The lattice energy represents the following materials: Cy5O$_3$SMe (380.57 kJ mol^{-1}), Cy5O$_3$SPh (372.84 kJ mol^{-1}), Cy5O$_3$SPhMe (371.24 kJ mol^{-1}), Cy5TFSI (364.83 kJ mol^{-1}), Cy5[Al(pftb)$_4$] (319.92 kJ mol^{-1}).

Photoluminescence spectra of 10 nm thick neat spin-cast films were recorded at 532 nm excitation wavelength (**Figure S4**). Photoluminescence measurements can be seen as a direct reflection of the individual anions' ability to stabilize the chromophore in the

excited state (**Figure 3:3A, B**). Spin-casted film thicknesses of 10±1 nm, as controlled using spectroscopic ellipsometry paired with smooth and defect free film morphology, same light emitting chromophore, fixed laser excitation power as well as measurement setup allow having photoluminescence properties depending only on the anion. In comparison with the methane sulfonate anion as a benchmark, the variation of organic moieties increases the fluorescence intensity by a factor of 1.5 for the $^{-}O_3SNaphth$ anion. Moderate improvement is achieved with the $TFSI^-$ anion, allowing a pronounced peak formation, achieving a 7-fold increase. When $[Al(pftb)_4]^-$ is employed, a clear emission peak enveloped boosting the intensity up to 5-times when compared to the TFSI anion containing salt. Additionally the lattice energy was found to be inversely proportional to the fluorescence intensity (**Figure 3:3A**).

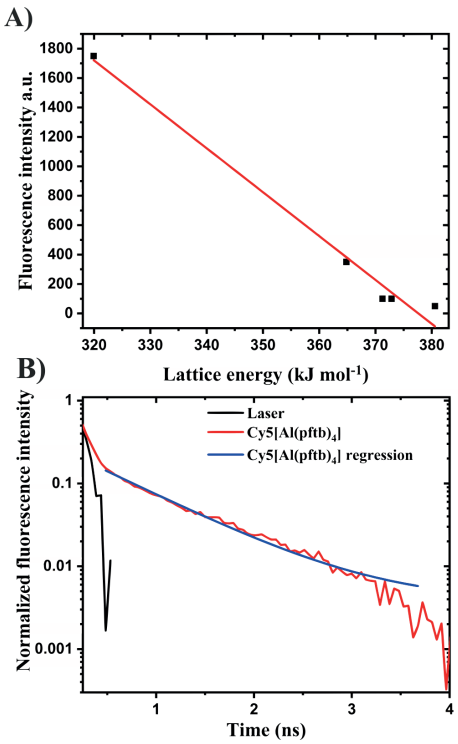

Figure 3:3 A) Fluorescence intensity obtained at 709 nm emission maxima from 10 nm thick spin-casted films plotted against the lattice energy of the corresponding Cy5 salts with R^2 of 0.99 and Pearson's r of -0.99. The lattice energy represents the following materials: $Cy5O_3SMe$ (380.57 kJ mol^{-1}), $Cy5O_3SPh$ (372.84 kJ mol^{-1}), $Cy5O_3SPhMe$ (371.24 kJ mol^{-1}), Cy5TFSI (364.83 kJ mol^{-1}), $Cy5[Al(pftb)_4]$ (319.92 kJ mol^{-1}). B) Fluorescence lifetime of $Cy5[Al(pftb)_4]$. The exponential regression has the form $y=3.79*10^{-3}+1.49*10^{-1}*\exp(-(x-4.37*10^{-1})/7.51*10^{-1}$ with a R^2 of 0.99.

The absolute quantum yield follows this trend towards higher values with decreasing lattice energy (**Table S8**). A remarkable 6-fold increase in quantum yield can be observed from $^{-}O_3SMe$ towards the superweak coordinating $[Al(pftb)_4]^-$ anion. However cyanine dye neat films are known for their low quantum yield making this measurement challenging and afflicted towards increased error, due to non-emissive decay pathways or quenching by hole transporting interlayers (**Table S8**). Additionally cyanine dye films casted on neat glass as required for the measurement form dewetted droplets introducing thickness fluctuations, self-absorbance and aggregate based quenching. On the contrary, fluorescence intensity can be relatively easily obtained by controlling the thickness and morphology of the cyanine film. However, fluorescence decay with a fluorescence lifetime of 0.75 ns could only be detected with the $Cy5[Al(pftb)_4]$ compound due to the limited time resolution of 50 ps of our detection system (**Figure 3:3B**). Accordingly, the sulfonate and bistriflylimide based salts must have radiative lifetimes shorter than 50 ps.

Cyanine dyes are able to exhibit unusual thermal behaviour when weak coordinating anions are used. As already known, the melting point of the different pentamethine based cyanine salts presented in previous work lays above 150 °C.[43] In principal, weakly coordinating anions are expected to lower the melting point mainly by preventing strong Coulomb interactions and closed packed stacking in the solid state. However this expected behaviour has to compete against the boosted molecular weight of the cyanine salt exceeding 1300 g mol^{-1}. Indeed the melting point for $Cy5[Al(pftb)_4]$ approaches 215 °C which is an increase of 70 °C compared to previous investigated salts.[43] The melting point is followed by two sharp peaks, an exothermic one at 269 °C and an endothermal at 279 °C (**Figure 3:4**).

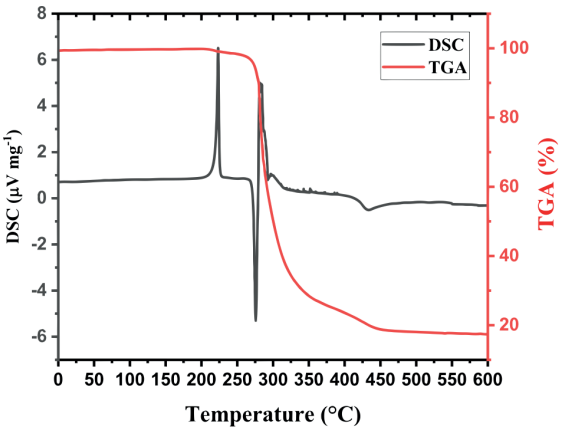

Figure 3:4 In situ thermogravimetric analysis and differential scanning calorimetry (endo up) of Cy5[Al(pftb)$_4$].

Such sequence of three peaks in the DSC indicates an evaporation process accompanied by a partial decomposition as already observed for a trimethine dye [Gesevicius et al, "unpublished"]. Within a temperature range of 225-269 °C a mass loss of 4% occurs in the TGA indicating melt evaporation followed by a rising amount of a degradation product with increasing temperature, leading to a broad one step degradation of the Cy5[Al(pftb)$_4$]. Apparently, the extended polymethine chain leads to an additional thermal instability of the chromophore so that even the [Al(pftb)$_4$]$^-$ anion is not fully capable in bringing the chromophore to the vapour phase without observing a partial decomposition. It can only be speculated whether the fluoride bridged alkoxyaluminate dimer would decrease the lattice energy and the Coulomb interactions enough for that purpose of this hypothetical cyanine salt.[46]

3.5.3 Anion Influence on Thin Film Morphology

Weakly coordinating anions often contain perfluorinated moieties as does the [Al(pftb)$_4$]$^-$. Combined with its size larger than 1nm, one expects the influence of the anion on the surface energy to become more significant. According to literature the aluminium core of the [Al(pftb)$_4$]$^-$ likewise increases the tendency in crystallization.[2,6,9] Indeed, while the solubility in various solvents remained, substrate coating trials from various solvents revealed a strong tendency in either dendritic polycrystallite formation or pronounced dewetting when compared to the previous[43] salts of the pentamethine chromophore (**Figure 3:5, S5**).

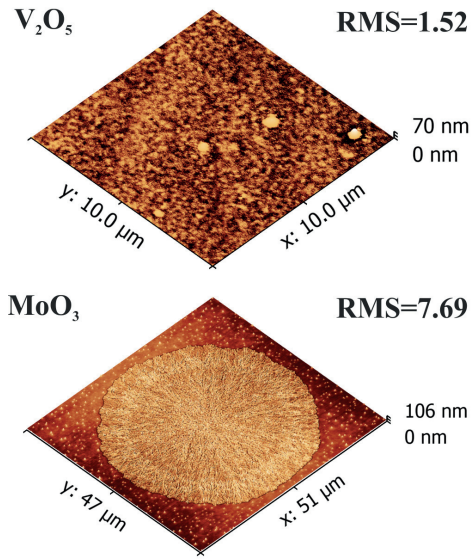

Figure 3:5 AFM images of spin-casted Cy5[Al(pftb)$_4$] films on V_2O_5 and MoO_3 substrates. On MoO_3 a dendritic crystal is observed.

Usual hole transport layers (HTL) such as MoO_3 or PEDOT:PSS seem to provide a strong surface energy mismatch for the Cy5[Al(pftb)$_4$]. Significant improvement yielding an amorphous and defect-free thin film was achieved employing V_2O_5 as HTL (**Figure**

3:5, S5). Films spin-cast from ethanol solution were stable over a sufficient time interval, allowing successful device fabrication. Both MoO_3 and V_2O_5 show similar surface energies of 44.8 and 41.3 mN m^{-1}, respectively. However, the disperse part of V_2O_5 is more pronounced contributing 35.2 mN m^{-1} to the surface free energy, while MoO_3 seems to be more polar showing only 33.9 mN m^{-1} dispersive contribution. In fact, with 11 mN m^{-1} the polar forces of MoO_3 are almost twice as high when compared to 6.1 mN m^{-1} observed in V_2O_5. Finally the Cy5[Al(pftb)$_4$] spin-casted on V_2O_5 yields a surface free energy of 36.9 mN m^{-1}, of which the dispersive forces with 36.4 mN m^{-1} represent the major contribution. Stable Cy5[Al(pftb)$_4$] film formation on V_2O_5 probably originates from an improved match between the dispersive forces of the total surface free energy, which represents the majority contribution for both components.

3.5.4 Anion Influence on OPV Device Performance

Cy5[Al(pftb)$_4$] proved to be a suitable electron donor for a bilayer organic photovoltaic device (**Figure S6**). Test devices under variation of hole transport layer (V_2O_5) and active light absorbing layer thicknesses revealed an optimum value of 15 nm for both V_2O_5 and Cy5[Al(pftb)$_4$] (**Figure S7, S8, S9**). Under optimized conditions on four ITO substrates 8 cells per substrate were fabricated yielding 32 cells in total. 11 cells exhibited a short circuit leaving 21 cells for analysis. **Figure 3:6** depicts the current-voltage (JV) and external quantum efficiency (EQE) characteristics of the best performing cell.

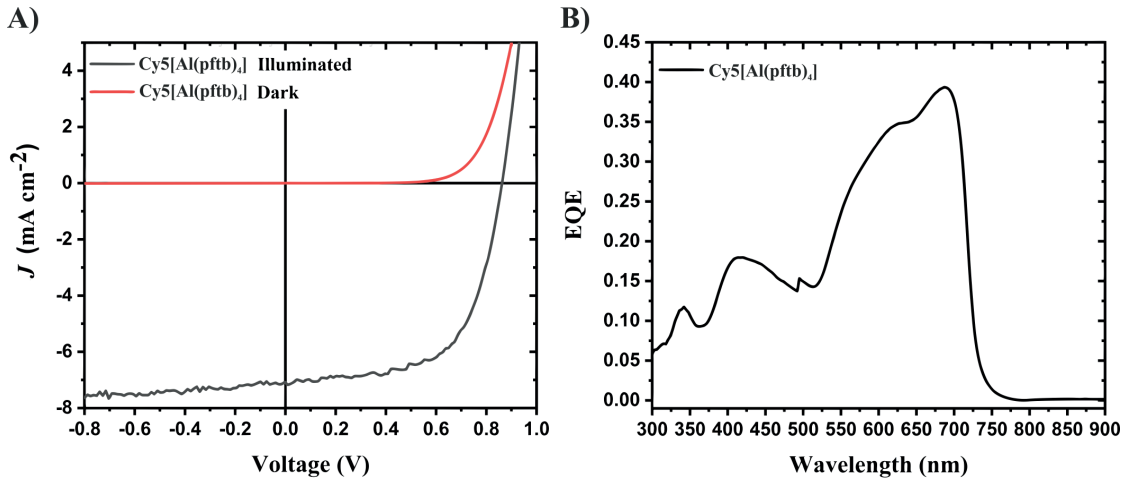

Figure 3:6 Current density vs.Voltage and external quantum efficiency plots of the best performing Cy5[Al(pftb)$_4$] cell.

Low dark current of 1.1 x 10^{-2} mA cm^{-2} at -0.8 V points towards a compact morphology preventing alternative parasitic current pathways. An increased thickness also contributes to the reduction of possible defects within the light absorbing active layer. A high open circuit voltage (V_{OC}) of 0.86 V and short circuit current (J_{SC}) of 7.1 mA cm^{-2} with a solid fill factor (FF) of 62% lead to a champion device performance (η) of 3.8%. This 40% increase in η when compared to the Cy5TFSI device from previous work[43] is mainly driven by 21% enhancement in V_{OC} and 16% in FF, respectively. All parameters show little variation resulting in averaged values close to the champion device with small standard deviations (**Table S9**). Interestingly an active light absorbing layer thickness of 15 nm was found to be optimal, pointing towards an enhanced exciton diffusion length by the [Al(pftb)$_4$]$^-$ anion, which has also a supportive effect on the high J_{SC} and FF values (**Figure S9**). This rise in exciton diffusion length points towards reduced Coulomb forces within Cy5[Al(pftb)$_4$] and less energetic disorder in films of this compound.

Both components contribute to the photovoltaic effect with an external quantum efficiency of 39% at λ_{max}, wherein the major contribution originates from the dye in contrast to devices from previous work (**Figure 3:6B**) where the C60 contribution dominates.[43] This major difference reflects the stabilization ability of the $^-$[Al(pftb)$_4$] anion in cyanine dye based electronic devices. Furthermore, the calculated J_{SC} of 5.7 mA cm^{-2} from the EQE spectrum shows a good match with the averaged values.

Knowing the lattice energy of the organic salts allows comparing the OPV device parameters obtained from different salts on a universal energy scale (**Figure 3:7**). A linear correlation of V_{OC} with the respective coefficient of determination (R^2) of 0.97 is observed with decreasing lattice energy (**Figure 3:7**).

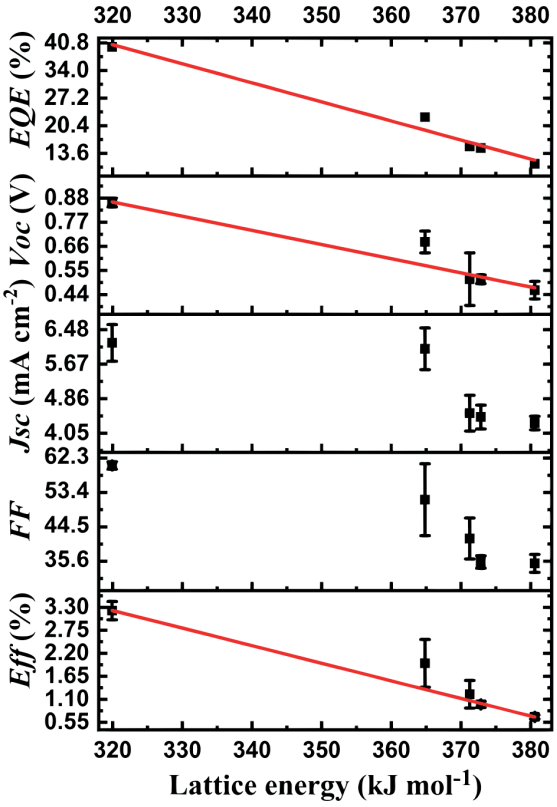

Figure 3:7 OPV device parameters plotted against lattice energy of various Cy5 salts. The lattice energy represents the following materials: $Cy5O_3SMe$ (380.57 kJ mol^{-1}), $Cy5O_3SPh$ (372.84 kJ mol^{-1}), $Cy5O_3SPhMe$ (371.24 kJ mol^{-1}), Cy5TFSI (364.83 kJ mol^{-1}), $Cy5[Al(pftb)_4]$ (319.92 kJ mol^{-1}). Each data point for EQE, FF, J_{sc}, V_{oc} and Eff (η) contain averaged values with their standard deviation. The data points for EQE were taken from best performing cells at maximum conversion wavelength. The linear correlation curves in red have an R^2/Pearson's r of 0.98/-0.99, 0.97/-0.99 and 0.99/-0.99 for EQE, V_{OC} and Eff (η) respectively.

Since V_{OC} in the first instance can be seen as a material property, which is decoupled from the device architecture and fabrication steps, it becomes clear that the $[Al(pftb)_4]^-$ anion has the strongest influence on the HOMO level downshift towards a larger donor-acceptor energy gap, since it is the weakest coordinating anion known to be suitable for OPV applications.[47] We explain this phenomenon by reduced transfer integrals, which lead to a narrower distribution of HOMO and LUMO energy levels within the material.[48,49] This decrease in energetic disorder causes a larger gap between HOMO and LUMO which results in a significant V_{OC} gain. Large spacing between the molecules caused by the steric hindrance of the weakly coordinating anions and reduced Coulomb interactions favour weak molecular orbital overlaps, contrast to conventional anions with localized negative charge.

Despite the linear increase of V_{oc} and η, the J_{sc} and the Fill Factor (FF) both exhibit additional losses for the sulfonate anions interrupting the linear correlation. These additional losses are most likely caused by exciton localization due to strong Coulomb forces and charge trapping in the disordered films incorporating point like charge sulfonate anions. In terms of the molecular arrangement the chromophores with sulfonate counterions experience significant attraction forces leading towards partial noncovalent chromophore overlap which causes aggregation phenomena. In good agreement stands also the non-measureable fluorescence intensity and excited state lifetimes of the sulfonate based salts. Shunting effects influencing the JV curve shapes cannot be neglected either. The FF also suffers from bimolecular recombination due to low mobility and interpenetrating phases as pointed out in the literature.[50] However both J_{SC} and FF are driven to their maximum for the Cy5 chromophore when $[Al(pftb)_4]^-$ is employed and approach the higher limit values for the FF found in organic semiconductors.[30,51] In case of $Cy5[Al(pftb)_4]$ the J_{sc} thrives also due to the increased active light absorbing layer thickness of 15 nm and increased number of monomeric species within the amorphous film by reduction of aggregate formation visible from the solid state UV-Vis spectrum (**Figure 3:2A, B**).

Considering the efficiency which implements all the discussed JV parameters, a similar behaviour to the V_{OC} is observed. A linear correlation with R^2 of 0.99 down to a lattice energy of 319.92 kJ mol^{-1} representing the Cy5[Al(pftb)$_4$] is resulting in a high average value of 3.2% pointing towards highly efficient OPV devices naturally limited by device physics.[52]

An intriguing behaviour can also be found for the dielectric constant when correlated to the lattice energy of various Cy5 chromophore salts (**Figure S12, Table S10**). Since the dielectric constant is dependent on the Coulomb force and expresses the compounds' ability to be polarized, a drop occurs with decreasing lattice energy of the cyanine salts. Likewise the Cy5[Al(pftb)$_4$] which possesses the lowest dielectric constant shows also the highest performance of all investigated pentamethine cyanine salts in an OPV device.

The improved ability of converting the incident photons to charge carriers by tuning the lattice energy is very well represented for different salts of the Cy5 chromophore (**Figure 3:7**). The proportional rise of EQE (R^2 = 0.98) at λ_{max} of the investigated salts with decreasing lattice energy directly quantifies the ability of the superweak coordinating anion both by stabilizing the excited state and reducing charge transfer binding energy. We postulate that the linear correlated V_{OC}, EQE and η dependence on the lattice energy implements a new concept that can be generalized and used for prediction and simulation approaches considering any ionic semiconductor, as far as the device architecture is kept constant.

3.6 Conclusion

In this work two concepts were used to create an organic/inorganic hybrid salt semiconductor between a cyanine dye and a superweak coordinating anion unifying desirable properties from both classes of materials. Direct comparisons were made between salts of the Cy5 chromophore realized in previous work. Lattice energy was implemented as a general descriptor for organic salt semiconductor properties and setting first values for further refined calculations and experimental measurements. The superweak coordinating [Al(pftb)$_4$]$^-$ anion substantially lowers the lattice energy and Coulomb interactions of the pentamethine chromophore to its minimum. Excited state stabilization is reflected in the highest fluorescence intensity, absolute quantum yield as well as longest fluorescence lifetime for the Cy5[Al(pftb)$_4$] compound allowing an efficient exciton splitting at the dye/C_{60} interface. Monomeric conditions are approached in the solid state yielding aggregate free and highly amorphous thin film with low overall surface roughness. All OPV figures of merit are boosted to their maxima for the pentamethine chromophore when [Al(pftb)$_4$]$^-$ anion is used, yielding a champion device with a power conversion efficiency of 3.8%. Additionally V_{OC}, EQE and η exhibited linear correlation when plotted against lattice energy. This proof of concept paves a future synthetic and descriptive pathway for all charged organic semiconductors and dyes where ever a highly stabilized excited state is needed.

3.7 Experimental Section

3.7.1 Materials and Methods

All chemicals and solvents were purchased from commercial sources (*Aldrich, VWR, FEW Chemicals, Kurt J. Lesker*) and used as received, unless otherwise stated. Reactions were carried out under air atmosphere using common lab glass ware. NMR multicore spectra were recorded on a *Bruker AV-400* spectrometer (^{1}H-NMR: 400 MHz, ^{13}C{^{1}H}-NMR: 100 MHz, ^{19}F{^{1}H}-NMR: 377 MHz). Chemical shifts (δ) are reported in ppm (parts per million) with the solvent residual signal (^{1}H/^{13}C{^{1}H}: 7.20/79 for $CDCl_3$) as reference. J coupling constants are given in Hz. Multiplicities are reported as singlet (s), doublet (d), triplet (t), quartet (q), multiplet (m). Thermal gravimetric analysis was recorded on a *Netzsch TG 209 F1*.

3.7.2 Device Fabrication and Characterisation

Glass/ITO substrates were cleaned in acetone (*VWR*, 99.5% GPR RECTAPUR), isopropanol (*VWR*, EMPLURA), ethanol (*VWR*, 99.5% AnalaR NORMAPUR®), detergent (Hellmanex® III, 2 wt% water solution) and finally washed four times with deionised water. Evaporation of V_2O_5 (99.97%) hole transport layer and C_{60} (99.5%) electron acceptor as well as Tris(8-hydroxyquinolinato)aluminium (99.99%) diffusion blocking layer and silver (99.99%) as the top electrode were performed in a glovebox using vapour deposition techniques. The pressure in the evaporation chamber did not exceed $6x10^{-6}$ mbar. The deposition rate was kept constant at 0.2 Å s^{-1}. The active light absorbing layer was spin-coated at a constant speed of 4000 rpm for 1 min in the glovebox under nitrogen atmosphere. The corresponding dye solutions (**Figure S7**) were prepared in the glovebox under nitrogen atmosphere and were filtrated over a 0.45 µm filter before spin-casting. The cell areas were defined with 3.1 and 7.1 mm^2 by using a mask for cathode deposition. The solar cells were characterised under inert gas atmosphere on a calibrated solar simulator (Spectra Nova) using a Xe lamp with 100 mW cm^{-2} simulated AM1.5G solar irradiation. The light intensity was adjusted using a calibrated silicon reference cell from Rera Solutions. External quantum efficiency was performed on a SpeQuest RR-2100.

3.7.3 Further Characterisation

UV-Vis spectra were measured on a Varian Cary 50. Measurement of *n* and *k* was performed using a spectroscopic ellipsometer M2000-VI (J.A. Woollam). The AFM analysis was performed on a scanning probe microscope Bruker Icon3 in tapping mode. Contact angle measurement and surface free energy calculation was performed on a Krüss Drop Shape Analyser. Single crystal diffraction patterns were recorded on a Stoe Mark II-Imaging Plate Diffractometer System (Stoe & Cie, 2015) equipped with a graphite-monochromator. Data collection was performed at –100˚C using Mo-Kα radiation (λ = 0.71073 Å). The structure was solved by direct methods using the program SHELXS and refined by full matrix least squares on F^2 with SHELXL using the graphical user interface Olex2.[53,54] The hydrogen atoms were included in calculated positions and treated as riding atoms using SHELXL-97 default parameters. All non-hydrogen atoms were refined anisotropically. CCDC 1858881 contains the supplementary crystallographic data for Cy5[Al(pftb)$_4$]. These data can be obtained free of charge from The Cambridge Crystallographic Data Centre via www.ccdc.cam.ac.uk/data_request/cif. Detailed information of the described experiments can be found in the supporting information.

Photoluminescence spectra were measured with a CCD fiber spectrometer (LR1, Aseq Instruments) with a 638 nm CW laser diode. PL emission from the samples passed through a long-pass optical filter with an edge at 650 nm in order to reject the excitation laser line. Time-resolved photoluminescence (TRPL) traces were recorded with a 532 nm excitation source (a frequency-doublet, Nd:YAG laser, Duetto from Time-Bandwidth). Scattered laser emission was filtered out using dielectric long-pass filters with edges at 550 nm. Measurements were performed using a time-correlated single photon counting (TCSPC) setup, equipped with a SPC-130-EM counting module (Becker & Hickl GmbH) and an IDQ-ID-100-20-ULN avalanche photodiode (Quantique) for recording the decay traces. Absolute values of the photoluminescence quantum yield (PLQY) were measured with a Quantaurus-QY C11347 spectrometer from Hamamatsu in low-QY mode with excitation by an external broadband Xe-lamp filtered by short-pass filter with edge at 650nm.

3.8 Supporting Information

3.8.1 General Information

3.8.2 General Notation for this Work

- Two symmetrical indolenine derivatives connected with a pentamethine chain

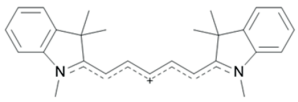

2-[5-(1,3-dihydro-1,3,3-trimethyl-2H-indol-2-ylidene)-1,3-pentadien-1-yl]-1,3,3-trimethyl-3H-indolium (Cy5)

- Superweak coordinating anion

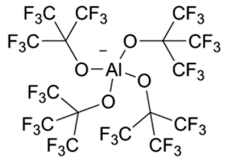

Tetrakis(nonafluoro-*tert*-butoxy)aluminate $[Al(pftb)_4]^-$

- Abbreviation for the dye used in this work

Cy5[Al(pftb)$_4$]

Figure S 1. Overview of the used notation of the compound for this work.

3.8.3 Anion Exchange Procedure

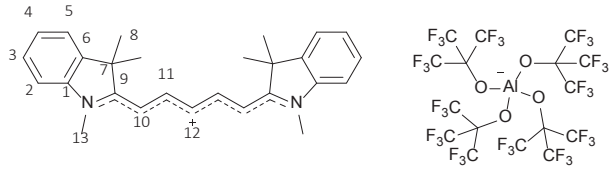

1.00 g, (1.03 x 10^{-3} mol) Lithium tetrakis(nonafluoro-*tert*-butoxy)aluminate and 0.43 g 2-[5-(1,3-dihydro-1,3,3-trimethyl-2H-indol-2-ylidene)-1,3-pentadien-1-yl]-1,3,3-trimethyl-3H-indolium chloride were dissolved in 100 mL chlorobenzene. The mixture was stirred overnight followed by 1 h of ultra-sonication at room temperature. After filtration and evaporation of all volatile compounds the reaction yielded 1.38 g of a blue powder.

$[C_{43}H_{30}AlF_{36}N_2O_4]$ 1349.65 g mol^{-1}

^{1}H NMR (400 MHz, Chloroform-*d*) δ: 7.79 (dd, *J* = 13.5, 12.6 Hz, 2H, H(11)), 7.44 (m, 2H, H(3)), 7.41 (d, 2H, *J* = 8.4 Hz, H(5)), 7.29 (td, *J* = 7.5, 0.9 Hz, 2H, H(4)), 7.12 (d, *J* = 7.8 Hz, 2H, H(2)), 6.46 (t, *J* = 12.5 Hz, 1H, H(12)), 6.03 (d, *J* = 13.6 Hz, 2H, H(10)), 3.55 (s, 6H, H(13)), 1.70 (s, 12H, H(8)) ppm.

^{13}C NMR (101 MHz, Chloroform-*d*) δ: 173.9 (C9), 153.2 C(11), 142.5 (C1), 140.8 (C6), 129.1 (C3), 126.1 (C4), 125.1 (C12), 122.9 (C5), 121.3 (q, J = 293 Hz, CF_3), 110.6 C(2), 103.2 (C10), 79.0 (bp, $C(CF_3)_3$), 49.5 (C7), 31.1 (C13) 28.0 (C8) ppm.

^{19}F NMR (377 MHz, Chloroform-*d*) δ: -75.4 (s, 36F) ppm.

3.8.4 Crystal Structure

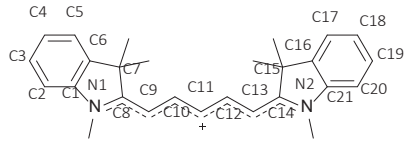

Figure S 2. Cyanine atom numbering.

All crystal structures solutions and refinements were performed with common crystallographic software.[2,3]

3.8.5 Overview about possible ways to access parameters describing anion-cation interactions in a single crystal

Formula used to calculate the lattice energy:

Since the anions and cations are complex molecules built from several atoms the term cation/anion radii needs further specifications and assumptions. Additionally the positive and negative charges are delocalised over several atoms. Therefore the coordination distance determination between the cation and anion is not a trivial task.

One common disadvantage of usual methods is that the ions are treated as spherical objects. This assumption causes strong deviations from the real situation where the ions represent several covalent bound atoms of irregular shape.

A simple and reliable model was developed for complex molecular ions which translates the ionic radii into a molecular volume.[2] The molecular volume can be precisely calculated for any geometrical shape taking information from the X-Ray structural data.

$$\Delta U = |Z^+||Z^-|\nu\left(\frac{a}{V_m{}^{\frac{1}{3}}} + \beta\right)$$

ΔU = Lattice energy, $|Z^+||Z^-|$ = charge of cation/anion, ν = number of ions per molecule, V_m = molecular volume, a = slope of the regression line: 117.3 kJ mol^{-1} nm (molecular volume against lattice energy of literature known salts), β = intercept of the regression line: 51.9 kJ mol^{-1} (molecular volume against lattice energy of literature known salts).

However, the presented equation for molecular volume can only be used when no intercalated solvents are present within the unit cell. In case of solvate crystals the estimation of molecular volumes becomes a non-trivial task. Olex[3] with implemented SHELXL[4] was used to squeeze all residual electron density assigned to solvent molecules. Subsequently the masked solvent volume was subtracted from the unit cell leading to a corrected unit cell volume. Finally the corrected unit cell volume was divided by coordination number yielding the molecular volume of the corresponding organic salts (**Table S1**).

Table S1. Lattice energy calculation of different Cy5 chromophore salts.

Parameters	**Anion**				
	^-O_3SMe	**^-O_3SPh**	**$^-O_3SPhMe$**	**^-TFSI**	**$[Al(pftb)_4]^-$**
a/nm	4.01284	1.70193	1.11894 (84.938)	1.17454 (103.83)	1.12248
α/(°)	(90)	(90)			(90)
b/nm	1.70323 (135.969)	2.80027 (103.218)	1.17926 (83.146)	1.28785 (105.068)	5.0171 (100.661)
β/(°)					
c/nm	3.80012	2.20323	1.68978 (63.980)	1.37737 (116.063)	1.0425
γ/(°)	(90)	(90)			(90)
Z	24	12	2	2	4
I	1	1	1	1	1
V_m/nm^3	0.609	0.663	0.675	0.726	1.279
E_L/kJ mol^{-1}	380.57	372.84	371.24	364.83	319.92

Overview about possible determination of Coulomb and lattice energy from single crystals:

Formula used to calculate electrostatic Coulomb interactions:

$$E_{Coulomb} = \frac{1}{4\pi\varepsilon\varepsilon_0} \cdot \frac{z^2e^2}{r}$$

Z = ionic charge, r = shortest contact distance between cation and anion, ε_0 = vacuum permittivity, ε = relative permittivity of the material.

Since the original formula assumes spherical anions and cations, the shortest cation-anion contact distance variable leads to a strong deviation from real conditions in complex molecular organic ions. The cation-anion distance can be replaced by the molecular volume.

$$r = \left(\frac{V_m}{2I}\right)^{\frac{1}{3}}$$

This modification provides more realistic values for complex molecular ions.

Table S2. Coulomb energy calculations of different Cy5 chromophore salts.

Parameters	**Anion**				
	$^{-}O_3SMe$	**$^{-}O_3SPh$**	**$^{-}O_3SPhMe$**	**$^{-}TFSI$**	**$[Al(pftb)_4]^-$**
ε	3.53	3.53	3.53	3.46	3.24
ε_0/ F m^{-1}	8.854×10^{-12}	8.854×10^{-12}	8.854×10^{-12}	8.854×10^{-12}	8.854×10^{-12}
z	1	1	1	1	1
e/C	$1.602*10^{-19}$	$1.602*10^{-19}$	$1.602*10^{-19}$	$1.602*10^{-19}$	$1.602*10^{-19}$
r/nm	0.67	0.69	0.69	0.71	0.86
E_c/eV	0.61	0.59	0.59	0.58	0.52

Table S3. Anion influence on bond length (Å) of the chromophore polymethine chain. *Average of the difference between C-C bond lengths in the polymethine chain.

Atom	Bond length (Å)
N1-C8	1.3606
C8-C9	1.3847
C9-C10	1.3987
C10-C11	1.3757
C11-C12	1.3857
C12-C13	1.3787
C13-C14	1.3907
N2-C14	1.3566
BLA*	1.32

Table S4. Anion influence on bending of the chromophore skeleton and indolenium ring conformation measured with Mercury 3.8.

Atoms	Angle (°)
C13-C14-N2-C21	179.5(9)
C11-C12-C13-C14	174.9(7)
C1-N1-C8-C9	177.9(7)
C6-C7-C8-C9	178.3(7)
C8-C9-C10-C11	176.0(4)
C13-C14-C15-C16	178.8(4)

3.8.6 UV-Vis absorbance

To determine the molar extinction coefficient 5.34×10^{-4} mol L^{-1} ethanol stock solution of Cy5[Al(pftb)$_4$] was prepared. Subsequently solutions with eight different concentrations were prepared by diluting the stock solution (**Table S5**).

Table S5. Used concentrations for the generation of calibration points in UV-Vis.

Solution	Concentration (mol L^{-1})
	Cy5[Al(pftb)$_4$]
1	8.32×10^{-8}
2	1.81×10^{-7}
3	1.09×10^{-6}
4	1.32×10^{-6}
5	1.60×10^{-6}
6	2.17×10^{-6}
7	6.08×10^{-6}
8	1.20×10^{-5}

All measurements were performed in a 1 mm quartz glass cuvette using 99.8 % ethanol as reference for the baseline. The relative molar extinction coefficient was calculated by multiplying the slope of the resulting plot of concentration against absorbance intensity by 10.

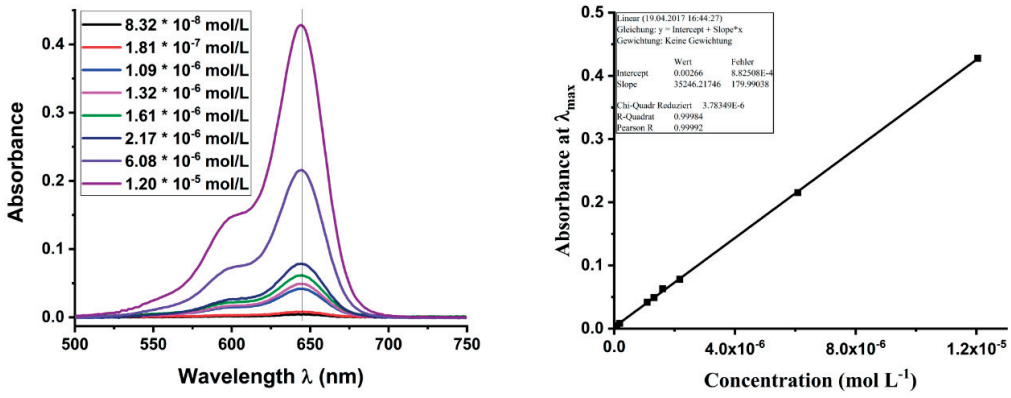

Figure S 3. Concentration dependent absorbance and linear fit of the absorbance maxima against concentration.

The extracted optical data are summarized in **Table S6**. The optical band gap was calculated from the onset of the absorbance at higher wavelengths with the following equation.

$$E_{g(opt)} = \frac{h \times c}{\lambda_{onset}}$$

λ_{onset}: Onset of absorption band at higher wavelength, h: Planck constant, c: speed of light.

The oscillator strength describes the probability of a transition from a lower to an upper energy state. The higher the value the easier the electrons can be excited and the stronger absorbing is the dye.

$$f = 4.319 \times 10^{-9} \int \varepsilon(\upsilon)\, d\upsilon$$

$\varepsilon(\upsilon)$: Molar extinction coefficient as a function of wavenumber, υ: Wavenumber.

The whole absorbance peak was assumed to represent the full band of the lowest energy π-π* transition and was integrated to calculate the oscillator strength.

First the wavelength was converted into wavenumbers with the following formula:

$$\upsilon = 1/(\lambda * 10^{-7})$$

Then the extinction coefficient was calculated for each wavenumber with the following formula:

$$\varepsilon_{(\upsilon)} = A/(c * d)$$

c: concentration in mol·L^{-1}, d: thickness of cuvette in cm, A: absorbance.

The calculations were performed for each recorded data point of the spectra.

Table S6. Calculated data from recorded UV-Vis spectra. * Onset energy at higher wavelengths obtained from EtOH solution.

Compound	ε_{max} (L mol^{-1} cm^{-1})	λ_{max} (nm)	λ_{onset} (nm)	$E_{(onset)}$* (eV)	f
Cy5[Al(pftb)$_4$]	3.52 ×10^5	644	674	1.83	1.48

3.8.7 Fluorescence

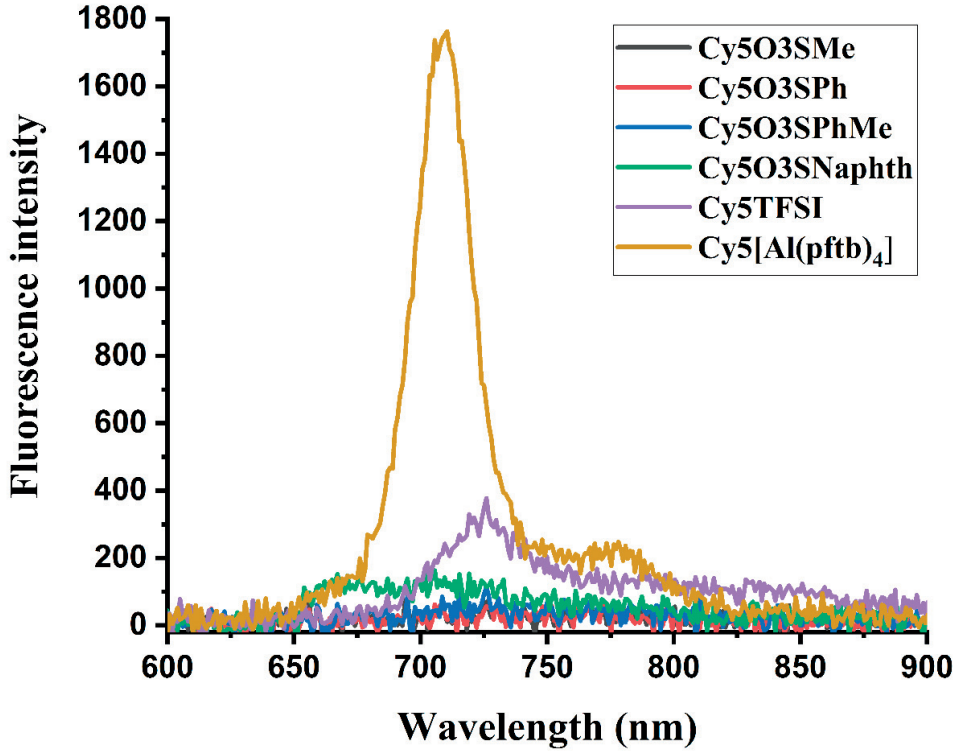

Figure S 4. Fluorescence spectra obtained from 10 nm thick cyanine dye salt films spin-casted on hole transport layers MoO_3 (sulfonate and TFSI containing salts) and V_2O_5 (Cy5[Al(pftb)$_4$]).

Table S8. Quantum yield of cyanine films spin-cast on glass and hole transport layers. MoO_3 was used for sulfonate and TFSI containing salts while V_2O_5 was used for the salt containing the tetrakis(nonafluoro-*tert*-butoxy)aluminate anion.

Compound	Quantum yield on glass (%)	Uncertainty	Quantum yield on HTL (%)	Uncertainty
Cy5O$_3$SMe	4.77×10^{-2}	1.60×10^{-3}	4.74×10^{-4}	1.13×10^{-5}
Cy5O$_3$SPh	4.96×10^{-2}	2.10×10^{-4}	4.85×10^{-4}	3.82×10^{-5}
Cy5O$_3$SPhMe	5.17×10^{-2}	2.2×10^{-3}	4.82×10^{-4}	1.41×10^{-5}
Cy5O$_3$SNaphth	6.04×10^{-2}	3.90×10^{-3}	4.80×10^{-4}	6.85×10^{-5}
Cy5TFSI	9.09×10^{-2}	3.60×10^{-3}	6.19×10^{-4}	2.12×10^{-5}
Cy5[Al(pftb)$_4$]	3.26×10^{-1}	1.80×10^{-2}	1.25×10^{-3}	1.46×10^{-4}

3.8.8 Active Light Absorbing Layer Morphology

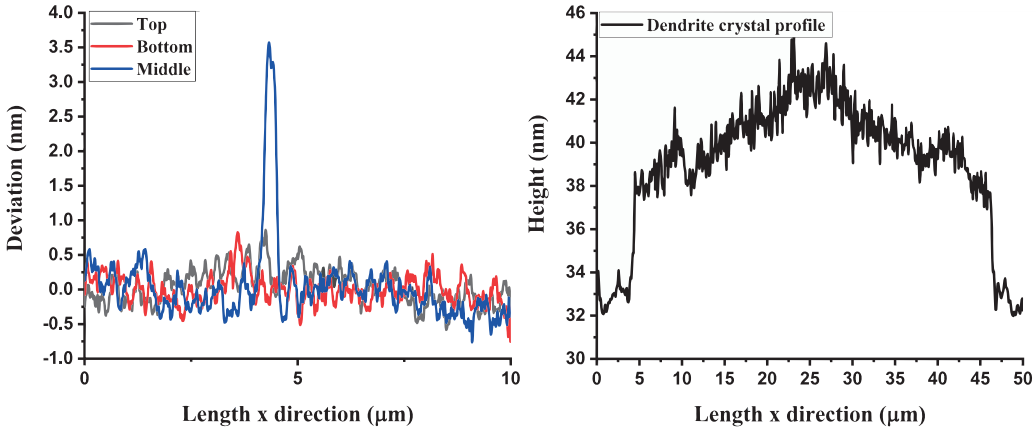

Figure S 5. Left: Roughness profiles of the dye film coated on V_2O_5 hole transport layer extracted from different regions of the AFM scan. Right: Height profile of the dye film coated on MoO_3 hole transport layer.

3.8.9 Organic Photovoltaic Device Fabrication

3.8.10 Used Architecture of the Organic Photovoltaic (OPV) Device

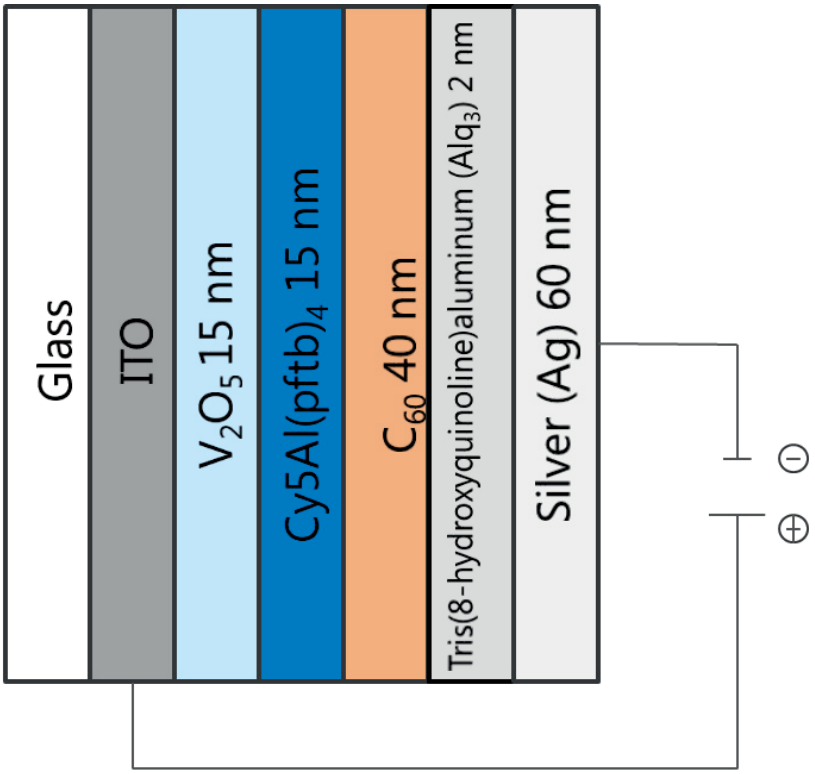

Figure S 6. A sketch of the organic photovoltaic device architecture.

3.8.11 Active Layer Thickness Adjustment

Four concentrations of Cy5[Al(pftb)$_4$] ethanol solution were prepared and spincast at 4000 rpm for 1 min on 15 nm V_2O_5 hole transport layer. Subsequently all samples were analysed by ellipsometry. The obtained thicknesses were plotted against concentration to determine the correlation between thickness and concentration.

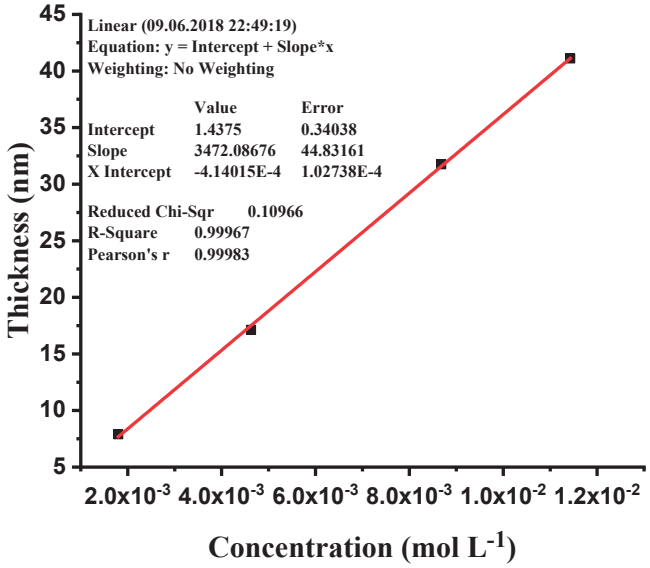

Figure S 7. Correlation between concentration and resulting active layer thickness.

Therefore all necessary concentrations for any desired active layer thicknesses can be determined form the resulting linear equation fit.

3.8.12 Determination of Optimum Hole Transport Layer (HTL) Thickness

Optimum V_2O_5 interlayer thickness was adjusted using fixed 10 nm thick Cy5[Al(pftb)$_4$] layer while varying V_2O_5 thicknesses by 5, 10, 15, 20 and 30 nm. V_2O_5 was thermally deposited on ITO substrates.

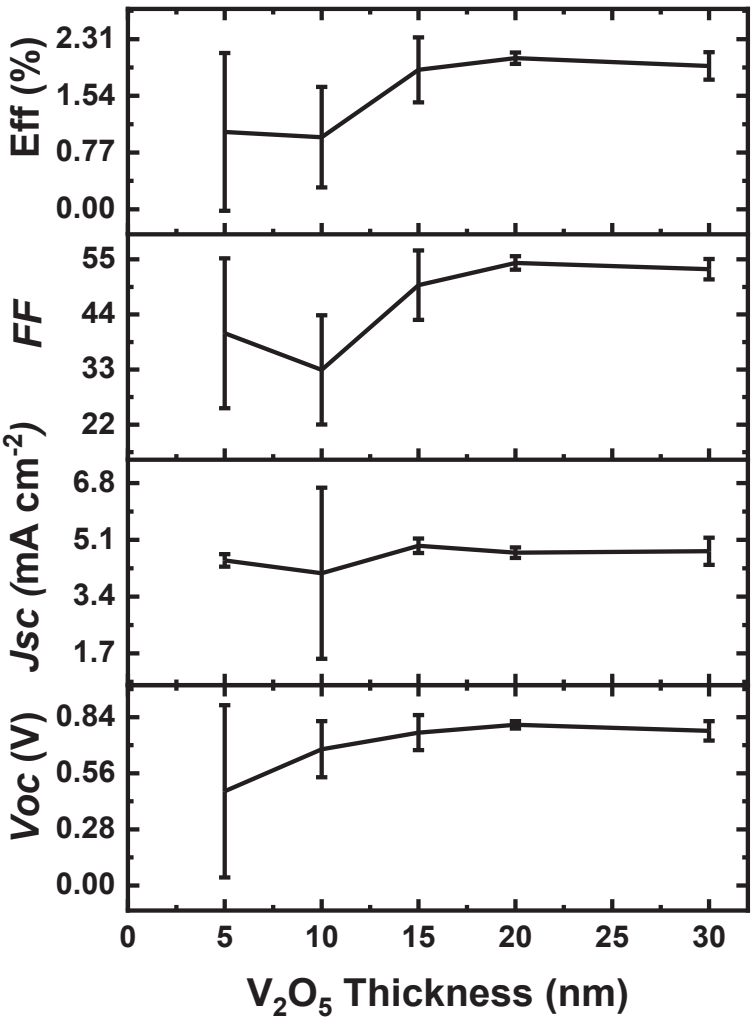

Figure S 8. V_2O_5 thickness vs. JV parameters. Each data point represents averaged values from 8 cells with the corresponding standard deviation.

Thin V_2O_5 layers cause broad standard deviations, which are suppressed at thicker values. All parameters reach their plateau at around 20 nm V_2O_5 thickness. Values exceeding 20 nm V_2O_5 layer thickness cause a slight decrease in all OPV descriptive parameters. Therefore the obtained data indicates 15 nm of V_2O_5 as the optimum hole transport layer thickness with the highest potential for highest obtainable OPV device parameter values.

3.8.13 Determination of Optimum Active Light Absorbing Layer Thickness

After choosing 15 nm as the optimum thickness for the V_2O_5 HTL, the next step was to optimize the active light absorbing layer thickness by depositing 5, 10, 15, 20 and 30 nm of Cy5[Al(pftb)$_4$] on the HTL.

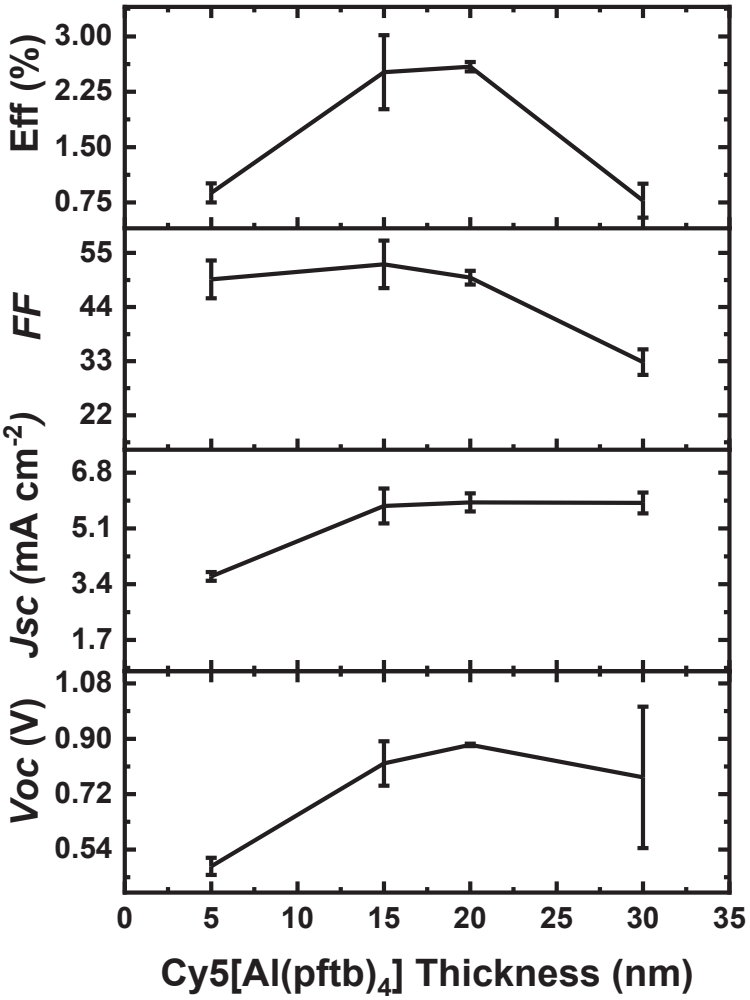

Figure S 9. Cy5[Al(pftb)$_4$] thickness vs. JV parameters. Each data point represents averaged values from 8 cells with the corresponding standard deviation.

All descriptive OPV parameters rise with increasing active layer thicknesses and saturate at 15-20 nm. Thicker Cy5[Al(pftb)$_4$] layers cause a significant drop in all descriptive parameters. 15 nm seems to be the optimum Cy5[Al(pftb)$_4$] thickness with the highest potential for this device configuration.

3.8.14 Optimized Device Descriptive Statistics

The fabrication of the final optimized devices was performed under consideration of the previously determined optimum interlayer thicknesses. Additionally new evaporation boats with freshly loaded material were used. The electrodes inside the evaporation chamber were cleaned by applying high current until all residual material was evaporated as monitored by a quartz sensor. The Cy5[Al(pftb)$_4$] was recrystallized from *t*BuOH and dried for two days at 3×10^{-3} mbar. The final transfer into the glovebox was carried out under vacuum.

Table S9. Descriptive statistics of the optimized Cy5[Al(pftb)$_4$] cells.

	N	$\bar{x}_{arithm}$	s	min	$\bar{x}_{med}$	max
V_{OC}/V	21	0.86	0.02	0.82	0.87	0.89
J_{SC}/mA cm^{-2}	21	6.17	0.43	5.63	6.06	7.23
η	21	3.22	0.23	2.91	3.15	3.79
FF	21	60.41	0.97	58.48	60.28	62.15

3.8.15 Short Circuit Current Density Calculation

The short circuit current density $J_{sc} = \int EQE(\lambda) * \Phi_{AM1.5}(\lambda) * e \, d\lambda$ was obtained by integrating over $EQE(\lambda)$, the photon flux $\Phi_{AM1.5}(\lambda)$ of the AM1.5 solar spectrum and multiplying by the elementary charge *e*.

3.8.16 Relative Permittivity

$$\varepsilon_r = n^2 - k^2$$

ε_r: relative permittivity (dielectric constant or function), n: real part of the index of refraction, k. imaginary part of the index (extinction coefficient)

The orientational polarization or dipole polarisation appears at low frequencies around 10^4 Hz. The n and k values are dependent on the wavelengths. At higher wavelengths however the slope is very low and at a certain wavelength the k value becomes practically 0.

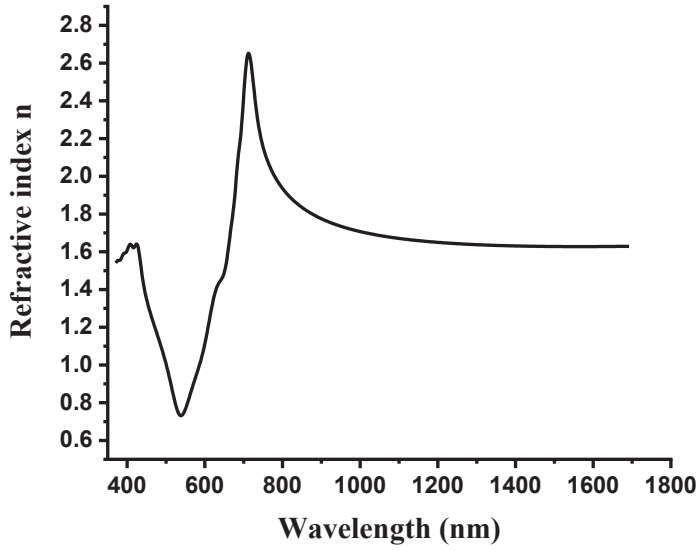

Figure S 10. Function of n depending on the wavelength.

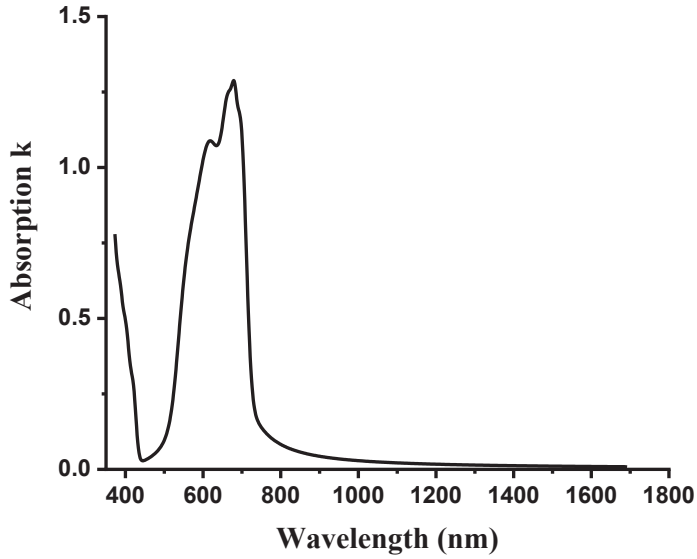

Figure S 11. Absorption coefficient k depending on the wavelength.

Therefore this area was chosen for the calculation of the dielectric constant. The n are given in this table as averaged values over the selected wavelength region.

Table S10. Calculated relative permittivity values for the Cy5[Al(pftb)$_4$].

Cyanine	**n**	**λ/nm**	ε_r
Cy5[Al(pftb)$_4$]	1.64	1000-1688	2.68

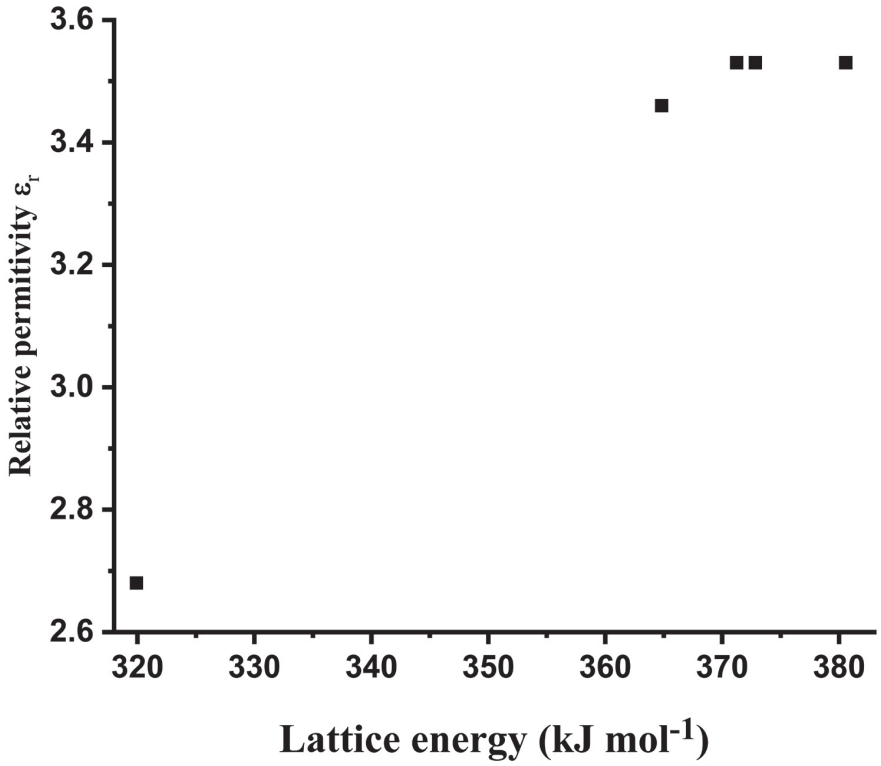

Figure S12. Relative permittivity as function of lattice energy of various Cy5 chromophore salts.

3.8.17 Literature Supporting Information

[1] D. Gesevičius, A. Neels, S. Jenatsch, E. Hack, L. Viani, S. Athanasopoulos, F. Nüesch, J. Heier, *Adv. Sci.* **2017**, *1700496*, 1700496.

[2] H. D. B. Jenkins, H. K. Roobottom, J. Passmore, L. Glasser, *Inorg. Chem.* **1999**, *38*, 3609.

[3] O. V. Dolomanov, L. J. Bourhis, R. J. Gildea, J. A. K. Howard, H. Puschmann, IUCr, *J. Appl. Crystallogr.* **2009**, *42*, 339.

[4] G. M. Sheldrick, *Acta Crystallogr. Sect. C Struct. Chem.* **2015**, *71*, 3.
Sheldrick, G. M. (2008). Acta Cryst. A64, 112-122.

[3] Spek, A. L. (2003). J.Appl.Cryst. 36, 7-13.

3.9 Acknowledgements

The use of the Scanning Probe Microscopy User Laboratory at Empa is gratefully acknowledged. We thank the Swiss National Science Foundation for financial support under grant number 160116.

3.10 References

[1] M. R. Rosenthal, J. Chem. Educ. 1973, 50, 331.

[2] T. S. Cameron, A. Decken, I. Dionne, M. Fang, I. Krossing, J. Passmore, Chem. - A Eur. J. 2002, 8, 3386.

[3] I. M. Riddlestone, A. Kraft, J. Schaefer, I. Krossing, Angew. Chemie Int. Ed. 2018, 57, 13982.

[4] S. H. Strauss, Chem. Rev. 1993, 93, 927.
[5] A. M. Bond, S. R. Ellis, A. F. Hollenkamp, 1988, 5293.
[6] I. Krossing, I. Raabe, Angew. Chemie - Int. Ed. 2004, 43, 2066.
[7] T. A. Engesser, M. R. Lichtenthaler, M. Schleep, I. Krossing, Chem. Soc. Rev. 2016, 45, 789.
[8] C. Reed, Acc. Chem. Res. 1998, 4842, 133.
[9] S. Körbe, P. J. Schreiber, J. Michl, Chem. Rev. 2006, 106, 5208.
[10] I. Krossing, In Comprehensive Inorganic Chemistry II; Elsevier, 2013; pp. 681–705.
[11] E. Y.-X. Chen, S. J. Lancaster, Comprehensive Inorganic Chemistry II; 2013.
[12] C. WINTER, X. ZHOU, M. HEEG, Organometallics 1991, 10, 3799.
[13] I. B. Gorrell, G. Parkin, Inorg. Chem. 1990, 29, 2452.
[14] P. V. Bonnesen, P. V. Bonnesen, C. L. Puckett, C. L. Puckett, R. V. Honeychuck, R. V. Honeychuck, W. H. Hersh, W. H. Hersh, J. Am. Chem. Soc. 1989, 111, 6070.
[15] R. F. Jordan, W. E. Dasher, S. F. Echols, J . Am. Chem. 1986, 108, 1718.
[16] G. Fachinetti, T. Funaioli, P. F. Zanazzi, J. Chem. Soc., Chem. Commun. 1988, 081, 1100.
[17] P. Kölle, H. Nöth, Chem. Rev. 1985, 399.
[18] A. Fallis, J. Chem. Inf. Model. 2013, 53, 1689.
[19] D. Dubois, K. M. Kadish, S. Flanagan, R. E. Haufler, L. P. F. Chibante, L. J. Wilson, J. Am. Chem. Soc. 1991, 113, 4364.
[20] C. Jehoulet, A. J. Bard, F. Wudl, J. Am. Chem. Soc. 1991, 113, 5456.
[21] I. Krossing, Chemistry 2001, 7, 490.
[22] N. Karl, Mol. Cryst. Liq. Cryst. Inc. Nonlinear Opt. 1989, 171, 31.
[23] S. R. Forrest, IEEE J. Sel. Top. Quantum Electron. 2000, 6, 1072.
[24] J. Roncali, P. Leriche, P. Blanchard, Adv. Mater. 2014, 26, 3821.
[25] D. Saccone, S. Galliano, N. Barbero, P. Quagliotto, G. Viscardi, C. Barolo, European J. Org. Chem. 2016, 2016, 2244.
[26] J. L. Bricks, A. D. Kachkovskii, Y. L. Slominskii, A. O. Gerasov, S. V. Popov, Dye. Pigment. 2015, 121, 238.
[27] U. Lawrentz, W. Grahn, K. Lukaszuk, C. Klein, R. Wortmann, A. Feldner, D. Scherer, Chem. - A Eur. J. 2002, 8, 1573.
[28] R. V. Markov, P. A. Chubakov, A. I. Plekhanov, Z. M. Ivanova, N. A. Orlova, T. N. Gerasimova, V. V. Shelkovnikov, J. Knoester, Nonlinear Opt. 2000, 25, 365.
[29] M. Young, J. Suddard-Bangsund, T. J. Patrick, N. Pajares, C. J. Traverse, M. C. Barr, S. Y. Lunt, R. R. Lunt, Adv. Opt. Mater. 2016, 4, 1028.
[30] O. Malinkiewicz, T. Grancha, A. Molina-Ontoria, A. Soriano, H. Brine, H. J. Bolink, Adv. Energy Mater. 2013, 3, 472.
[31] M. Bates, R. R. Lunt, Sustain. Energy Fuels 2017, 1, 955.
[32] J. Suddard-Bangsund, C. J. Traverse, M. Young, T. J. Patrick, Y. Zhao, R. R. Lunt, Adv. Energy Mater. 2016, 6, 1501659.
[33] C. J. Traverse, M. Young, J. Suddard-Bangsund, T. Patrick, M. Bates, P. Chen, B. Wingate, S. Y. Lunt, A. Anctil, R. R. Lunt, Sci. Rep. 2017, 7, 16399.
[34] A. Köhler, H. Bässler, Electron. Process. Org. Semicond. 2015, 87.
[35] S. G. Lias, P. Ausloos, J. Am. Chem. Soc. 1978, 100, 6027.
[36] X. Y. Zhu, Q. Yang, M. Muntwiler, Acc. Chem. Res. 2009, 42, 1779.
[37] O. V Mikhnenko, P. W. M. Blom, T.-Q. Nguyen, Energy Environ. Sci. 2015, 8, 1867.
[38] A. Devižis, J. De Jonghe-Risse, R. Hany, F. Nüesch, S. Jenatsch, V. Gulbinas, J.-E. Moser, J. Am. Chem. Soc. 2015, 137, 8192.
[39] G. Spavieri, G. T. Gillies, M. Rodriguez, Metrologia 2004, 41, S159.
[40] P.-A. Bouit, C. Aronica, L. Toupet, B. Le Guennic, C. Andraud, O. Maury, J. Am. Chem. Soc. 2010, 132, 4328.
[41] O. D. Kachkovski, O. I. Tolmachov, Y. L. Slominskii, M. O. Kudinova, N. O. Derevyanko, O. O. Zhukova, Dye. Pigment. 2005, 64, 207.
[42] T. D. Iordanov, J. L. Davis, A. E. Masunov, A. Levenson, O. V. Przhonska, A. D. Kachkovski, Int. J. Quantum Chem. 2009, 109, 3592.
[43] A. E. Masunov, D. Anderson, A. Y. Freidzon, A. A. Bagaturyants, J. Phys. Chem. A 2015, 119, 6807.
[44] D. Gesevičius, A. Neels, S. Jenatsch, E. Hack, L. Viani, S. Athanasopoulos, F. Nüesch, J. Heier, Adv. Sci. 2018, 5, 1700496.
[45] H. D. B. Jenkins, H. K. Roobottom, J. Passmore, L. Glasser, Inorg. Chem. 1999, 38, 3609.
[46] I. Krossing, J. M. Slattery, C. Daguenet, P. J. Dyson, A. Oleinikova, H. Weingärtner, J. Am. Chem. Soc. 2006, 128, 13427.
[47] A. Bihlmeier, M. Gonsior, I. Raabe, N. Trapp, I. Krossing, Chem. - A Eur. J. 2004, 10, 5041.
[48] A. Martens, P. Weis, M. C. Krummer, M. Kreuzer, A. Meierhöfer, S. C. Meier, J. Bohnenberger, H. Scherer, I. Riddlestone, I. Krossing, Chem. Sci. 2018, 9, 7058.
[49] J. Suddard-Bangsund, C. J. Traverse, M. Young, T. J. Patrick, Y. Zhao, R. R. Lunt, Adv. Energy Mater. 2016, 6, 1501659.
[50] J. L. Bredas, J. P. Calbert, D. A. da Silva Filho, J. Cornil, Proc. Natl. Acad. Sci. 2002, 99, 5804.
[51] A. Troisi, G. Orlandi, J. Phys. Chem. A 2006, 110, 4065.

[52] J. Nelson, Mater. Today 2011, 14, 462.
[53] B. Qi, J. Wang, Phys. Chem. Chem. Phys. Phys. Chem. Chem. Phys 2013, 15, 8972.
[54] S. M. Menke, N. A. Ran, G. C. Bazan, R. H. Friend, Understanding Energy Loss in Organic Solar Cells: Toward a New Efficiency Regime. Joule 2018, 2, 25–35.
[55] G. M. Sheldrick, Acta Crystallogr. Sect. C Struct. Chem. 2015, 71, 3.
[56] O. V. Dolomanov, L. J. Bourhis, R. J. Gildea, J. A. K. Howard, H. Puschmann, IUCr, J. Appl. Crystallogr. 2009, 42, 339.

Chapter 4 Physical Vapor Deposition of Cyanine Salt and First Application in Organic Electronic Devices

Donatas Gesevičius,[a,e] Antonia Neels[b], Léo Duchêne[c], Erwin Hack,[d] Jakob Heier[a] and Frank Nüesch[a,f]*

a. Laboratory for Functional Polymers, Swiss Federal Laboratories for Materials Science and Technology, Empa, Überlandstrasse 129, Dübendorf, Switzerland
b. Center for X-ray Analytics, Swiss Federal Laboratories for Materials Science and Technology, Empa, Überlandstrasse 129, Dübendorf, Switzerland
c. Materials for Energy Conversion, Swiss Federal Laboratories for Materials Science and Technology, Empa, Überlandstrasse 129, Dübendorf, Switzerland
d. Laboratory for Transport at Nanoscale Interfaces, Swiss Federal Laboratories for Materials Science and Technology, Empa, Überlandstrasse 129, Dübendorf, Switzerland
e. Institute of Chemical Sciences and Engineering, ISIC, Ecole Polytechnique Fédérale de Lausanne, EPFL, Station 6, CH-1015 Lausanne, Switzerland
f. Institut des Matériaux, Ecole Polytechnique Fédérale de Lausanne, EPFL, Station 6, CH-1015 Lausanne, Switzerland
E-mail: jakob.heier@empa.ch

4.1 Declaration of Contribution

This chapter is an exact copy of an article to be published in Journal of Materials Chemistry C, which was accepted for publication by the 6th of November 2018. Unless otherwise stated Donatas Gesevičius was responsible for all the experiments and practical work. In all cases, the idea development, interpretation of results and the writing of the manuscript was performed by Donatas Gesevičius. Antonia Neels was responsible for X-Ray analysis. Léo Duchêne was giving an introduction to the quasi-isothermal thermogravimetric measurement techniques. Erwin Hack was supporting the ellipsometry raw data analysis. Frank Nüesch and Jakob Heier were responsible for proofreading, submitting and moderating scientific discussions.

4.2 Keywords

Cyanine dyes, physical vapor deposition, enthalpy of vaporization, morphology, and organic electronics.

4.3 Abstract

A symmetrical trimethine indocyanine dye chromophore was modified with the bistriflylimide anion to study changes in coulomb interactions, thermal stability and the volatility of the organic salt. The bulky bistriflylimide anion minimizes electrostatic interactions and increases the vapour pressure of the compound resulting in an increased volatility of the organic salt. First examples of entirely vacuum-processed bulk heterojunction organic photovoltaic devices show the proof of concept. We give evidence that the well dispersed negative charge of the bistriflylimide introduces quasi gas phase conditions to the cyanine chromophore. This overcomes the existing restriction of thin film formation via spincasting in cyanine dyes based organic electronics and expands the thin film fabrication process choices towards physical vapour deposition.

4.4 Introduction

Organic electronic devices have an over 60 years long history of intense research.[1,2] Besides fundamental understanding of electronic processes in organic semiconductor devices, proper layer formation by suitable deposition techniques plays a crucial role for a successfully working device. In academic research wet film formation processes[3–8] are most popular and especially spincasting[9] is established as a fast technique to form thin films of small area. Despite its popularity, spincasting has several drawbacks such as little control over the desired film geometry. In addition, the resulting film quality strongly depends on substrate surface wetting of the solution. Organic electronic devices in research often consist of several thin layers with similar solubility, making a multistack device fabricated via spincasting a challenging task. However, industry requires large area homogenous thin film layers, high precision in geometry control and long term stability, which is usually achieved by vacuum deposition techniques.[8,10–15]

The majority of small molecule organic semiconductors are neutral.[16] However, indolenium-cyanine dyes belong to the class of organic salts, with a characteristic presence of an electron accepting quarternary ammonia group (antiauxochrome) as well as an electron donating ternary amino moiety (auxochrome) which are connected via a polymethine chain. Such a geometry creates a fully delocalised charge over the polymethine backbone within the cyanine limit and enables many of their attractive optical properties, such as large extinction coefficients.[17–19] Since their discovery in 1856[20] cyanine dyes were used in various applications, according to the scientific interest in each decade starting from photography,[20] CD-R based data storage,[21–24] life science,[25,26] non-linear optics[27,28] and organic photovoltaics (OPV) or photodiodes.[17,29–39]

While neutral organic semiconductors can be easily evaporated mainly due to the weak intermolecular van der Waals forces, ionic organic functional materials such as cyanine dyes suffer from strong Coulomb interactions which results in high melting points and decomposition at ambient temperatures.[40,41] Heteroatoms in the polymethine chain or in aromatic moieties as well as high molecular weight of the cyanine salts and counterions with localised charge induce additional decomposition pathways when thermal stress is applied.[24] These drawbacks prevented successful implementation of physical vapour deposition techniques in cyanine dye based semiconductor research.

Weakly coordinating anions as the key to improve both chromophore stability in the excited state and organic electronic device performance are emerging topics.[37,42] The influence of a weakly coordinating anion on volatility of the cyanine salts was not investigated in the literature so far. Our work presents guidelines for a successful design of evaporable cyanine organic salts with the aim to open future research possibilities regarding synthesis of evaporable cyanine salts, organic electronic device fabrication and optimisation as well as theoretical calculations on new emerging thermodynamic properties. Besides the fundamental interest to overcome present limitations and making a cyanine salt thermally stable but volatile enough to be evaporated before decomposition occurs, we demonstrate first applications in organic electronic devices where thin film formation had taken place by a physical vapour deposition based fabrication method.

4.5 Results and Discussion

4.5.1 From Material Synthesis to Optical and Electrochemical Properties

The bistriflylimide (TFSI) anion was introduced to the 1-ethyl-2-[3-(1-ethyl-1,3-dihydro-3,3-dimethyl-2H-indol-2-ylidene)-1-propen-1-yl]-3,3-dimethyl-3H-indolium iodide (Cy3I), exchanging the partially redox active iodide anion from the starting material by using an Amberlyst® A26 (OH^- form) wet anion exchange resin. The detailed working principles and experimental setup were reported elsewhere.[42] For simplicity the dye shall be denoted as Cy3TFSI (**Figure 4:1, S1**) in the following.

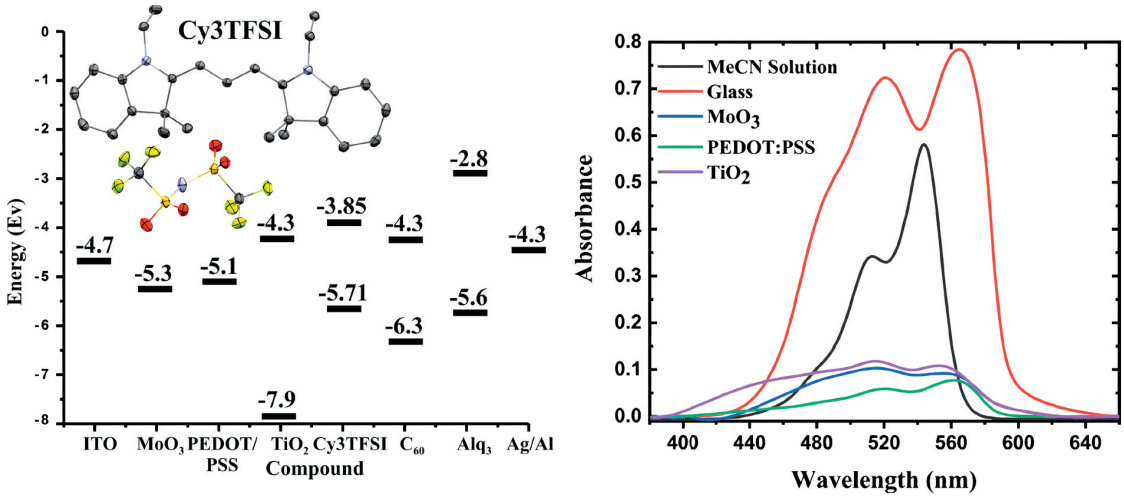

Figure 4:1 On the left: cartoon depicting the molecular structure of the Cy3TFSI salt with the corresponding energy level alignment respective possible device fabrication. On the right: qualitative UV-Vis spectra of evaporated thin films on different substrates.

Four different substrates were chosen and compared to the solution spectrum to investigate the UV-Vis properties of vapour deposited Cy3TFSI films with respect to further application in organic electronic devices (**Figure 4:1, S2**). Cy3TFSI has a absorbance maximum in acetonitrile solution attributed to the 0 → 0 transition at 544 nm with a shoulder shifted by 1182 cm^{-1} towards shorter wavelengths at 512 nm due to a dominant vibronic mode resulting from the 0 → 1 or 0 → 2 transition. The absorbance peak spans a range between 455 and 567 nm. With a relative molar extinction coefficient of 2.40 x 10^5 L mol^{-1} cm^{-1} in acetonitrile solution the dye manifests strong light absorption which is most beneficial to light harvesting in thin films as required for OPV devices (**Figure S3**, **Table S1**). Depending on the substrate used the solid state absorbance broadens up to 1302 cm^{-1} for glass, 2269 cm^{-1} for MoO_3, 3401 cm^{-1} for PEDOT:PSS and 4371 cm^{-1} for mesoporous TiO_2. The blue shifted shoulder grows and becomes a dominant species on TiO_2 (1366 cm^{-1}) and MoO_3 (1496 cm^{-1}) substrates with a measured ratio of 1:0.91 and 1:0.87 respectively. The opposite effect is observed on glass with a shift of 1531 cm^{-1} and PEDOT:PSS (1405 cm^{-1}) showing a ratio between the shoulder and the main peak of 0.92:1 and 0.7:1, respectively. Such differences in peak/shoulder ratios, absorbance peak shapes and shoulder shifts indicate differences in the thin film morphology. A film with large thickness variations could cause the observed peak broadening in UV-Vis due to geometrical reasons and points either towards dewetted or rough surfaces. Dimerization and aggregation effects induced by solid state packing of the molecules could contribute as well to shoulder formation at shorter wavelengths. In general the optical properties of vapour deposited molecules are similar to those from spin casted films.[43]

The Cy3TFSI dye belongs to the class of intermediate band gap semiconductors possessing an electrochemical energy gap of 1.86 eV with intermediate electron affinity and high positive oxidation potential (**Figure S4**, **Table S4**). The TFSI anion is not redox active within the electrochemical window of the chromophore. **Figure 4:1** depicts the relative energy levels of the possible organic electronic device interlayers. With a HOMO of -5.71 eV and LUMO of -3.85 eV, Cy3TFSI can be employed as an electron donor in both standard geometry with the hole collecting layer on the substrate anode as well as in inverted geometry with the electron collecting layer on the substrate cathode.

4.5.2 Factors Enabling Physical Vapour Deposition

Physical vapour deposition in vacuum occurs either by sublimation of a solid or by evaporation of a molten substance. Which process takes place is determined by the triple point of the compound. Both mechanisms require a high thermal stability of the compounds. The combined methods of thermogravimetric analysis (TGA) and differential scanning calorimetry (DSC) reveal a melt based evaporation process for the Cy3TFSI dye (**Figure 4:2, S5**).

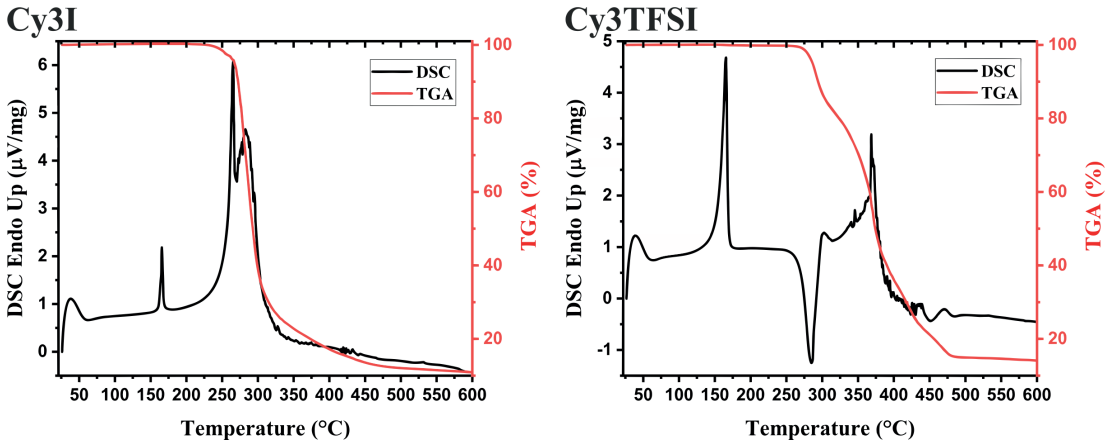

Figure 4:2 Dynamic TGA (10 °C min^{-1}) with corresponding DSC signal of starting material (Cy3I) and Cy3TFSI.

Considering the melting peak onset values, Cy3TFSI has a melting point of 156 °C compared to 165 °C observed for the starting material. Despite the larger molecular weight of Cy3TFSI, the melting point is lowered by 10 °C proving that the bulky anion with its dispersed negative charge reduces intermolecular chromophore interactions. Similar findings regarding the influence of Coulomb interaction on ion pair evaporation were mentioned in the literature on ionic liquids.[44] Significant 2% mass losses were obtained at 280 °C for Cy3TFSI while the starting material reaches this onset already at 252 °C. A low melting point and an increased thermal stability favour a successful evaporation of an organic salt by widening the thermal window until the decomposition temperature is reached. However, the thermal degradation mechanism is not trivial as it is not sufficient to assign an initial mass loss to its decomposition point, especially for a volatile compound. Additionally, literature on ionic liquids points towards significant differences in mass loss mechanisms driven either by vaporisation or decomposition or even simultaneous occurrence of both depending on ultra-high vacuum (UHV), high vacuum (HV) or ambient pressure conditions.[45] Despite material class differences and a different focus of this work we try to adopt some of the experiments from the literature and reveal first insights into the evaporation mechanism of cyanine salts. While the starting material shows a two-step mass loss in dynamic TGA (**Figure 4:2**) with relative integrals of 46 and 42% until the range of 450 °C and two endothermal peaks at 265 and 283 °C (peak maxima) in the DSC suggesting a two-step degradation, the Cy3TFSI has a more complex TGA curve (**Figure 4:2**). Three well distinguished steps can be identified with relative integrals of 19, 26 and 42% accompanied by a sharp exothermal DSC peak at 285 °C (peak maximum).

Evidence that the evaporated Cy3TFSI that comes to a rest on the substrate and the starting material are identical is given by UV-Vis spectroscopy. The solution spectrum of a re-dissolved film matches the solution spectra of the starting material. Differently, with Cy3I also the half-dye is observed (Fig. S5).

The information content of a dynamic TGA measurement is limited regarding the evaporation mechanism of a compound. To extract the enthalpy of vaporisation ($\Delta_1^g H_m^\circ(T_{av})$) at an average temperature as a physical value describing the evaporation process, a quasi-isothermal TGA measurement was performed (supporting information, thermal behaviour section).[46] **Figures** 4:**3, S6, S7** display the differences in mass loss of each isothermal step for Cy3I and Cy3TFSI.

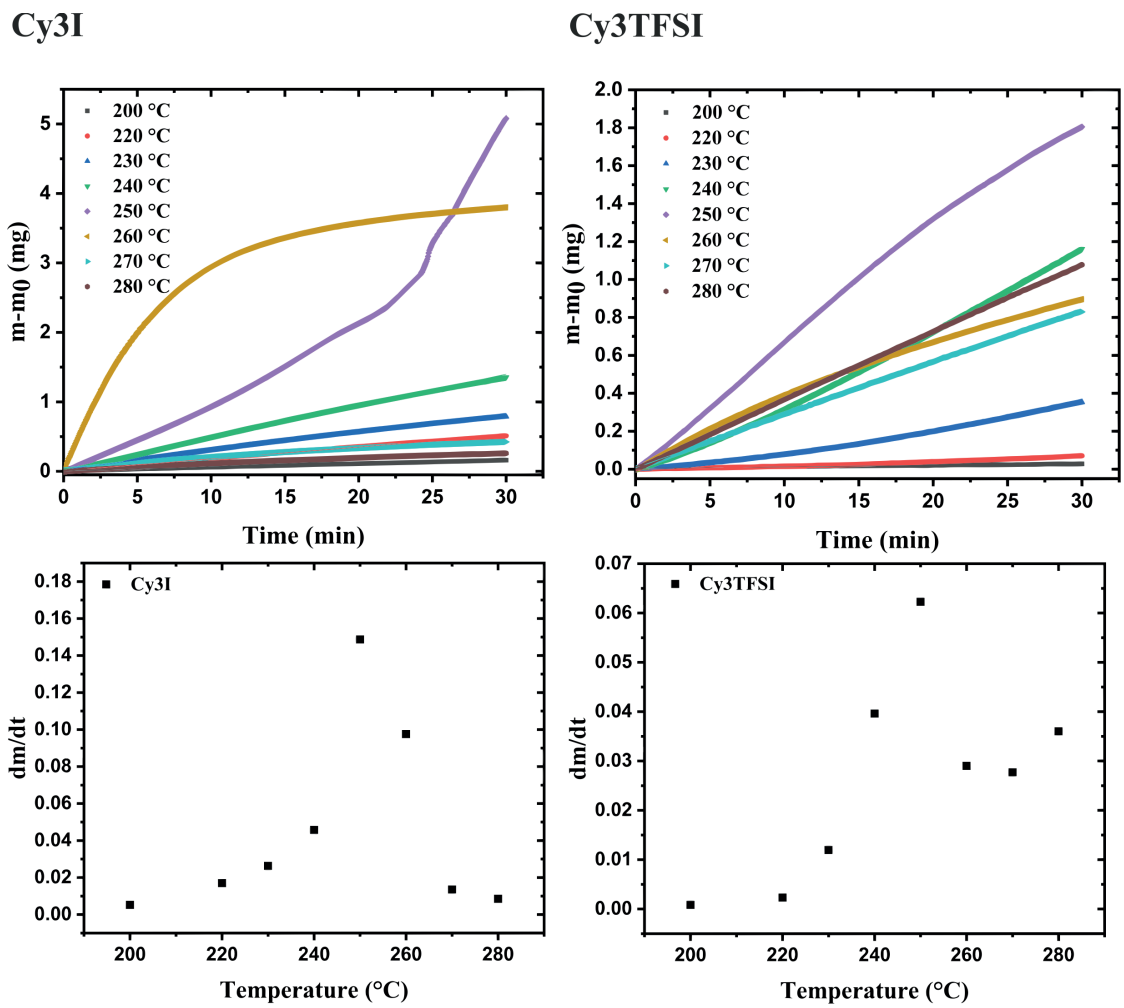

Figure 4:3 The upper row represents extracted weight losses as a function of time occurring during each isothermal step. The lower row represents the extracted slopes of the isothermal weight loss curves as function of temperature.

An evaporation process is expected to have a defined vapour pressure at a given temperature and thus behaves linearly over time while decomposition should occur spontaneously with inconsistent vapour pressure showing a non-linear mass loss over time. The extracted slopes of the isothermal weight loss behave nonlinearly for both materials as a function of temperature. Cy3TFSI possesses a wide linear region from 220-250 °C which can be attributed to the evaporation process. The exponential increase in mass loss of the starting material can be attributed to a simultaneous occurrence of partial evaporation and decomposition mainly visible from UV-Vis spectra of respectively heated samples at a particular temperature (**Figure S8).** Approaching a temperature range above 250 °C both materials show a DSC activity. With the exothermal DSC peak onset at 269 °C for Cy3TFSI the mass loss decreases sharply reaching a local minima at 270 °C pointing towards partial decomposition forming non-volatile degradation products as visible in UV-Vis (**Figure S8**). The unpredictable mass loss decrease over time especially during isothermal steps at 250 and 260 °C with the corresponding broad endothermal DSC peak onset at 260 °C and random distribution of dm/dt vs. T indicate that the Cy3I undergoes unpredictable thermal decomposition only (**Figure 4:3, S6, S7, S8**). The decomposition only pathway is supported by observing a 75% total weight loss for Cy3I compared to only 27% obtained for Cy3TFSI during the measurement. This points towards the assumption that Cy3I forms volatile decomposition species while Cy3TFSI is more stable and decomposes only partially by forming less volatile decomposition species.

Applying the developed model for ionic liquids we obtain a value for $\Delta_1^g H_m^\circ(T_{av})$ of 152.8 kJ mol^{-1} for Cy3TFSI within a temperature range of 220-250 °C (**Table S5**, **S6**, **S7**, **Figure S9**).[46] With this approach we provide first experimental results quantifying the thermal evaporation process of Cy3TFSI which will be helpful in deeper future thermodynamic investigations.

In summary it can be concluded that the literature of thermogravimetric experiments of cyanine dyes has to be revised. The thermal behaviour of cyanine dyes containing weakly coordinating anions is more complicated than assigning the first significant mass loss to a decomposition temperature. Furthermore, the thermal behaviour under ambient pressure may strongly deviate from the conditions inside a HV evaporation chamber, making conclusions even more complex.

The thermal properties of an organic salt are closely linked to its molecular packing as well as with the strength of electrostatic interactions in the solid state. Therefore we link the crystal structure of Cy3TFSI and Cy3I to the physical vapour deposition phenomenon and define the lattice energy as a key parameter. Single crystals were obtained by cooling saturated ethanol solutions. The starting material crystalizes in a monoclinic lattice with the space group $P2_1/c$ while Cy3TFSI belongs to the orthorhombic system with the $P2_12_12_1$ space group. The shortest observed anion coordination distances of 7.65 Å for Cy3TFSI and 5.07 Å for Cy3I in **Figure 4:4** give qualitative insights about reduced electrostatic interactions within Cy3TFSI.

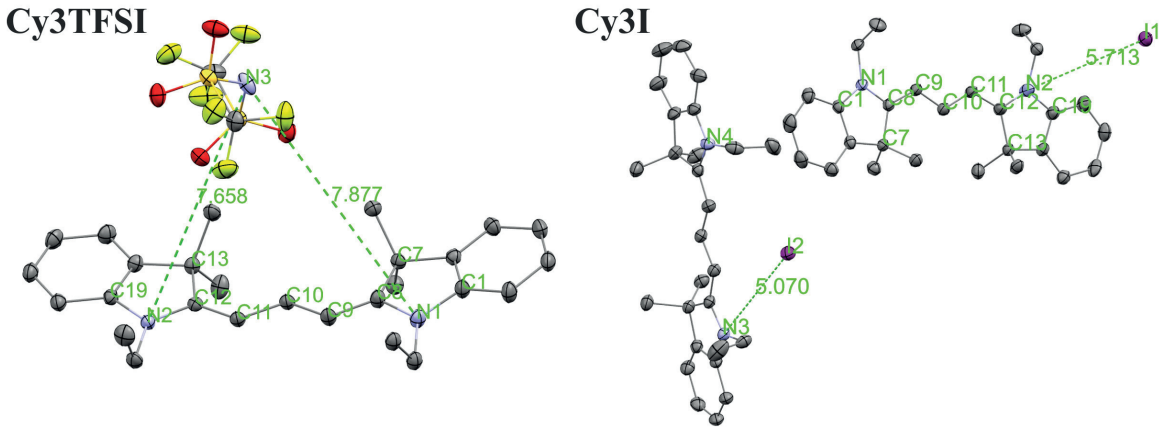

Figure 4:4 Molecular structure and anion coordination environment observed in the single crystal structures of Cy3I and Cy3TFSI. The shortest anion-chromophore distances are given in Å. The thermal ellipsoids represent 50% probability levels. The disorder in Cy3TFSI as well as the hydrogen atoms are omitted for clarity. Color code: C: grey, N: violet, S: yellow, O: red, F: yellow-green, I: purple.

Relative lattice energies of 359.09 kJ mol^{-1} for Cy3TFSI and 376.93 kJ mol^{-1} for Cy3I and the Coulomb interactions of 0.67 eV for Cy3TFSI and 0.77 eV for Cy3I, respectively, were estimated according to a literature method (**Table S8, S9**).[47] The estimated lattice and coulomb energy values are well below the ones obtained for inorganic molecular ions as well as smaller organic ionic liquids and visualise well the strong influence of the bulky bistriflylimide on the thermal stability of the Cy3TFSI chromophore.

The bistriflylimide anion prevents short distance intermolecular chromophore interactions since no regular packing motive can be observed (**Figure 4:5**).

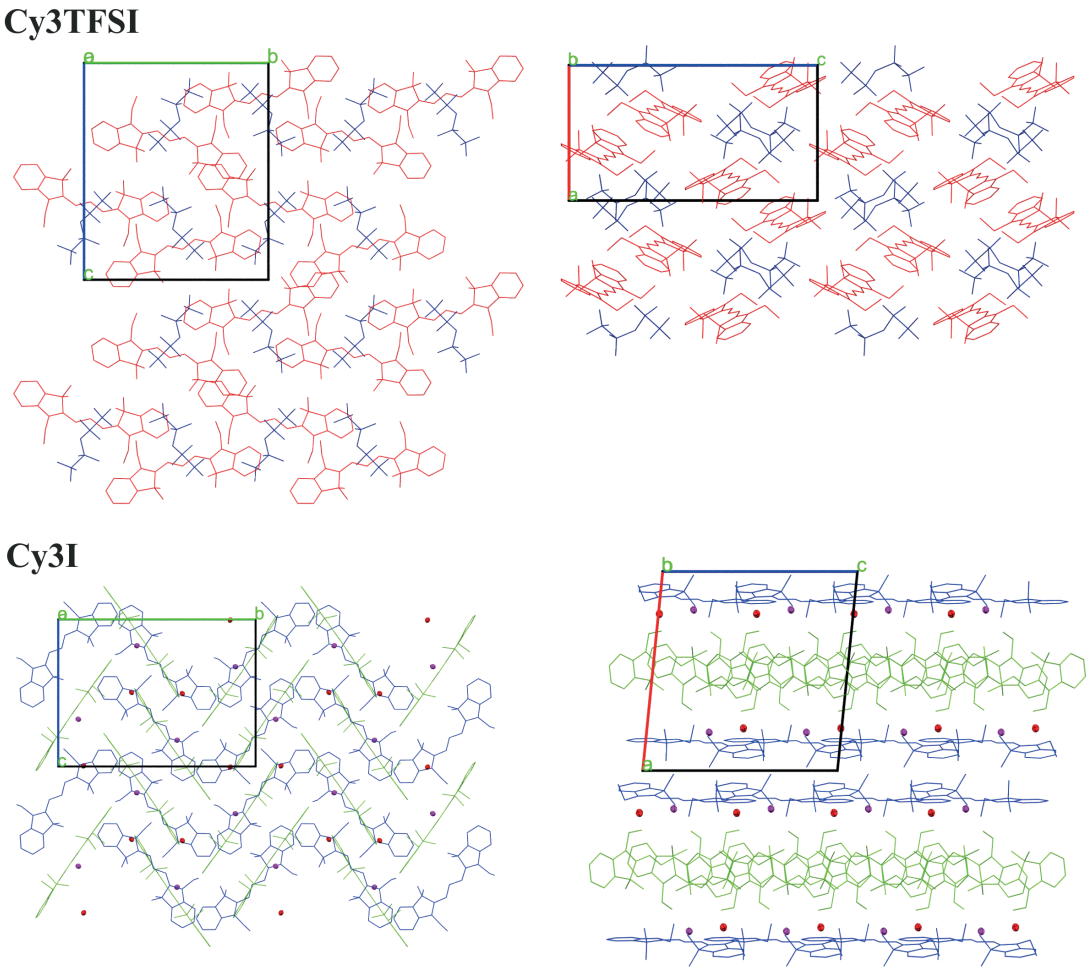

Figure 4:5 Molecular arrangement over 2x2x2 unit cells with views along the a axis (left) and b axis (right). For clarity the Cy3TFSI packing is depicted in the wire frame model, while Cy3I contains the chromophore in wire frame and the iodide as thermal ellipsoid with 50% probability level. The disorder in Cy3TFSI as well as the hydrogen atoms are omitted for clarity. Color code: Cy3TFSI symmetry equivalent chromophores: red, anion: blue. Cy3I symmetry equivalent chromophores: blue and green, iodide: red or purple.

On the contrary the chromophores in Cy3I are packed in two symmetry equivalents; see **Figure 4:5**: the blue layers are forming a plane that sandwiches the cross bone packed yellow symmetry equivalent layer. The iodide anions are closely distributed along the plane of blue chromophores pointing towards complex shared anion-cation interactions within the two symmetry operation separated layers as observed by the highly asymmetric iodide-chromophore coordination distance (**Figure 4:4**). Despite the well-ordered symmetry close π-stacking or long range heteroatom interactions are prevented, since the closest chromophore distances exceed 5 Å. The packing motives are in agreement with the 10°C difference in melting point between Cy3TFSI and Cy3I.

4.5.3 Substrate Dependent Thin Film Morphology

The concept of “physical vapour deposited cyanine organic electronics” was proven in devices with standard geometry containing hole transport layers such as MoO_3 or PEDOT:PSS as well as inverted geometry devices with compact and mesoporous TiO_2, using commercially available indium-tin-oxide (ITO) on glass as substrate. Thin film formation during vacuum deposition is mainly determined by the surface energy of the substrate, substrate temperature and the evaporation rate which allows the formulation of different growth mechanisms.[48] Depending on the substrate used, significantly different morphologies of the Cy3TFSI dye were obtained (**Figure 4:6**).

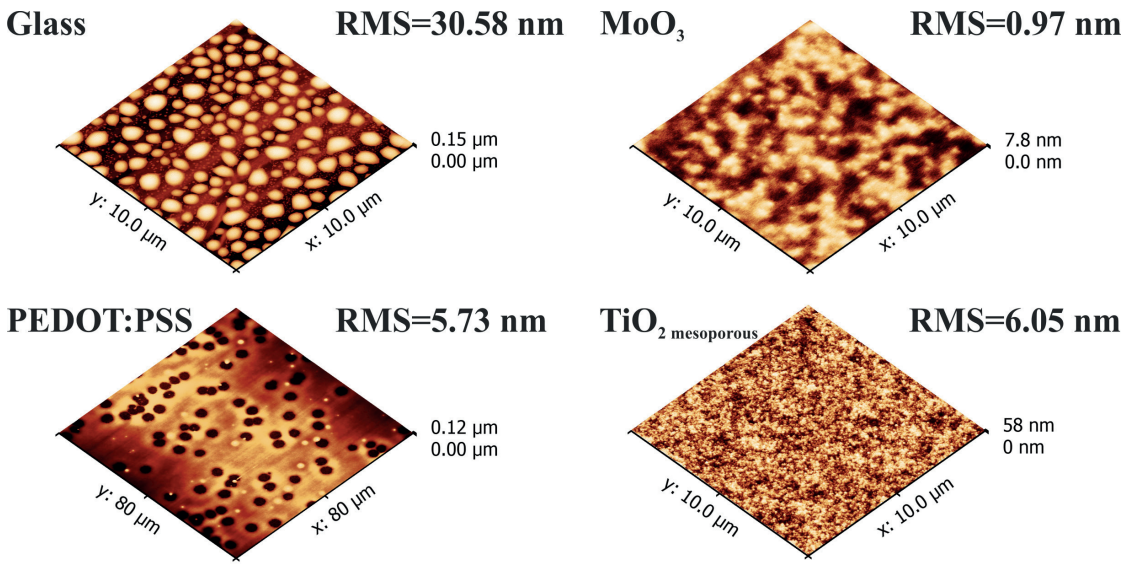

Figure 4:6 Topography of vacuum deposited Cy3TFSI films on different substrates.

The glass substrate leads to a formation of well isolated up to 2 micrometre sized islands of 70 nm height **(Figure S14).** It provides also the roughest surface of the investigated thin films, such droplet formation results from dewetting phenomena. MoO_3 provides a better surface energy match by firstly adsorbing a thin dye layer followed by an irregularly shaped micrometre sized island formation indicating a possible continuous film formation at higher thicknesses but with increased surface roughness comparable to a mechanism formulated by Stranski-Krastanov.[48] When PEDOT:PSS is employed, amorphous film with low overall surface roughness forms over areas of more than 10 μm^2. However, on a larger scale dewetting holes up to 6 μm in diameter (**Figure S14**) as well as local dye droplet formation on the amorphous bottom layer is observed, indicating an additional abrupt organic material erosion from the crucible. The high surface energy mismatch can be bypassed when naturally rough mesoporous TiO_2 with large surface volume is used. The atom force microscopy (AFM) scanned area reveals spherical particles smaller than 500 nm in diameter close to native mesoporous TiO_2 morphology suggesting a continuous dye coverage of the TiO_2 particles. Together with MoO_3 the investigated dye film on mesoporous TiO_2 provides the smallest surface roughness (**Figure S14**).

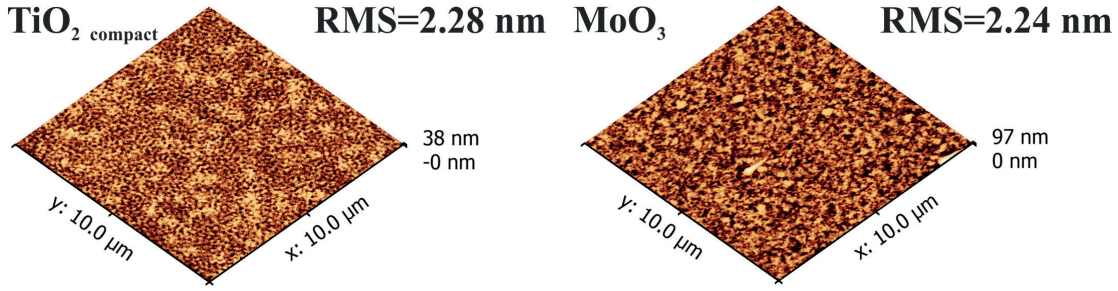

Figure 4:7 Topography of coevaporated Cy3TFSI and C_{60} on TiO_2 and MoO_3 substrates.

We can assume that the films formed after the melt based evaporation are amorphous in nature. In this sense our evaporation process is different from a sublimation process. Neither AFM nor UV-Vis spectroscopy point to the presence of crystalline domains.

We here also want to point to a drawback of films processed from solution. We had observed earlier that these films contain considerable amounts of residual solvents.[49] This leads to increased mobility of dye molecules and may account for the ability of the molecules in the film to crystallize over time. We also demonstrated that the solvent molecules have a significant influence on electronic processes at interfaces in solar cells.

Further trials to form a bulk heterojunction by coevaporation of Cy3TFSI and fullerene C_{60} blends on MoO_3 and compact TiO_2 substrates (**Figure 4:7**) have led to a better surface energy match. The surface roughness in the order of 2 nm in both blends is low and should allow applications in either standard or inverted geometry bulk heterojunction devices. The surface profile exhibits mixed random amorphous features suggesting suppressed phase separation below 1 µm in diameter. A spinodal pattern is recognisable on the TiO_2 substrate. However, local organic material accumulation ascending several nanometres from the surface can also be observed in both blends, mainly caused by an abrupt Cy3TFSI ejection from the crucible.

Solution processed blend films of cyanine dyes and fullerenes on the other hand frequently phase separate into large scale structures by liquid-liquid dewetting.[50] Here co-evaporating Cy3TFSI and a fullerene leads to a more favourable morphology for solar cell application than the spincoated samples (see section Device Fabrication).

In summary, wetting phenomena observed during spincasting from solution also apply to evaporated cyanine films making extended film tuning on different substrates an important issue. The substrate coverage can be improved by blending the Cy3TFSI or incorporating it as a dopant into a carrier matrix for OLED application overcoming the surface energy mismatch.

4.5.4 Proof of Concept in Organic Electronic Devices

The Cy3TFSI salt enables a wide variety of electronic device fabrication methods not seen in cyanine dye semiconductors so far. First proof-of-concept devices are presented with pro and contra regarding their further perspectives. With an open circuit voltage of 1 V, a solution based bilayer device of Cy3TFSI and C60 shows one of the highest potentials among all organic semiconductors (**Table S13**). One of the major existing limitations in cyanine dye semiconductors for organic photovoltaic applications was the so far only poorly performing bulk-heterojunction morphology.[51] By blending cyanine dyes with fullerene based electron acceptors in solution, typically micrometre sized phase separated domains of pure cyanine/fullerene rich phases form as demonstrated in Fig. S15. Such morphology leads to short circuited organic photovoltaic devices (**Table S14**). However our new approach of simultaneous dye/fullerene evaporation has led to the first vacuum processed cyanine dye based bulk heterojunction device.

Cy3TFSI was employed as electron donor material in a fully vacuum processed inverted geometry bulkheterojunction OPV device. In total 32 cells with 8 cells per substrate were prepared. 13 cells showed short circuit behaviour, therefore 19 cells could be measured. **Figure 4:8** represents the best performing device of the batch.

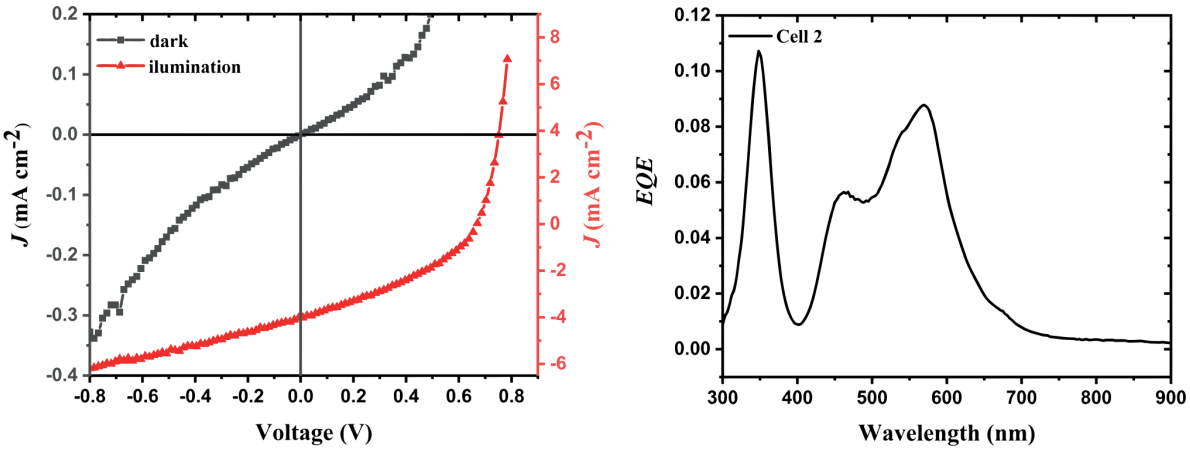

Figure 4:8 JV and EQE curves of the best performing OPV cell. The EQE represents a sharp C_{60} peak at shorter wavelengths followed by an overlap of the second C_{60} absorption peak with Cy3TFSI.

The OPV device exhibits a dark current of 0.34 mA cm^{-2} at -0.8 V. One origin of the dark current could be alternative pathways trough the thin active layer formed by a continuous electron acceptor channel ranging from the hole collecting layer to the TiO_2. This could partially explain the relative low fill factor (FF) of 41.5% and the open circuit voltage (V_{OC}) of 0.67 V in the device. The relatively low V_{OC} points also towards not optimal morphology of the active layer missing the well-defined phase separated networks between dye and electron acceptor in the order of 10-20 nm. The AFM analysis in **Figure 4:7** shows the absence of micrometre sized phase separated domains in freshly prepared blends, which typically would occur when cyanine dye fullerene blends are coated from solution.

However, a repeated measurement after 3 weeks of storage in the glovebox shows several micrometre sized dendritic crystals (**Figure S16**) pointing towards ongoing kinetic processes, driven by dye crystallization in the blend.

The Cy3TFSI proves itself as a strong absorber capable to generate sufficient amount of short circuit current density (J_{sc}) of 4.02 mA cm^{-2} since an active layer thickness of only 10 nm is used. The values are leading to a champion performance (η) of 0.96%. However, the experimentally obtained J_{SC} for the best device deviates does not match the calculated J_{SC} of 0.90 mA cm^{-2} from the external quantum efficiency (EQE) spectrum. This deviation originates mainly from differences in the two measurements and can only be compared when no light intensity related effects play a role. In fact, while the average V_{OC} of 0.63±0.06 V and FF of 38.98±2.41% are stable for all 19 cells, the J_{SC} of 1.46±0.98 mA cm^{-2} shows a large variation between minima and maxima. The J_{SC} calculated from the EQE spectrum matches the measured average value much better, pointing towards quick degradation mechanisms within the best cell. This effect also leads to a broad distribution in average device performance of 0.36±0.25%. The EQE data proves that both components of the blend, the Cy3TFSI and the C_{60}, contribute to the photovoltaic effect with an external quantum efficiency of 8%. The contribution of the dye to the external quantum efficiency, however, is less than that of C_{60} suggesting either an extraction barrier for holes formed at the heterojunction/MoO_3 surface or a partial chromophore degradation or is simply the result of the very thin active layer used. Further, the coevaporation of Cy3TFSI and C_{60} prevents aggregate formation of the cyanine dye since the peak/shoulder ratio of 1:0.55 is comparable to the one obtained from acetonitrile solution although the absorbance of C_{60} may overlap with the shoulder at shorter wavelengths of the Cy3TFSI.

Further vacuum processed devices should demonstrate the introduced flexibility by the Cy3TFSI in fabricating varying device stacks. The bilayer geometry cells realized by physical vapour deposition suffer from bad morphology of the neat evaporated films as discussed in Fig. 6. A further promising device stack is the inverted bilayer cell (**Figure S17, S18, S19, Table S14**). With a high V_{OC} in a range of 0.8 V, the inverted bilayer device approaches V_{OC} values also found in solution spin-casted bilayer reference device. The regular geometry bulk heterojunction device cannot compete with the implemented inverse structure. Further the solid state dye sensitized solar cell approach seems to be less promising from all trials.

4.6 Conclusion

By employing the bistriflylimide anion with a well dispersed negative charge over seven atoms to the 1-ethyl-2-[3-(1-ethyl-1,3-dihydro-3,3-dimethyl-2H-indol-2-ylidene)-1-propen-1-yl]-3,3-dimethyl-3H-indolium chromophore we introduce volatility and thermal stability to an organic salt of high molecular weight. Properties of the solid state structure from single crystals and thermo-analytical methods were linked to reveal the evaporation mechanism of the dye. The lattice energy and enthalpy of vaporization were identified to be the key parameters of the first volatile organic cyanine salt. We give evidence that a weakly coordinating anion tailored for a specific chromophore regarding the number of atoms for dispersed negative charge can introduce quasi gas phase conditions to the chromophore. The semiconducting properties of the cyanine allowed its application in organic electronic devices as light absorbing or emitting layer. Proof of concept was demonstrated by fabricating fully vacuum deposited OPV devices. This work aims to pave the way to development strategies of cyanine based volatile organic salts covering the full visible and infrared spectral absorption range.

4.7 Experimental Section

4.7.1 Materials and Methods

All chemicals and solvents were purchased from commercial sources (*Aldrich, VWR, FEW Chemicals, Kurt J. Lesker*) and used as received, unless otherwise stated. Reactions were carried out under air atmosphere using common lab glass ware. NMR multicore spectra were recorded on a *Bruker AV-400* spectrometer (^{1}H-NMR: 400 MHz, ^{13}C{^{1}H}-NMR: 100 MHz, ^{19}F{^{1}H}-NMR: 377 MHz). Chemical shifts (δ) are reported in ppm (parts per million) with the solvent residual signal (^{1}H/^{13}C{^{1}H}: 7.20/79 for $CDCl_3$) as reference. J coupling constants are given in Hz. Multiplicities are reported as singlet (s), doublet (d), triplet (t), quartet (q), multiplet (m). Elemental analysis data were obtained from the Micro Laboratory of ETH Zürich with the instrument *Leco TruSpec Micro* for C, H, N, S, F and O, while I was determined by ion chromatography. Thermal gravimetric analysis as well as differential scanning calorimetry were recorded on a *Netzsch TG 209 F1* and Netzsch STA449 F3 Jupiter, respectively.

4.7.2 Device Fabrication and Characterisation

Glass/ITO substrates were cleaned in acetone (*VWR*, 99.5% GPR RECTAPUR), isopropanol (*VWR*, EMPLURA), ethanol (*VWR*, 99.5% AnalaR NORMAPUR®) detergent (Hellmanex® III, 2 wt% water solution) and finally washed four times with deionised water. Subsequently a precursor sol yielding a 50 nm thick TiO_2 layer was spincasted according to a literature protocol.[52] The vacuum deposited bulkheterojunction was fabricated by adjusting a constant rate of 0.12 Å s^{-1} from the C_{60} source followed by evaporation of Cy3TFSI at 128 °C with a combined rate of 0.24 Å s^{-1}. Finally after stabilization of the deposition rate the substrate shutter was opened to deposit the bulkheterojunction layer by coevaporation. Evaporation of MoO_3 (99.97%) as the hole transport layer and silver (99.99%) as the top electrode followed immediately after with a deposition rate of 0.1 Å s^{-1}. The pressure in the evaporation chamber did not exceed $6x10^{-6}$ mbar during all evaporation steps. The OPV cell areas were defined as 3.1 and 7.1 mm^2 by using a mask for cathode deposition. Further details about device fabrication can be found in the supporting information. The solar cells were characterised under inert gas atmosphere on a calibrated solar simulator (Spectra Nova) using a Xe lamp with 100 mW cm^{-2} simulated AM1.5G solar irradiation. The light intensity was adjusted using a calibrated silicon reference cell from Rera Solutions. External quantum efficiency measurements were performed on a SpeQuest RR-2100.

4.7.3 Further Characterisation

UV-Vis spectra were measured on a Varian Cary 50. Measurement of *n* and *k* was performed using a spectroscopic ellipsometer M2000-VI (J.A. Woollam). The AFM analysis was performed on a scanning probe microscope Bruker Icon3 in tapping mode. Cyclic voltammetry (CV) measurements were performed on a PGStat 30 potentiostat (Autolab) using a three cell electrode system (Au working electrode, Pt counter electrode and an Ag/AgCl reference electrode). Single crystal diffraction patterns were recorded on a Stoe Mark II-Imaging Plate Diffractometer System (Stoe & Cie GmbH, Darmstadt, Germany) equipped with a graphite-monochromator. Data collection was performed at –100˚C using Mo-Kα radiation (λ = 0.71073 Å). The structures were solved by direct methods using the program SHELXS and refined by full matrix least squares on F^2 with SHELXL.[53] The hydrogen atoms were included in calculated positions and treated as riding atoms using SHELXL-97 default parameters.[54] All non-hydrogen atoms were refined anisotropically. All cartoons depicted in this work as well as chromophore-anion distances were prepared and measured using MERCURY CSD 3.9.[51] CCDC 1834037 and 1834038 contain the supplementary crystallographic data for for Cy3I and Cy3TFSI, respectively. These data can be obtained free of charge from the Cambridge Crystallographic Data Centre via www.ccdc.cam.ac.uk/data_request/cif. Detailed information about the background of the described experiments can be found in the supporting information.

4.8 Supporting Information

Supporting Information is available from the Wiley Online Library or from the author.

4.8.1 General Information

4.8.2 General Notation for this Work

- Two symmetrical indolenine derivatives connected with a trimethine chain

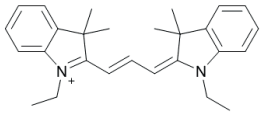

1-Ethyl-2-[3-(1-ethyl-1,3-dihydro-3,3-dimethyl-2*H*-indol-2-ylidene)-1-propen-1-yl]-3,3-dimethyl-3H-indolium (Cy3)

- Weakly coordinating anion

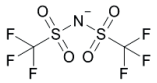

Bis((trifluoromethyl)sulfonyl)imide (TFSI)

- Abbreviation for the dye used in this work

Cy3TFSI

Figure S 2. Overview of the used notation of the compound for this work.

4.8.3 Anion Exchange Procedure

The detailed background and experimental setup for the ion exchange procedure can be found in literature.[1]

4.8.4 Synthesis of Cy3TFSI

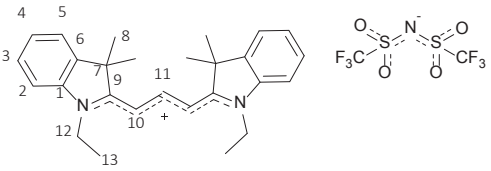

0.5 g of Cy3I solved in 250 mL MeCN were passed through 1.3 g of the anion exchange resin loaded with the bistriflylimide. After evaporation of the solvent and drying for 24 h at 9.3x10^{-3} mbar a shiny red solid was obtained. Yield: quantitative.

For X-Ray analysis suitable crystals were obtained by slowly cooling of a saturated ethanol solution.

[$C_{29}H_{33}F_6N_3O_4S_2$] 665.71 g mol^{-1}

^{1}H NMR (400 MHz, Chloroform-*d*) δ: 8.44 (t, *J* = 13.5 Hz, 1H, H(11)), 7.41 (td, *J* = 7.7, 1.2 Hz, 2H, H(3), 7.38 (d, *J* = 7.1 Hz, 2H, H(5), 7.27 (t, *J* = 7.5 Hz, 2H, H(4)), 7.14 (d, *J* = 7.9 Hz, 2H, H(2)), 6.53 (d, *J* = 13.4 Hz, 2H, H(10)), 4.20 (q, *J* = 7.3 Hz, 4H, H(12)), 1.73 (s, 12H, H(8)), 1.47 (t, *J* = 7.2 Hz, 6H, H(13) ppm.

^{13}C NMR (101 MHz, Chloroform-*d*) δ: 173.8 (C9), 150.9 (C11), 141.7 (C1), 140.8 (C6), 129.1 (C3), 125.7 (C4), 122.4 (C5), 120.1 (q, J = 321 Hz, (CF_3)), 110.9 (C2), 103.0 (C10), 49.4 (C7), 39.7 (C12), 28.1 (C8), 12.4 (C13) ppm.

^{19}F NMR (377 MHz, Chloroform-*d*) δ: -78.7 ppm.

Elemental analysis: Calculated: [C] 52.32, [H] 5.00, [N] 6.31, [F] 17.12 [S] 9.63.

Found: [C] 52.44, [H] 5.14, [N] 6.34, [F] 17.25 [S] 9.67.

4.8.5 Thin Film Evaporation

4.8.6 Qualitative trials of Cy3TFSI evaporation

Figure S 3. Visual results of the evaporated Cy3TFSI films on glass, ITO/TiO_2 ITO/MoO_3 and ITO/PEDOT:PSS substrates.

4.8.7 UV-Vis absorbance

To determine the molar extinction coefficient 1.44 x 10^{-4} mol L^{-1} acetonitrile stock solution of the Cy3TFSI compound was prepared. Subsequently solutions with five different concentrations were prepared by diluting the stock solution (**Table S1**).

Table S1. Used concentrations for the generation of calibration points in UV-Vis.

Solution	Concentration (mol L^{-1})
	Cy3TFSI
1	1.70 x 10^{-8}
2	6.35 x 10^{-8}
3	5.85 x 10^{-7}
4	6.85 x 10^{-7}
5	2.39 x 10^{-6}

All measurements were performed in a 1 cm quartz glass cuvette using 99.8 % acetonitrile as reference for the baseline. The relative molar extinction coefficient was calculated by extracting the slope of the resulting plot of concentration against absorbance intensity.

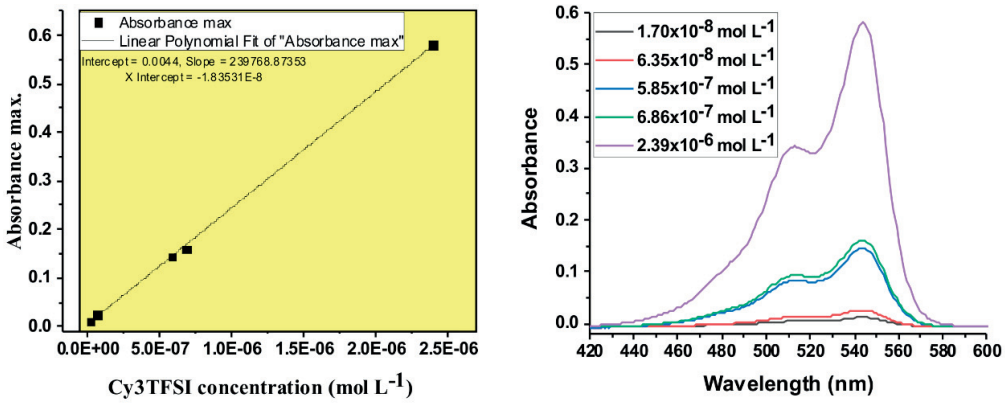

Figure S 4. Concentration dependent absorbance and linear fit of the absorbance maxima against concentration.

The extracted optical data are summarized in **Table S2**. The optical band gap was calculated from the onset of the absorbance at higher wavelengths with the following equation.

$$E_{g(opt)} = \frac{h \times c}{\lambda_{onset}}$$

λ_{onset}: Onset of absorption band at higher wavelength, h: Planck constant, c: speed of light.

The oscillator strength describes the probability of a transition from a lower to an upper energy state. The higher the value the easier the electrons can be excited and the stronger absorbing is the dye.

$$f = 4.319 \times 10^{-9} \int \varepsilon(\upsilon)\, d\upsilon$$

$\varepsilon(\upsilon)$: Molar extinction coefficient as a function of wavenumber, υ: Wavenumber.

The peak in **Figure S3** was assumed to represent the full band of the lowest energy π-π* transition and was integrated to calculate the oscillator strength.

First the wavelength was converted into wavenumbers with the following formula:

$$\upsilon = 1/(\lambda * 10^{-7})$$

Then the extinction coefficient was calculated for each wavenumber with the following formula:

$$\varepsilon_{(\upsilon)} = A/(c * d)$$

c: concentration in mol·L^{-1}, d: thickness of cuvette in cm, A: absorbance.

The calculations were performed for each recorded data point of the spectra.

Table S2. Calculated data from recorded UV-Vis spectra. * Onset energy at higher wavelengths obtained from MeCN solution.

Compound	ε_{max} (L mol^{-1} cm^{-1})	λ_{max} (nm)	λ_{onset} (nm)	$E_{(onset)}$* (eV)	f
Cy3TFSI	2.40 x10^5	544	565	2.19	1.87

4.8.8 Cyclic Voltammetry for Estimation of HOMO/LUMO Energy Levels

Cyclic voltammetry (CV) measurements were performed on a PGStat 30 potentiostat (Autolab) using a three cell electrode system (Au working electrode, Pt counter electrode and an Ag/AgCl reference electrode). Two electrolyte solutions of tetrabutylammonium perchlorate and tetrabutylammonium chloride were prepared in DMF each 0.1 mol/L. Each measurement needs 50 ml of tetrabutylammonium perchlorate (25 mL account for the measurement and 25 mL for cleaning) and 10 mL of tetrabutylammonium chloride (4 mL for measurement and 6 mL for cleaning) solutions. Following amount of the Cy3TFSI was used (**Table S3**).

Table S3. Weighted quantities of the dyes.

Dye	m (mg)	n (mol)
Cy3TFSI	10.0	1.50x10^{-5}

The Ferrocene solution was prepared qualitatively by adding a spatula of ferrocene in 10 mL of electrolyte solution. All potentials were referenced to NHE by adopting a potential of +0.72 V vs. NHE for Fc/Fc+ in DMF.[4] The rotating disk was equilibrated before first measurement for 30 min at 3000 rpm. Then the rotation speed was reduced to 50 rpm and was kept constant for all measurements. Before each measurement step the solution was fumigated with argon for 15 min. The solvent window was determined by running 30 cycles from -1.5 V until 1.5 V with a scanning rate of 2 V/s, subsequently the scanning rate was reduced to 0.1 V/s and the baseline curve was recorded. Then the Cy3TFSI was added to the solution and the above described measurement procedure was repeated. The negative potential window was adjusted to -0.75 V.

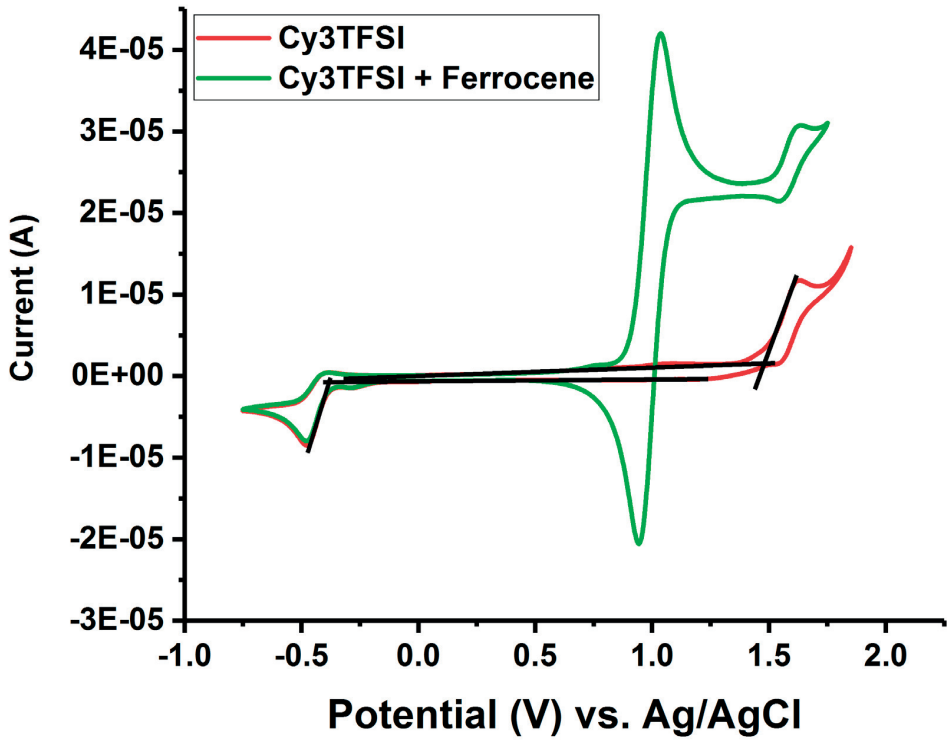

Figure S 4. Cyclic voltammetry curves of Cy3TFSI.

The calculations of the $E_{g(el)}$ (HOMO/LUMO gap) are based on the assumption that a positive cathodic current can be referred to a reduction process, while a negative anodic current to an oxidation process. Therefore the oxidation potential corresponds to electron extraction from the HOMO level, while the reduction potential is associated with the electron affinity and indicates the LUMO level. By analysing the recorded spectra graphically it is possible to determine the respective reduction $E_{red(dye)}^{onset}$ or oxidation $E_{ox(dye)}^{onset}$ onset potentials. It is notable that the recorded cyclic voltammograms are showing irreversible processes for all investigated dyes, so that the intersection onset of the corresponding peak has to be chosen as the respective potential. While for the ferrocene which undergoes a reversible process the potential is calculated according to:

$$E_{1/2(Ferrocene)}^{ox} = \frac{E_{pc}^{ox} + E_{pa}^{ox}}{2}$$

$E_{1/2(Ferrocene)}^{ox}$: half-curve potential, E_{pa}^{ox}: anodic peak potential, E_{pc}^{ox} : cathodic peak potential.

The potentials were measured against an Ag/AgCl reference. The used conversion constant for ferrocene in DMF is 0.72 V.[4] The correction value against NHE for ferrocene was calculated as follows:

$Korr._{Ferrocene}$=0.72-$E_{1/2(Ferrocene)}^{ox}$

To calculate the corrected values for the onset potentials against NHE potential the following assumptions were made:

$$E_{ox(dye)\ vs.\ NHE}^{onset} = E_{ox(dye)}^{onset} + Korr._{Ferrocene}$$

$$E_{red(dye)\ vs.\ NHE}^{onset} = E_{red(dye)}^{onset} + Korr._{Ferrocene}$$

The calculation of the HOMO and LUMO was performed by using empirical equations.[5] The used onset potentials were corrected against NHE as described above.

$$E_{HOMO} = -\left(E_{ox(dye)\ vs.\ NHE}^{onset} + 4.5\right)eV$$

$$E_{LUMO} = -\left(E_{red(dye)\ vs.\ NHE}^{onset} + 4.5\right)eV$$

$$E_{g(el)} = E_{HOMO} - E_{LUMO}$$

Table S4. Calculated data from the CV measurement.

Substance	$E_{ox(dye)}^{onset}$ /V	$E_{red(dye)}^{onset}$/V	$E_{\frac{1}{2}ox(FeCp_2)}^{0}$/V	E_{HOMO}/eV	E_{LUMO}/eV	$E_{g(el)}$/eV
Cy3TFSI	1.48	-0.38	0.99	-5.71	-3.85	1.86

4.8.9 Thermal Behaviour of Cy3I and Cy3TFSI

The dynamic TGA for both materials was carried out with a heating cycle from room temperature till 600°C followed by a cooling to room temperature with dynamic steps of 10°C min^{-1}.

The aluminium crucible was sealed and contained five holes in the lid.

Temperature Program for isothermal TGA measurement for both components:

All dynamic steps were carried at 10°C min^{-1} under constant nitrogen or helium flow respectively.

Dynamic: heating to 100°C; Isothermal: 100°C, 30 min; Dynamic: heating to 200°C; Isothermal: 200°C, 30 min; Dynamic: heating to 220°C; Isothermal: 220°C, 30 min; Dynamic: 230 °C; Isothermal: 230°C, 30 min; Dynamic: heating to 240°C; Isothermal: 240°C, 30 min; Dynamic: heating to 250°C; Isothermal: 250°C, 30 min; Dynamic: heating to 260°C; Isothermal: 260°C, 30 min; Dynamic: heating to 270°C; Isothermal: 270°C, 30 min; Dynamic: heating to 280°C; Isothermal: 280°C, 30 min; Cooling to room temperature.

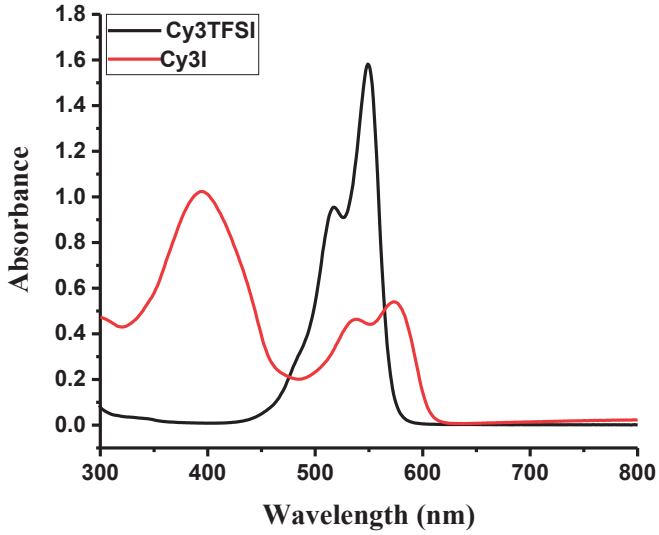

Figure S 5. Qualitative UV-Vis spectra in ethanol solution rinsed from the substrate of evaporated starting material (Cy3I) and Cy3TFSI.

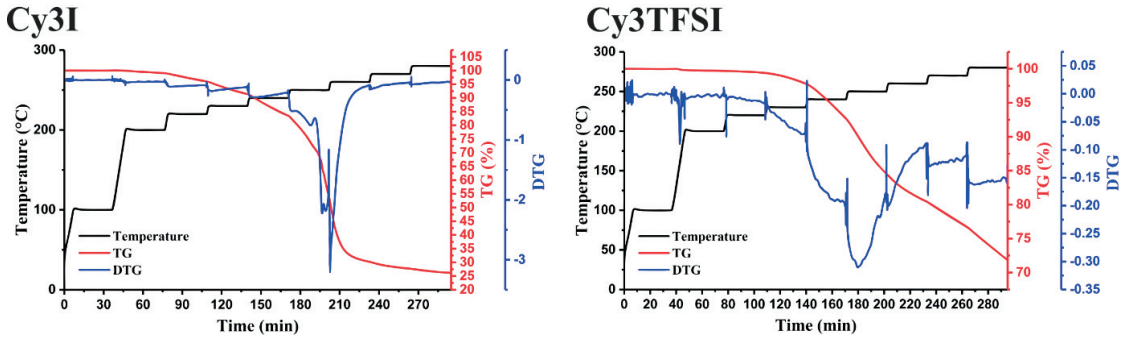

Figure S 5. Isothermal TGA of both components with relative mass loss.

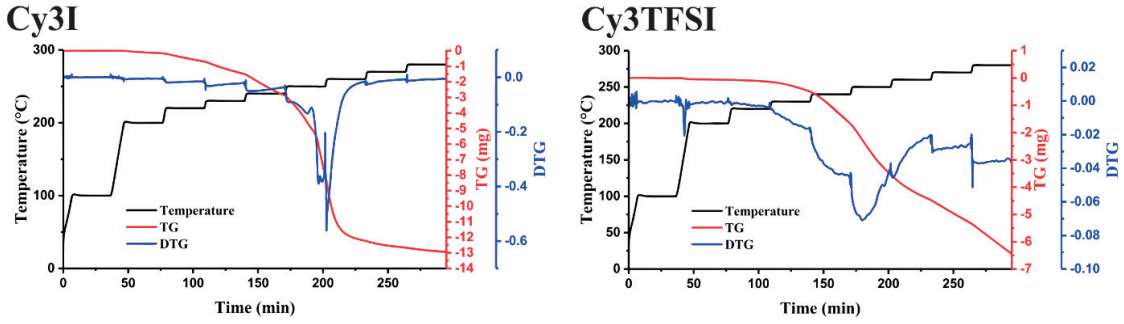

Figure S 6. Isothermal TGA of both components with absolute mass loss.

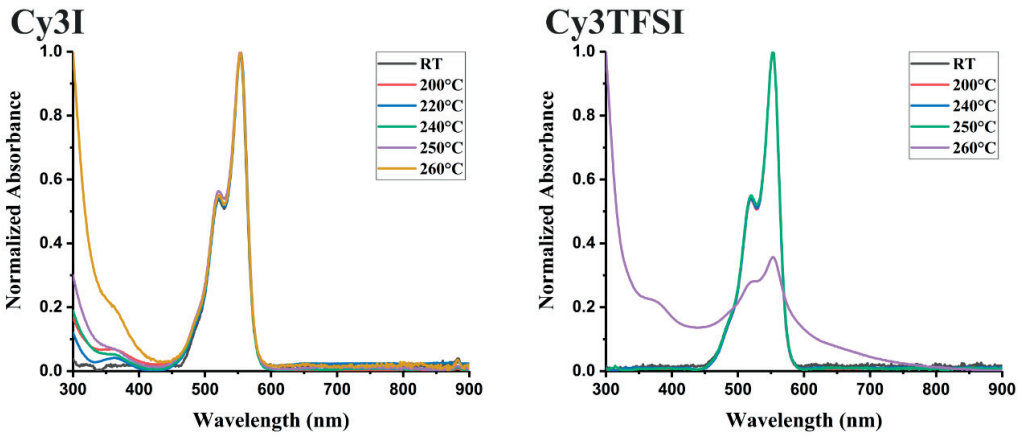

Figure S 7. Normalized UV-Vis spectra of heated residual material from TGA crucibles at certain temperatures.

The mass loss of each isothermal section was extracted and plotted against the time of each isothermal step. Subsequently the slopes of the linear fit were extracted and plotted against temperature.

Table S5. Cy3I extracted slope of (dm/dt) vs. t and coefficient of determination at a certain temperature.

T/°C	Slope	R^2
200	0.0052	0.99
220	0.01701	0.99
230	0.0263	0.99
240	0.04573	0.99
250	0.14865	0.92
260	0.09757	0.77
270	0.01349	0.97
280	0.00851	0.98

Table S6. Cy3TFSI extracted slope of (dm/dt) vs. t and coefficient of determination at a certain temperature.

T/°C	Slope	R^2
200	0.00083	0.97
220	0.00232	0.98
230	0.01196	0.99

T/°C	Slope	R^2
240	0.03963	0.99
250	0.06227	0.99
260	0.02901	0.99
270	0.02770	0.99
28	0.03601	0.99

Table S7. Calculated values for Cy3TFSI in 220-250°C range to determine the enthalpy of vaporization.

T/K	T^{-1}/K^{-1}	10^5 (-dm/dt)/g min^{-1}	ln[$T^{1/2}$ (-dm/dt)]
493.15	0.00203	1.70	-7.8813
503.15	0.00199	2.63	-7.4355
513.15	0.00195	4.57	-6.87247
523.15	0.00191	1.49	-5.68398
slope	-18379.8		
R^2	0.94		

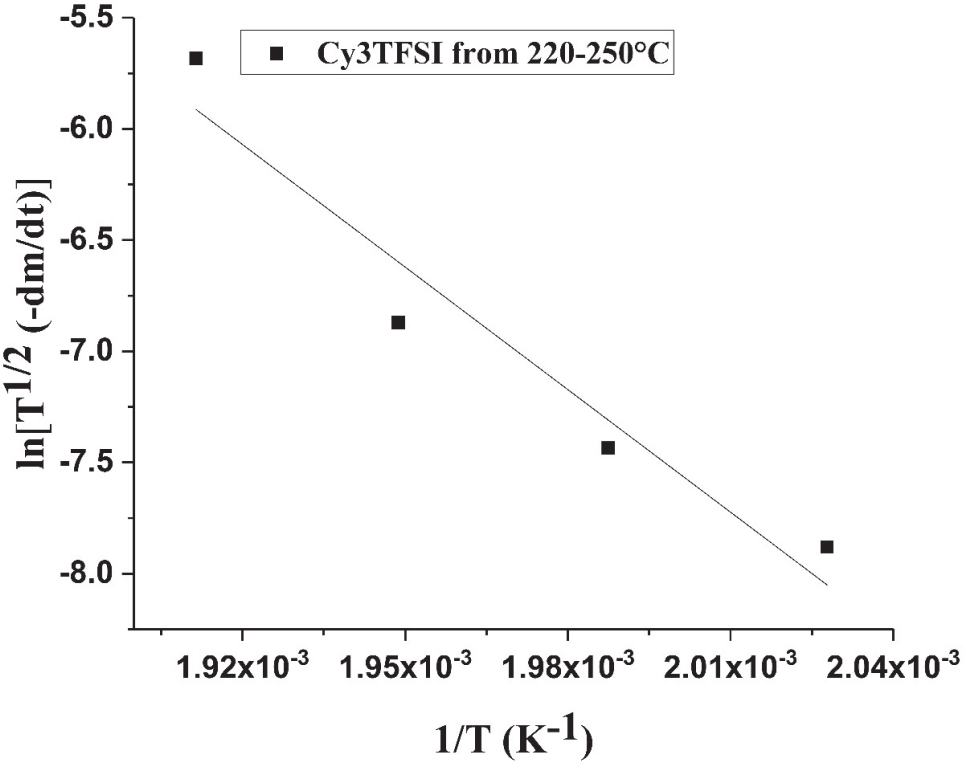

Figure S 98. Plot of $\ln[T^{1/2}\,(-dm/dt)]$ vs. T^{-1} to extract the slope for enthalpy of vaporization calculation.

Equation used to calculate the enthalpy of vaporization at average temperature (220-250°C):

$$\Delta_1^g H_m^\circ(T_{av}) = R\,S_L$$

R: universal gas constant 8.314 (J mol^{-1} K^{-1}), S_L: slope of $\ln[T^{1/2}\,(-dm/dt)]$ vs. T^{-1} (K^{-1}).

4.8.10 Crystal Structures

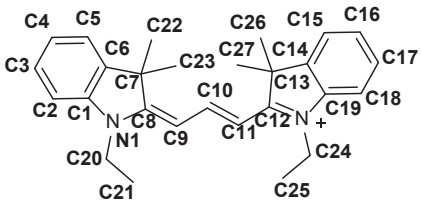

Figure S 10. Cyanine atom numbering.

All crystal structures solutions and refinements were performed with common crystallographic software.[2,3]

The cyanines were numbered according to the cif file.

Overview about possible ways to access parameters describing anion-cation interactions in a single crystal

Formula used to calculate the lattice energy:

Since the anions and cations are complex molecules build from several atoms the term cation/anion radii needs further specifications and assumptions. Additionally the positive and negative charges are delocalised over several atoms. Therefore the coordination distance determination between the cation and anion is not a trivial task.

One common disadvantage of usually used methods is that the ions are treated as spherical objects. This assumption causes strong deviations from real situation where the ions represent several covalent bound atoms of irregular shape.

A simple and reliable model was developed for complex molecular ions which translates the ionic radii into a molecular volume.[2] The molecular volume can be precisely calculated for any geometrical shape taking information from the X-Ray structural data.

$$\Delta U = |Z^+||Z^-|v\left(\frac{a}{V_m{}^{\frac{1}{3}}} + \beta\right)$$

ΔU = Lattice energy, $|Z^+||Z^-|$ = charge of cation/anion, v = number of ions per molecule, V_m = molecular volume, a = slope of the regression line: 117.3 kJ mol^{-1} nm (molecular volume against lattice energy of literature known salts), β = intercept of the regression line: 51.9 kJ mol^{-1} (molecular volume against lattice energy of literature known salts).

Table S8. Lattice energy calculation for Cy3TFSI and Cy3I.

Parameters	**Compound**	
	Cy3TFSI	Cy3I
a/nm (°)	1.02584 (90)	1.59149 (90)
b/nm (°)	1.60405 (90)	2.06750 (95.735)
c/nm (°)	1.88625 (90)	1.54852 (90)
Z	4	8
I	1	1
V_m/nm^{-3}	0.77596	0.63372
E_L/kJ mol^{-1}	359.09	376.93

Overview about possible determination of coulomb and lattice energy from single crystals:

Formula used to calculate Electrostatic interactions by Coulomb:

$$E_{Coulomb} = \frac{1}{4\pi\varepsilon\varepsilon_0} \cdot \frac{z^2e^2}{r}$$

Z = ionic charge, r = shortest contact distance between cation and anion, ε_0 = vacuum permittivity, ε = relative permitivity of the material.

Since the original formula of coulomb estimates spherical anions and cations the shortest cation-anion contact distance variable leads to a strong deviation from real conditions in complex molecular organic ions. The cation-anion distance can be replaced by the molecular volume.

$$r = \left(\frac{V_m}{2I}\right)^{\frac{1}{3}}$$

This modification provides more realistic values for complex molecular ions.

Table S9. Coulomb energy calculation.

Parameters	Compound	
	Cy3TFSI	Cy3I
ε	2.96	2.96
ε_0/ F m^{-1}	8.854*10^{-12}	8.854*10^{-12}
z	1	1
e/C	1.602*10^{-19}	1.602*10^{-19}
r/nm	0.729	0.63
E_c/eV	0.67	0.77

Similar to the lattice energy calculation the coulomb interactions should be taken as a qualitative physical description rather than absolute expression.

Table S10. Anion influence on bond lengths (Å) of the chromophore polymethine chain. *Average of the difference between C-C bond lengths in the polymethine chain. The values for Cy3I are given for both chromophores of the asymmetric unit.

Atom		
	TFSI	I
N1-C1	1.423(6)	1.413(4)/1.419(4)
N1-C8	1.360(5)	1.344(4)/1.342(4)
C8-C9	1.385(3)	1.385(4)/1.388(4)
C9-C10	1.386(3)	1.385(4)/1.378(4)
C10-C11	1.394(3)	1.385(4)/1.392(5)
C11-C12	1.380(3)	1.373(4)/1.379(4)
C12-N2	1.351(3)	1.351(4)/1.352(4)
N2-C19	1.408(3)	1.387(4)/1.412(4)
BLA*	0.77	0.43/1.23

Table S11. Anion influence on bending of the chromophore skeleton and indolenium ring conformation measured with Mercury 3.8.

Atoms		
	TFSI	**I**
C11-C12-N2-C19	174.1(9)	178.8(3)/178.1(5)
C11-C12-C13-C14	175.2(1)	177.4(5)/175.6(9)
C1-N1-C8-C9	172.2(3)	177.1(4)/178.9(1)
C6-C7-C8-C9	177.6(7)	177.0(2)/179.7(6)
C8-C9-C10-C11	177.0(4)	176.4(4)/178.1(1)

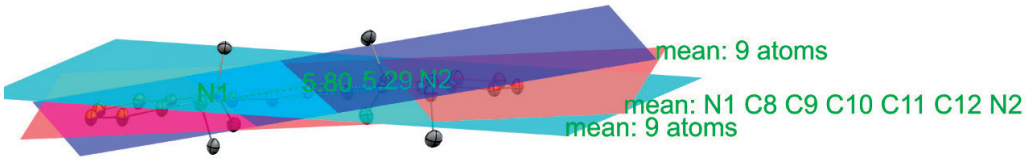

Figure S 11. Chromophore bending angle measurement example.

With a low bond length alternation of 0.77 pm the Cy3TFSI polymethine chain polarisation lays in-between 0.43/1.23 pm observed for both chromophores of Cy3I. The delocalised π electron system is terminated by the two indolenium nitrogen atoms. Both chromophores are slightly concave bended with additional geometrical distortions of the indolenium rings with torsion angles obtained from C1/19-N1/2-C8/12-C9/11 and C6/14-C7/13-C8/12-C9/11 ranging between 174-177° for Cy3TFSI and 175-179° for Cy3I respectively.

4.8.11 Relative Permittivity

$$\varepsilon_r = n^2 - k^2$$

ε_r: relative permittivity (dielectric constant or function), n: real part of the index of refraction, k. imaginary part of the index (extinction coefficient)

The orientational polarization or dipole polarisation appears at low frequencies around 10^4 Hz. The n and k values are dependent on the wavelengths. At higher wavelengths however the slope is very low and at a certain wavelength the k value becomes 0.

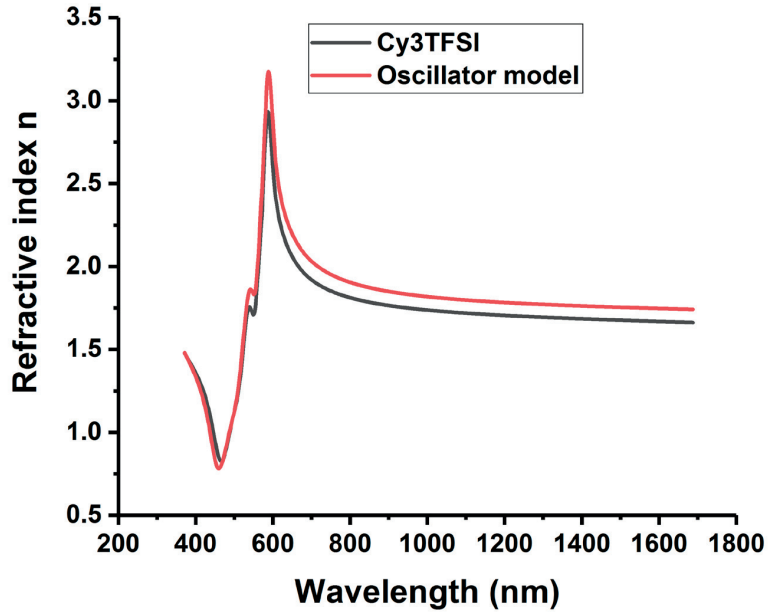

Figure S 9. Function of n depending on the wavelength.

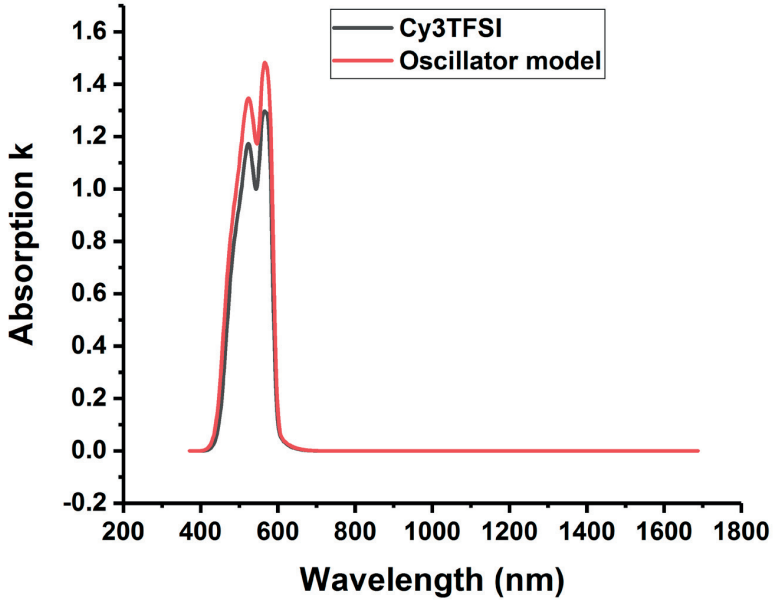

Figure S 10. Function of k depending on the wavelength.

Therefore this area was chosen for the calculation of the dielectric constant. The n are given in this table as averaged values over the selected wavelength region.

Table S12. Calculated relative permittivity values for the Cy3TFSI.

Cyanine	n	λ/nm	ε_r
Cy3TFSI	1.72	823-1688	2.96

4.8.12 Thin Film Morphology

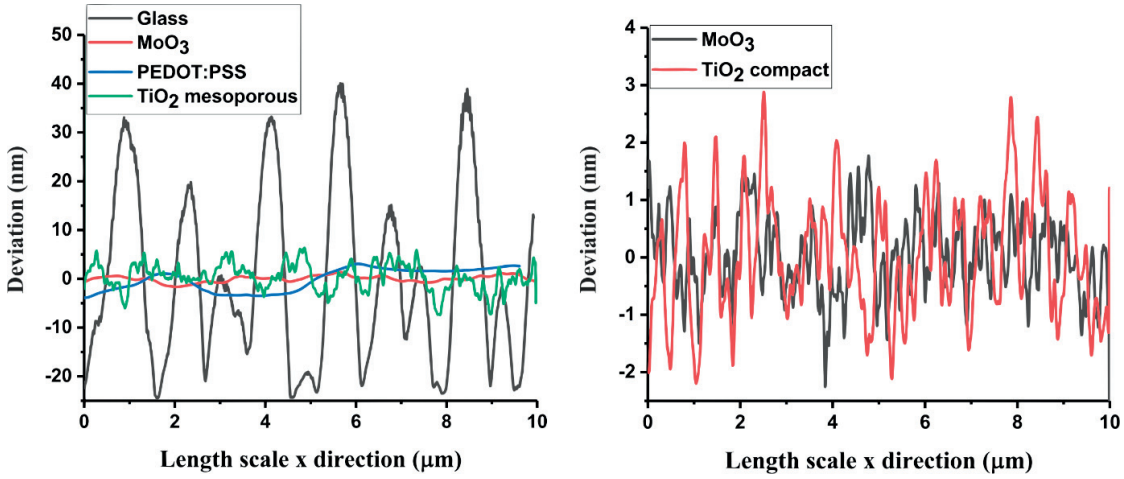

Figure S 14. Roughness profiles obtained from different substrates of thin evaporated Cy3TFSI films.

4.8.13 Organic Photovoltaic Device Fabrication

Solution Spin-casted Bilayer Reference Device

As for cyanine organic photovoltaic devices usual a bilayer stack was used with ITO/MoO_3(10 nm)/Cy3TFSI (10 nm)/C_{60} (40 nm)/Alq_3 (2 nm)/Ag (60 nm). The spincasting of the dye was performed under nitrogen atmosphere from TFP solution at 400 rpm for 60 s. After spincasting the substrate underwent a high vacuum treatment for 8 h at 6 x 10^{-6} mbar before the residual layers were evaporated. The statistics are presented in the Table S 13.

Table S13. Statistics of solution spincasted Cy3TFSI cells

	N Cells	Mean	Standard Deviation	Min.	Median	Max.
V_{OC}/V	8	0.97	0.07	0.81	1.00	1.01
J_{SC}/mA cm^{-2}	8	4.67	0.26	4.40	4.62	5.12
Eff %	8	2.25	0.22	1.93	2.21	2.55
FF %	8	49.48	0.95	47.87	49.92	50.33

Solution Spin-casted Bulk Heterojunction Device

The trial to spin-cast Cy3TFSI and PCBM from chlorobenzene solution on a MoO_3 surface to form a bulk heterojunction morephology yielded phase separated dye/fullerene rich domains as illustrated in Figure S15.

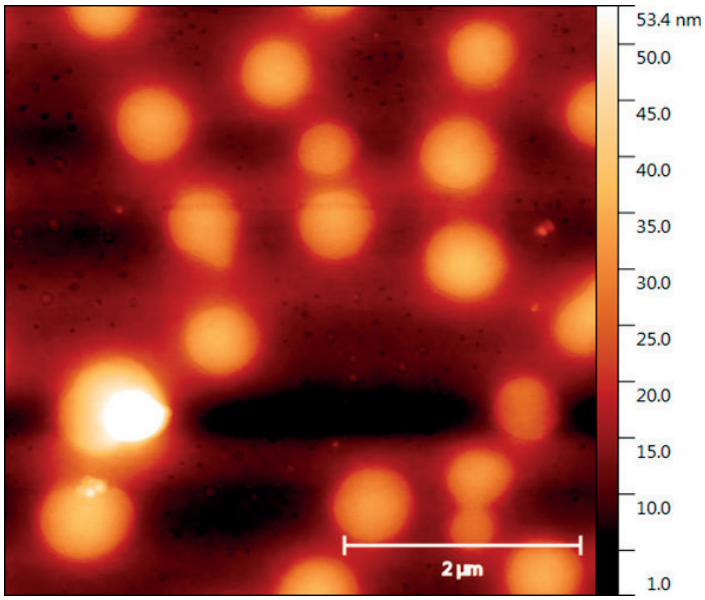

Figure S15. Morphology of spincasted Cy3TFSI and PCBM blend.

As can be seen from the Table 3 spin-casted bulk heterojunction device shows only short circuited cells producing nonsense statistical values. The morphology of the active layer causing these short circuited cells can be seen in the Table S14.

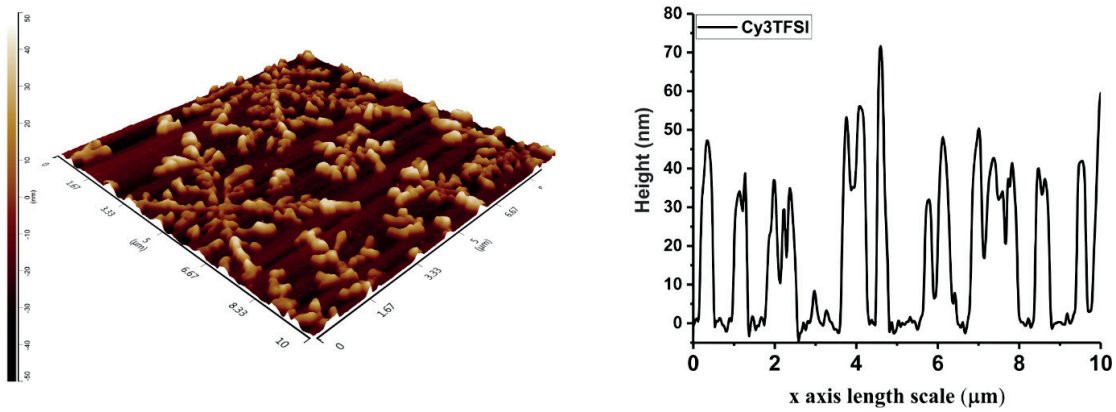

Figure S16. Topography of the coevaporated Cy3TFSI/C_{60} blend after 3 weeks storage in a glovebox.

Table S14. Statistical values of the short circuited Cy3TFSI/PCBM cells.

	N Cells	Mean	Standard Deviation	Min.	Median	Max.
V_{OC}/V	9	-1.29E9	1.73E8	-1.55E9	-1.28E9	-1.03E9
J_{SC}/mA cm^{-2}	9	-1205.3	722.75	-2221.05	-1445.34	-452.92
Eff %	9	2.22E-4	1.54E-5	2.01E-4	2.21E-4	2.45E-4
FF %	9	0.42	0.27	0.15	0.46	0.872

Co-evaporated Bulk-Heterojunction Device

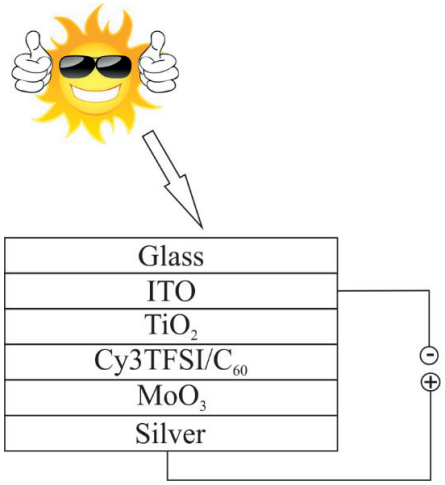

Figure S17. Architecture of the inverted bulkheterojunction cell.

The devices were made out of six layers: glass, indium tin oxide, TiO_2 (50 nm), Cy3TFSI/C_{60} active layer as co-evaporated bulkheterojunction (10 nm), molybdenum oxide (10 nm) as hole transport layer and silver (60 nm) as bottom electrode.

Table S15. Descriptive statistics of the measured Cy3TFSI cells.

	N	$\bar{x}_{arithm}$	s	Σ	min	$\bar{x}_{med}$	max
V_{OC}/V	19	0.63007	0.06067	11.97138	0.38763	0.64241	0.66975
J_{SC}/mA cm^{-2}	19	1.46121	0.97978	27.76305	0.71976	1.03648	4.02068
η	19	0.36075	0.24836	6.85428	0.15233	0.24708	0.9573
FF	19	38.97636	2.41159	740.55075	30.91617	39.47854	41.52454

Further Evaporated Device Stacks: First Trials

The following devices have been fabricated without further optimizing the interlayer or active layer thicknesses.

Bulk heterojunction regular:

Glass/ITO/MoO_3/(Cy3TFSI/C_{60})BHJ co-evaporation/Alq_3/Ag (blue curve)

Bilayer inverted:

Glass/ITO/$TiO_{2\ compact}$/C_{60}/Cy3TFSI/MoO_3/Ag (green curve)

SSDSSC:

Glass/ITO/$TiO_{2\ mesoporous}$/Cy3TFSI/CuI/Ag (violet curve)

Bilayer regular:

Glass/ITO/PEDOT:PSS/Cy3TFSI/C_{60}/Alq_3/Ag (red curve)

Glass/ITO/MoO_3/Cy3TFSI/C_{60}/Alq_3/Ag (black curve)

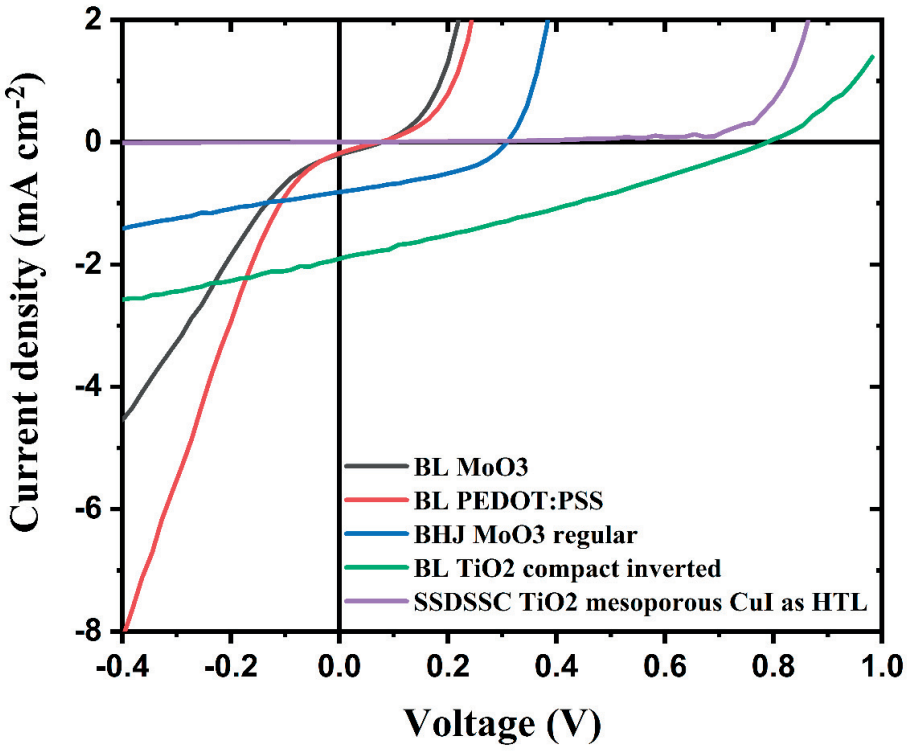

Figure S98. Sumarized results from different device stacks of evaporated Cy3TFSI. The curves represent the cell response under illumination.

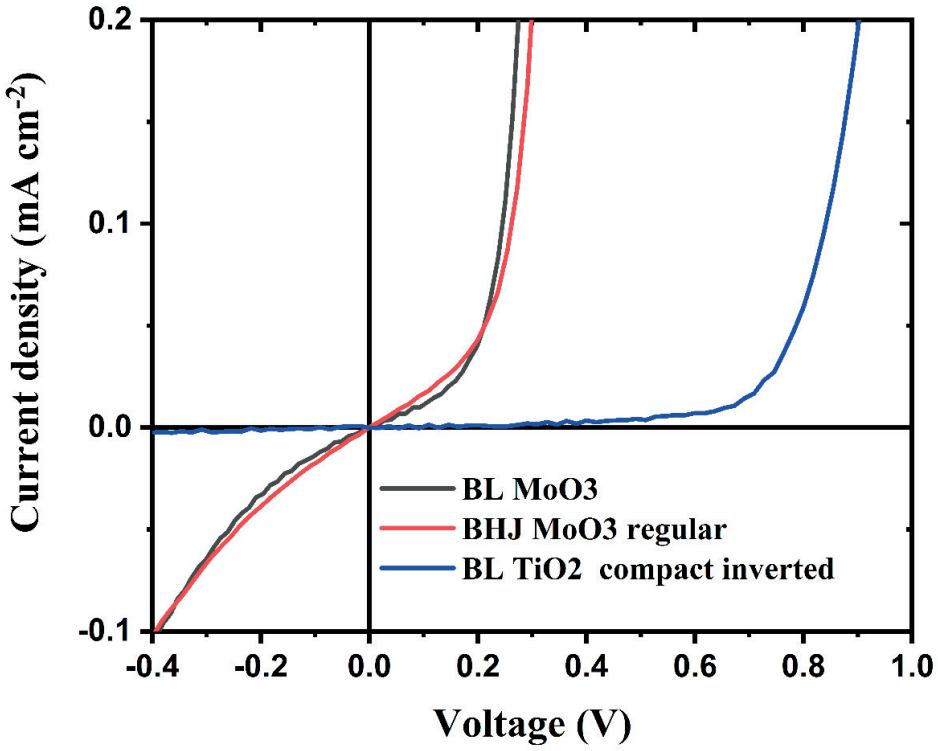

Figure S19. Dark current of the regular bulk heterojunction device, regular bilayer device geometry and of the inverted bilayer device geometry. Dark current of regular bilayer device with PEDOT:PSS as hole transport layer and SSDSSC devices were not measured due to the short lifetime of the cells.

Table S14. JV data of the representative evaporated Cells from Figure S17.

	V_{OC}/V	J_{SC}/mA cm^{-2}	η	*FF*
BL MoO_3	0.06	0.23	2.44x10^{-3}	17.07
BL PEDOT:PSS	0.06	0.24	1.4x10^{-3}	9.45
BHJ MoO_3 regular	0.30	1.12	0.10	45.11
BL TiO_2 compact inverted	0.77	1.89	0.42	29.01
SSDSSC TiO_2 mesoporous CuI as HTL	-0.05	-0.00	0	0

4.8.14 Sort Circuit Current Density Calculation

The short circuit current density $J_{sc} = \int EQE(\lambda) * \Phi_{AM1.5}(\lambda) \cdot e \, d\lambda$ was obtained by integrating over $EQE(\lambda)$, the photon flux $\Phi_{AM1.5}(\lambda)$ of the AM1.5 solar spectrum and multiplying by the elementary charge e.

4.8.15 Literature Supporting Information

[1] D. Gesevičius, A. Neels, S. Jenatsch, E. Hack, L. Viani, S. Athanasopoulos, F. Nüesch, J. Heier, Adv. Sci. 2017, 1700496, 1700496.

[2] H. D. B. Jenkins, H. K. Roobottom, J. Passmore, L. Glasser, Inorg. Chem. 1999, 38, 3609.

[3] Spek, A. L. (2003). J.Appl.Cryst. 36, 7-13.

[4] C. G. Zoski, *Handbook of electrochemistry*; Elsevier, 2007.

[5] J. L. Bredas, R. Silbey, D. S. Boudreaux, R. R. Chance, *J. Am. Chem. Soc.* **1983**, *105*, 6555.

4.9 Acknowledgements

The use of the Scanning Probe Microscopy User Laboratory at Empa is gratefully acknowledged. We thank the Swiss National Science Foundation for financial support under grant numbers 160116 and 152909.

4.10 References

[1] N. Karl, *Mol. Cryst. Liq. Cryst. Inc. Nonlinear Opt.* **1989**, *171*, 31.

[2] S. R. Forrest, *IEEE J. Sel. Top. Quantum Electron.* **2000**, *6*, 1072.

[3] D. Angmo, T. T. Larsen-Olsen, M. Jørgensen, R. R. Søndergaard, F. C. Krebs, *Adv. Energy Mater.* **2013**, *3*, 172.

[4] M. Hösel, D. Angmo, R. R. Søndergaard, G. A. dos Reis Benatto, J. E. Carlé, M. Jørgensen, F. C. Krebs, *Adv. Sci.* **2014**, *1*, 1400002.

[5] R. R. Søndergaard, M. Hösel, F. C. Krebs, *J. Polym. Sci. Part B Polym. Phys.* **2013**, *51*, 16.

[6] F. C. Krebs, *Sol. Energy Mater. Sol. Cells* **2009**, *93*, 394.

[7] H. Youn, H. J. Park, L. J. Guo, *Small* **2015**, *11*, 2228.

[8] N. T. Kalyani, S. J. Dhoble, *Renew. Sustain. Energy Rev.* **2012**, *16*, 2696.

[9] K. Norrman, A. Ghanbari-Siahkali, N. B. Larsen, *Annu. Reports Sect. "C" (Physical Chem.* **2005**, *101*, 174.

[10] D. M. Taylor, *Semicond. Sci. Technol.* **2015**, *30*, 1.

[11] H. Sasabe, J. Kido, *Chem. Mater.* **2011**, *23*, 621.

[12] F. So, J. Kido, P. Burrows, *Mrs Bull.* **2008**, *33*, 663.

[13] C. D. Dimitrakopoulos, P. R. L. Malenfant, *Adv. Mater.* **2002**, *14*, 99.

[14] M. A. Baldo, D. F. O'Brien, Y. You, A. Shoustikov, S. Sibley, M. E. Thompson, S. R. Forrest, *Nature* **1998**, *395*, 151.

[15] M. a Baldo, S. Lamansky, P. E. Burrows, M. E. Thompson, S. R. Forrest, *Appl. Phys. Lett.* **1999**, *75*, 4.

[16] J. Roncali, P. Leriche, P. Blanchard, *Adv. Mater.* **2014**, *26*, 3821.

[17] D. Saccone, S. Galliano, N. Barbero, P. Quagliotto, G. Viscardi, C. Barolo, *European J. Org. Chem.* **2016**, *2016*, 2244.

[18] J. L. Bricks, A. D. Kachkovskii, Y. L. Slominskii, A. O. Gerasov, S. V Popov, *Dye. Pigment.* **2015**, *121*, 238.

[19] V. Z. Shirinian, A. A. Shimkin, In *Heterocyclic Polymethine Dyes*; Strekowski, L., Ed.; Springer Berlin Heidelberg: Berlin, Heidelberg, 2008; pp. 75–105.

[20] C. H. G. Williams, *Trans. Roy. Soc. Edinburgh* **1856**, *21*, 377.

[21] K. Y.-J. Liao; Wen-Yih, Huang; Chien-Liang, Huang; Der-Ray, Chiang; Don-You, Hu; Andrew Teh, Lee; Hong-Ji, Ye; Shi-jae, Preparation of cyanine dye for high density optical recording disk **1999**.

[22] H. Tian, F. Meng, In *Functional Dyes*; Kim, S.-H., Ed.; Elsevier: Amsterdam, 2006; pp. 47–84.

[23] J. Tan, D. Ma, X. Sun, S. Feng, C. Zhang, *Dalton Trans.* **2013**, *42*, 4337.

[24] H. Mustroph, M. Stollenwerk, V. Bressau, *Angew. Chemie - Int. Ed.* **2006**, *45*, 2016.

[25] C. Shi, J. B. Wu, D. Pan, *J. Biomed. Opt.* **2016**, *21*, 50901.

[26] W. Sun, S. Guo, C. Hu, J. Fan, X. Peng, *Chem. Rev.* **2016**, *116*, 7768.

[27] U. Lawrentz, W. Grahn, K. Lukaszuk, C. Klein, R. Wortmann, A. Feldner, D. Scherer, *Chem. - A Eur. J.* **2002**, *8*, 1573.

[28] R. V. Markov, P. A. Chubakov, A. I. Plekhanov, Z. M. Ivanova, N. A. Orlova, T. N. Gerasimova, V. V. Shelkovnikov, J. Knoester, *Nonlinear Opt.* **2000**, *25*, 365.

[29] M. Young, J. Suddard-Bangsund, T. J. Patrick, N. Pajares, C. J. Traverse, M. C. Barr, S. Y. Lunt, R. R. Lunt, *Adv. Opt. Mater.* **2016**, *4*, 1028.

[30] J. Zhang, P. J. Pellechia, J. Hayat, C. G. Hardy, C. Tang, *Macromolecules* **2013**, *46*, 1618.

[31] O. Malinkiewicz, T. Grancha, A. Molina-Ontoria, A. Soriano, H. Brine, H. J. Bolink, *Adv. Energy Mater.* **2013**, *3*, 472.

[32] A. C. Véron, H. Zhang, A. Linden, F. Nüesch, J. Heier, R. Hany, T. Geiger, *Org. Lett.* **2014**, *16*, 1044.

[33] G. Wicht, S. Bücheler, M. Dietrich, T. Jäger, F. Nüesch, T. Offermans, J. N. Tisserant, L. Wang, H. Zhang, R. Hany, *Sol. Energy Mater. Sol. Cells* **2013**, *117*, 585.

[34] J. Roncali, P. Leriche, P. Blanchard, *Adv. Mater.* **2014**, *26*, 3821.
[35] M. Bates, R. R. Lunt, *Sustain. Energy Fuels* **2017**, *1*, 955.
[36] J. Suddard-Bangsund, C. J. Traverse, M. Young, T. J. Patrick, Y. Zhao, R. R. Lunt, *Adv. Energy Mater.* **2016**, *6*, 1501659.
[37] C. J. Traverse, M. Young, J. Suddard-Bangsund, T. Patrick, M. Bates, P. Chen, B. Wingate, S. Y. Lunt, A. Anctil, R. R. Lunt, *Sci. Rep.* **2017**, *7*, 16399.
[38] H. Zhang, B. Niesen, E. Hack, S. Jenatsch, L. Wang, A. C. V Eron, M. Makha, R. E. Schneider, Y. Arroyo, R. Hany, F. Nüesch, *Org. Electron.* **2016**, *30*, 191.
[39] R. Hany, B. Fan, F. A. de Castro, J. Heier, W. Kylberg, F. Nüesch, *Prog. Photovoltaics Res. Appl.* **2011**, *19*, 851.
[40] V. E. Shershov, M. A. Spitsyn, V. E. Kuznetsova, E. N. Timofeev, O. A. Ivashkina, I. S. Abramov, T. V. Nasedkina, A. S. Zasedatelev, A. V. Chudinov, *Dye. Pigment.* **2013**, *97*, 353.
[41] E. K. Lindenberg, G. N. Patey, *J. Chem. Phys.* **2015**, *143*, 24508.
[42] D. Gesevičius, A. Neels, S. Jenatsch, E. Hack, L. Viani, S. Athanasopoulos, F. Nüesch, J. Heier, *Adv. Sci.* **2017**, *1700496*, 1700496.
[43] D. M. Sturmer, In *Chemistry of Heterocyclic Compounds: Special Topics in Heterocyclic Chemistry*; John Wiley & Sons, Inc., 2008; Vol. 30, pp. 441–587.
[44] J. P. Armstrong, C. Hurst, R. G. Jones, P. Licence, K. R. J. Lovelock, C. J. Satterley, I. J. Villar-Garcia, *Phys. Chem. Chem. Phys.* **2007**, *9*, 982.
[45] F. Heym, B. J. M. Etzold, C. Kern, A. Jess, *Phys. Chem. Chem. Phys.* **2010**, *12*, 12089.
[46] J. Wei, B. H. Fan, Y. Pan, N. N. Xing, S. Q. Men, J. Tong, W. Guan, *J. Chem. Thermodyn.* **2016**, *101*, 278.
[47] H. D. B. Jenkins, H. K. Roobottom, J. Passmore, L. Glasser, *Inorg. Chem.* **1999**, *38*, 3609.
[48] J. A. Venables, *Introduction to Surface and Thin Film Processes*; Cambridge University Press: Cambridge, 2000.
[49] S. Jenatsch, R. Hany, A. C. Véron, M. Neukom, S. Züfle, A. Borgschulte, B. Ruhstaller and F. Nüesch, *J. Phys. Chem. C*, 2014, **118**, 17036–17045.
[50] J. Heier, J. Groenewold, S. Huber, F. Nüesch and R. Hany, *Langmuir*, 2008, **24**, 7316–7322.
[51] J. Heier, C. Peng, A. C. Véron, R. Hany, T. Geiger, F. A. Nüesch, M. V. G. Vismara and C. F. O. Graeff, eds. Z. H. Kafafi, P. A. Lane and I. D. W. Samuel, International Society for Optics and Photonics, 2014, vol. 9184, p. 918408.
[52] P. Vivo, A. Ojanperä, J.-H. Smått, S. Sandén, S. G. Hashmi, K. Kaunisto, P. Ihalainen, M. T. Masood, R. Österbacka, P. D. Lund and H. Lemmetyinen, *Org. Electron.*, 2017, **41**, 287–293.
[53] G. M. Sheldrick, *Acta Cryst*, 2008, **64**, 112–122.
[54] C. F. Macrae, I. J. Bruno, J. A. Chisholm, P. R. Edgington, P. Mccabe, E. Pidcock, L. Rodriguez-Monge, R. Taylor, J. Van De Streek and P. A. Wood, *J. Appl. Cryst*, 2008, **41**, 466–470.

Chapter 5 Conclusion

5.1 General Conclusion

In the past decades an increased publication outcome dealing with counterion variation in cyanine dyes and their organic electronic devices has led to a large variety of ionic compounds. All publications have in common that certain molecular anion structures are presented as efficiency enhancers although the mechanisms behind it remains unrevealed. Despite common literature justifications of using cyanine dyes as light absorbers with the aim for green science, their synthesis and particular the ion exchange procedures are carried out using standard approaches employing halogenated solvents and non-stoichiometric excess of material. Although cyanine dyes were implemented as light absorbers decades ago, their processability was restricted to solution based deposition techniques. Furthermore up to now no published content about volatility of cyanine based organic salts exists. Besides that organic solar cell device architectures were limited to bilayer geometry. The challenge is taken to deal with these issues within this thesis. Mechanisms are revealed behind the organic photovoltaic device figures of merit enhancement and a general approach is introduced decoupled from a certain Lewis structure, enabling predictive descriptions regarding fluorescence and organic photovoltaic performance for a particular device stack. The third chapter of the thesis deals with the vaporization of high molecular weight cyanine organic salt, which represents a very seldom phenomenon. Besides this fundamental interest for the first time a cyanine dye containing bulk heterojunction morphology was obtained by vacuum co-deposition.

Inefficient ion exchange procedures and the fundamental question if rather the organic moiety of an anion or its negative charge delocalization are more important for efficient cyanine semiconductors were addressed in the first research chapter. For that purpose a symmetrical pentamethine 2-[5-(1,3-dihydro-1,3,3-trimethyl-2H-indol-2-ylidene)-1,3-pentadien-1-yl]-1,3,3-trimethyl-3H-indolium ($Cy5^+$) chromophore was modified with methanesulfonate, benzenesulfonate, *p*-methylbenzenesulfonate, 2-naphthalenesulfonate anions and the bulky bistriflylimide. The ion exchange takes place using an Amberlyst®A26 (OH^- form) anion exchanger with free acids as anion sources. With the target to introduce a halide-for-anion exchange method that does not necessitate further purification steps and possesses the potential for industrial scale-up. The reasons for efficient ion exchange lays in the fact that quaternary ammonia groups of the ion exchanger preferably bind small and hard anions while the larger and softer ones are released. Therefore salt metathesis occurs driven by the “Hard and Soft Lewis Acids and Bases” (HASAB) principle enabling a quantitative and chemically pure compound after evaporation of volatile compounds. By having the same cationic light absorbing chromophore, the arising differences in semiconductor properties of the various salts can be attributed to the anion variation. Beginning with optical properties in the solid state it was shown that the absorbance peak broadening and aggregation phenomena were significantly reduced in films of the salt containing the weakly coordinating bistriflylimide. Single crystal data revealed a qualitative trend towards higher anion coordination distances when the bistriflylimide was employed. Large chromophore spacing preventing regular packing motives were also favoured by the weakly coordinating anion. Thermal stability of the chromophore was found to be improved by 30 °C when the bistriflylimide anion was employed taking methylsulfonate as a benchmark. Further advantages of the weakly coordinating anion compared to the point like charge sulfonates were obtained in thin film surface formation. Atomic force microscopy analysis has yielded smooth and defect free surface in contrary to rough, pinhole and aggregate containing thin film surfaces of the sulfonate based salts. Drastic enhancement of all relevant organic photovoltaic parameters was observed when the salt containing the bistriflylimide anion was employed as organic semiconductor. Therefore the negative charge delocalisation effect of the anion significantly favours the organic semiconductor properties of a cyanine chromophore over anion size variation by only tuning the organic moiety as represented by sulfonate based anions.

The first research chapter has provided a solid fundament for further development of a more generalized description of cyanine dye semiconductors as shown in the second research chapter. It became obvious that within a salt Coulombic interactions rather than a certain Lewis structure of an anion, play a crucial role in determining semiconducting properties. Furthermore negative charge delocalisation of an anion influencing the Coulomb interactions should be expressed in terms of the lattice energy rather than in a specific anionic Lewis formula. Therefore in order to proof this concept the superweak coordinating tetrakis(nonafluoro-*tert*-butoxy)aluminate ($[Al(pftb)_4]^-$) was introduced to the 2-[5-(1,3-dihydro-1,3,3-trimethyl-2H-indol-2-ylidene)-1,3-pentadien-1-yl]-1,3,3-trimethyl-3H-indolium chromophore as one of the most weakly coordinating anion that can be used in salts for organic photovoltaic applications. The lattice energy of this organic-inorganic hybrid salt as well as lattice energies of the salts used in the first chapter were estimated yielding the inverse of the molecular volume. Taking the solid state absorbance peak width of all salts and plotting against the lattice energy a linear correlation was established. It is shown that the reduction of the lattice energy and Coulomb interactions supress aggregate formation and approaches monomeric like conditions in solid state. Further Photoluminescence measurements revealed individual anions ability to stabilize the chromophore in the excited state. In analogy to the solid state absorbance peak width the fluorescence intensity of neat spin-casted films showed a linear correlation towards higher values with decreasing lattice

energy. An unusual long radiative lifetime of 0.75 ns was obtained for the salt containing the superweak $[Al(pftb)_4]^-$. A strong contrast when considering photoluminescence lifetimes of the other salts below the detection limit of 50 ps. The thermal properties are influenced by the boosted molecular weight of the new salt. The melting point rose by 70 °C compared to the other salts investigated in the first research chapter. Moderate improvement in the thermal stability was achieved taking bistriflylimide as a benchmark. In general the thermal behaviour of cyanine salts indicated a much more complex behaviour than can be described by simple assigning of a melting point and a decomposition point. The surface properties important for a smooth and defect free thin film were strongly affected by the superweak coordinating perfluorinated anion. Dispersive part of the surface free energy matching for both the salt and the vanadium oxide hole transport layer was identified as the major factor for stable and smooth thin film formation. The semiconducting properties of this new organic-inorganic salt were compared with the salts developed in the first research chapter on a universal lattice energy scale. Linear correlations were found among the lattice energy and open circuit voltage (V_{OC}), performance (η) as well as external quantum efficiency (EQE). The open circuit voltage was identified as a device independent property arising in first instance only from the material. The increase of V_{OC} was mainly caused by the reduction of the transfer integrals, which lead to a reduced energetic disorder of highest occupied molecular orbital (HOMO) and lowest unoccupied molecular orbital (LUMO) energy levels. Due to a decreased disorder the gap between HOMO and LUMO increases resulting in boosted V_{OC} values. The efficiency behaved similarly and yielded a solid average value of 3.2% pointing towards highly efficient cyanine semiconductor caused by the superweak coordinating anion. Besides the fluorescence intensity, EQE can be seen as a further expression of the individual anions ability to reduce Coulomb interactions and thus the charge transfer binding energy. This effect lead to the rise in EQE with decreasing lattice energy of the cyanine salts.

The consecutive first two chapters of this thesis have paved the way for a generalized description of cyanine dye salts decoupled form their Lewis formula. This proof of concept paves a future synthetic and descriptive pathway for all charged organic semiconductors and dyes where ever a highly stabilized excited state is needed.

The complex thermal behaviour of cyanine dye salts has been neglected by the literature so far. Thermal experiments carried out in the first two research chapters have indicated a more complex thermal behaviour of cyanine dyes than melting and decomposition. First hints were found that at least a partial evaporation of the salt can take place. The thermal properties were shown to be dependent on the anion in first instance. However the chromophore contribution cannot be neglected either. Therefore a symmetrical trimethine 1-ethyl-2-[3-(1-ethyl-1,3-dihydro-3,3-dimethyl-2H-indol-2-ylidene)-1-propen-1-yl]-3,3-dimethyl-3H-indolium ($Cy3^+$) indocyanine chromophore was modified with the bistriflylimide (TFSI) anion to study changes in Coulomb interactions, thermal stability and the volatility of the organic-inorganic hybrid salt. Properties of the solid state structure from single crystals and thermo-analytical methods were linked to reveal the evaporation mechanism of the dye. Suppressed inter-chromophore interactions preventing regular packing motives as observed for the Cy3TFSI were identified as a crucial parameter for a lower melting point and a wider thermal operational window. From Quasi-isothermal TGA measurements slopes of detected mass loss over time were used to distinguish between a controlled evaporation process followed by a decomposition as observed for the Cy3TFSI or simultaneously occurring overlap of both as it was the case for the starting material. Further derived enthalpy of vaporization at an average temperature quantified the evaporation process of Cy3TFSI salt. By high vacuum physical vapor deposition of neat thin films a significant dependence on the substrate used is shown. An alternative vacuum co-evaporation method yielded a smooth and defect free bulk heterojunction morphology. These experiments have showed that wetting phenomena observed during spincasting from solution also apply to evaporated cyanine films making extended film tuning on different substrates an important issue. Proof of concept was demonstrated by a fully vacuum processed inverted geometry bulk heterojunction OPV device where Cy3TFSI acted as a donor and the fullerene as acceptor. The device exhibited a sufficient amount of photocurrent while both components were contributing to the photovoltaic effect. Therefore this is the first demonstration of a cyanine dye bulk heterojunction solar cell where thin film formation had taken place by a physical vapour deposition based fabrication method. Within this study the known anion influence on electrostatic interactions was widened by thermodynamic aspects covering the increase in vapour pressure, resulting in an increased volatility of the organic salt. The present limitation of thin film formation via spin-casting in cyanine dye based semiconductor research was expanded towards physical vapour deposition. This chapter should initiate development strategies of cyanine based volatile organic salts covering the full visible and infrared spectral absorption range.

5.1.1 Outlook of Future Development

The proof of concepts developed in this work can be generally applied to diverse ionic semiconducting materials. These are not limited to cyanine dye salts and can be transferred among others to ionic organometallic compounds like the “black dye” to name an example as used in dye sensitized solar cells. Most obvious is the transfer of the concepts to near infrared absorbing cyanine dyes. Enabling fabrication of transparent devices for energy generation, upconverters or photodetectors. The estimation of lattice energy could be tailored for complex organic salts and more refined computing methods developed. Experimental values for a broader range of cyanine salts regarding the enthalpy of vaporisation could be collected using thermal gravimetric analysis. The formation of proper

bulk heterojunction morphology was not implemented in cyanine dye semiconductors so far. The developed co-evaporation method allows advanced morphological tailoring opportunities which could lead to state of the art bulk heterojunction device performance once the donor/acceptor ratio, active layer thickness and interlayer adjustments are optimized. New doping opportunities of the bulk heterojunction arise from vacuum co-deposition. Besides new challenging chemical synthesis of more weakly coordinating anions one has to consider alternative structures for cyanine salts. The polymethine backbone terminated by two symmetrical indolenium moieties gives a dumbbell like shaped structure. Such geometry is favourable for rotaxane formation. By having a cyclic anion one could produce cyanine salt rotaxanes. A compound class representing molecular machines entirely unexplored in ionic semiconductor field.

Curriculum Vitae

Personal Information

Date of birth:	05.03.1988
Birthplace:	Kaunas (Lithuania)
Citizenship:	Lithuanian
Family status:	single

Current Position

08/2015 – present	Ph.D. student at EMPA and EPFL, Switzerland

Study

01/2014 – 09/2014	**Master thesis**, carried out at Philipps-University Marburg. **Supervisor**: *Prof. Dr. J. Sundermeyer*. **Titel**: *N- and C-metallated Phosphoranes: Unusual Chelatligand Templates for Transition Metals.*
04/2012 – 09/2014	Master of Science in Chemistry, Philipps-University Marburg.
10/2011 – 03/2012	**Bachelor thesis**, carried out at Philipps-University Marburg. **Supervisor**: *Prof. Dr. J. Sundermeyer*. **Titel**: *Synthesis of new Bisphosphazene and Bisphosphazide Proton Sponges and their Application in Metal Free Hydrogen Activation*.
04/2008 – 03/2012	Bachelor of Science in Chemistry, Philipps-University Marburg.

Vocational Training

2005 – 2007	Chemical-Technical Assistant

Education

2003 – 2005	Adolf-Reichwein vocational school (specialisation in electronics), Marburg
1999 – 2003	Lower secondary school, Wetter

Internships

07/2007 – 01/2008	Internship in quality control department of Temmler Pharma GmbH & Co. Determination of contents and degradation products of drugs via HPLC, GC, IR and UV-Vis. Analysis of the data and qualification of the equipment under GMP conditions.
2006	Four week internship in the department of geoscience at Philipps-University Marburg. Analysis of rock samples from Namibia with ICP/AES.

Publications

- D. Gesevičius, A. Neels, S. Jenatsch, E. Hack, L. Viani, S. Athanasopoulos, F. Nüesch, J. Heier, *Adv. Sci.* **2018**, *5*, 1700496.
- L. Wang, S. Jenatsch, B. Ruhstaller, C. Hinderling, D. Gesevičius, R. Hany, F. Nüesch, *Adv. Funct. Mater.* **2018**, *28*, 1705724.
- R. Langer, A. Gese, D. Gesevičius, M. Jost, B. R. Langer, F. Schneck, A. Venker, W. Xu, *Eur. J. Inorg. Chem.* **2015**, *2015*, 696.
- J. F. Kögel, X. Xie, E. Baal, D. Gesevičius, B. Oelkers, B. Kovačević, J. Sundermeyer, *Chem. - A Eur. J.* **2014**, *20*, 7670.

Research Projects and Learned Methods

- Organometallic chemistry: Synthesis and application of transition and rare-earth metal based homogeneous catalysts. Schlenk/Glovebox techniques, 1D and 2D NMR, MS, CHN, IR, X-ray, GC.
- Biophysical chemistry: Interaction of hybrid gold nanoparticles with HeLa-cells. Sterile work with cell cultures, AFM.
- Material chemistry: Synthesis of carbon nanotubes on laser modified stainless steel surface. Surface structuring with pulse laser, CVD, SEM/TEM, chromatic white light sensor, Tensiometer.
- Macromolecular chemistry: Synthesis of smart, biodegradable, antibacterial, copolymers and microcapsules. Polymerisation techniques, GPC, DSC, TGA, DLS.
- Current research: OPV device construction, spincoating, thermal evaporation techniques, reflectometry, interferometry, elipsometry, CV, UV-Vis, IV measurements for OPV efficiency, IPCE, CELIV, kelvin probe, SAXS/WAXS, AFM, SEM.

Conferences

- D. Gesevicius, A. Neels, J. Heier, F. Nüesch, Presentation: “Physical Vapour Deposition of Cyanine Dye and First Application in Organic Electronics”, *Gordon Research Conference on Solar Energy Conversion*, *Hong Kong, 2018.*
- D. Gesevicius, A. Neels, J. Heier, F. Nüesch, Presentation: “General Approach for an Efficient Anion Exchange in Organic Salt Semiconductors”, *101st Canadian Chemistry Conference, Edmonton (Canada), 2018.*
- D. Gesevicius, A. Neels, J. Heier, F. Nüesch, Poster: “Engineering of a Cyanine Chromophore and Application in an Organic Solar Cell”, *Zing Conference on Organic Semiconductors, Dubrovnik (Croatia), 2016.*

Zürich, 14th of September 2018